MANIPULATING THZ RADIATION USING NOVEL METAMATERIALS TOWARDS FUNCTIONAL PASSIVE AND ACTIVE DEVICES

By

YONGYAO CHEN

Bachelor of Science in Optoelectronics
Tianjin University
Tianjin, China
2003

Master of Science in Physical electronics
Tianjin University
Tianjin, China
2006

Submitted to the Faculty of the
Graduate College of the
Oklahoma State University
in partial fulfillment of
the requirements for
the Degree of
DOCTOR OF PHILOSOPHY
July, 2012

MANIPULATING THZ RADIATION USING NOVEL METAMATERIALS TOWARDS FUNCTIONAL PASSIVE AND ACTIVE DEVICES

Dissertation Approved:

Dr. Weili Zhang

Dissertation Adviser

Dr. Daniel Grischkowsky

Dr. Daqing Piao

Dr. Yingmei Liu

Outside Committee Member

Dr. Sheryl A. Tucker

Dean of the Graduate College

TABLE OF CONTENTS

LIST OF FIGURES

Figure Page

Figure Page

CHAPTER I

INTRODUCTION

There has been increasing interest in the fields of plamonics and metamaterials, which become fascinating research fields of microstructure photonics. It explores how light-matter interactions can be controlled by using dielectric or metallic subwavelength composites. The beauty of this field is that the artificial media can gain their extraordinary optical properties from discontinuity or subwavelength structures rather than directly from their intrinsic compositions. Terahertz (THz) technology is another emerging frontier providing challenges for fundamental research and opportunities for new applications [1-4]. In this field, researchers explore light-matter interaction occurring at wavelength ranging from 30 μm to 1mm. People have realized that THz technology has very promising applications in medicine, microscopic imaging, superfast circuit, computers and communications; however, bottlenecks of electromagnetic materials in the THz region impede the development of these technologies. For example, there is a lack of materials with simultaneously strong resonance and low intrinsic loss in the THz region. Also no natural materials exist with very high refractive index and low intrinsic loss, which are suitable for waveguides. Another challenge is the relatively poor ability to manipulate the amplitude and phase of THz radiation within a broadband spectrum.

Fortunately, the introduction of microstructure photonics, metamaterials and plasmonics in THz technology, may overcome the challenges and lead to breakthrough applications. On the other hand, functional THz devices such as filters, delay lines, switch/modulators, phase shifters, waveguides and sensors, are key elementary devices to freely manipulate THz radiations. It will be demonstrated that the metamatreial based devices could significantly boost the performance for both passive and active functional devices. It is expected that the combination of metallic microstructure photonics and THz technology can resolve the above challenges. By using periodic small structures, one can create effective media to control the flowing of THz light at will. Thus, merging plasmonic and metamaterial for the control of THz radiation will open up an entirely new world of THz technology and may lead to breakthrough applications in a broad range of disciplines.

Artificial media based on plasmonics and metamaterials open up new perspectives on the manipulation of light. These research fields have already made impacts in fundamental optics and could lead to important applications in optoelectronic devices. Notable examples including spoof surface plasmons on micro-structured surfaces (section 1.1), negative refractive index materials (section 1.2), and artificial slow light media (section 1.3), will be highlighted in the following sections in this chapter. Some manifestations in these examples are important in relation to the novel optical properties of plasmonic media and metamaterials and could be used in technological applications in the THz region.

1.1 Designing the THz surface plasmons with micro-structured surfaces

The long wavelength diffraction of THz wave (with wavelengths lie between 30 μm and 1 mm) limited the abilities to control the propagation of THz waves with high-optical-confinement which is potentially important for miniaturization of THz waveguide and improving resolution in the THz imaging systems. To achieve the capability, researchers may follow the successful experiences in the optical region, where the efficient confinement and focusing of light can be achieved through dielectric waveguides with high refractive index, or through surface plasmon polaritons (SPPs) on the surfaces of metals [5-15]. Unfortunately, in the THz region, there is a lack of materials that have very high refractive index and low intrinsic loss. Moreover, SPPs on the metal surfaces, which are powerful and renowned for the strong field localization in the optical region, become incapable in the THz band, because the high-optical-confinement of SPPs can only be achieved near the surface plasmon frequency of metals, which is usually in the visible or UV spectrum region. Since THz radiation is with frequencies far away from the surface plasmon frequency of the metal, THz SPPs are essentially the Sommerfeld-Zenneck waves with very weakly confinement [16-19], and the fields of THz SPPs extend many wavelength in space (illustrated in Figure 1-1).

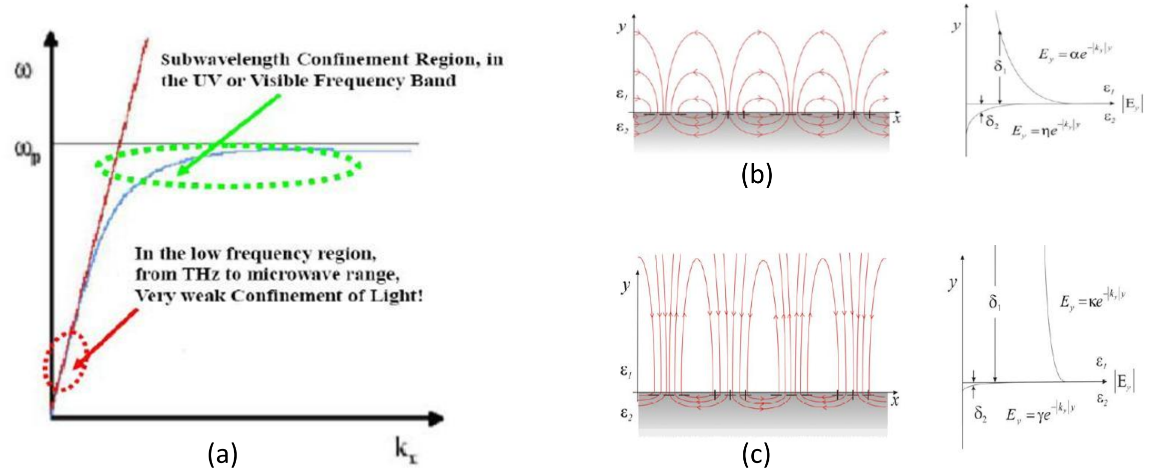

(a)

(b)

(c)

Figure 1-1 (a) Schematically dispersion curve of SPPs on metal surface. (b) Field confinement in the optical region. (c) Field confinement in the THz region [8].

In order to overcome the above challenges, it is proposed that by fabricating microstructures on metal surfaces, the high-optical-confinement of SPPs in the optical band can be transferred to the low frequency region such as the THz or microwave band and these surface modes are known as "spoof surface plasmon polaritons" [20-25]. For example, as illustrated by Figure 1-2, by drilling hole on a metal surface, one can create effective responses of surface plasmons which can be designed through the geometric parameters. In this way, the high confinement of SPPs can be achieved near the effective surface plasmon frequencies.

This high-confinement region can be designed by the structured surface and can be extended from the microwave region to the THz region. The function of the holes or grooves on the metal surfaces is that they increase the penetration depth of electromagnetic field into the holey metals, as shown in Figure 1-2 (a), thus enhancing the confinement ability for light.

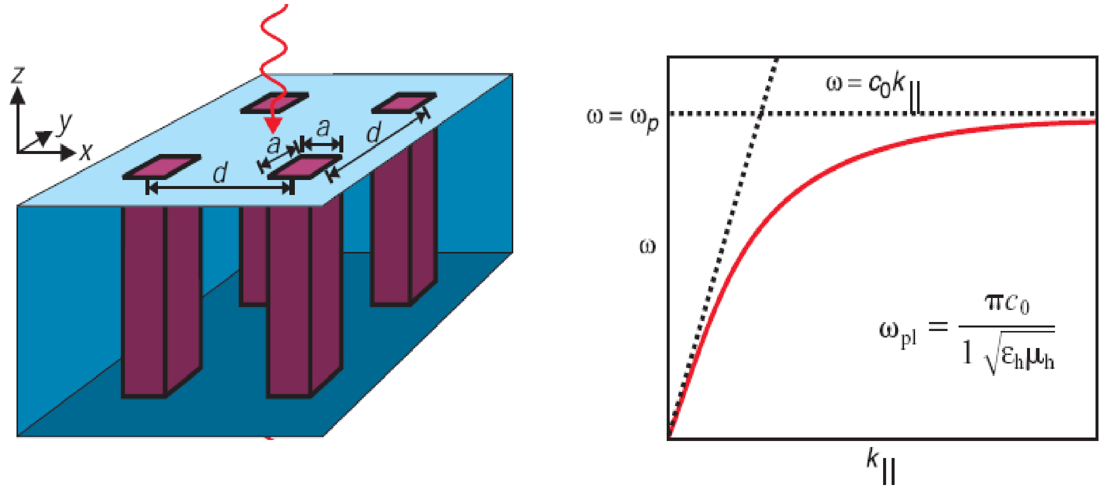

(a) **(b)**

Figure 1-2 (a) Square holes cut into the surface of a perfect conductor. (b) Dispersion relation for the effective surface plasmons on the structured surface [20,21].

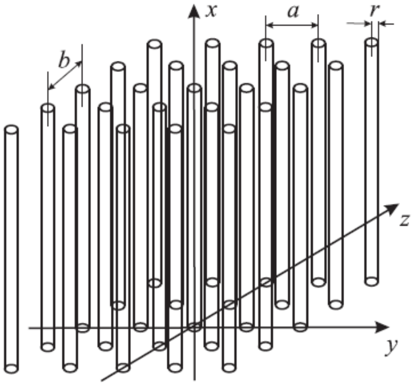

Figure 1-3 The geometry of wire medium comprised of a spare lattice of parallel conduction wire [27].

It should be noted that the dispersion of the effective surface plasmon on the flat metal surface has close resemblance with the dispersion of the SPPs supported by the real metal surfaces. In the low frequency range, both of the dispersion curves approach the air line, while at a large propagating constant for the SPPs dispersion curve on the real metal surface, the eigenfrequencies approach the surface plasmon frequency determined by the intrinsic metal property; whereas in the structured metal surface, effective surface plasmons approach the frequency region which is the cut-off frequency of cavity waveguide.

1.2 THz metamaterials

THz radiation is an intriguing electromagnetic wave with great potential applications in sensing, imaging, and spectroscopy. However, the development of efficient techniques to control the THz radiation is limited by the lack of materials that have naturally strong resonance, which is the key to achieve high efficiency functional devices. Fortunately, Metamaterials can offer a promising way for the future technology in the THz regime, as the electromagnetic response of metamaterials can be engineered in the microstructures rather than the intrinsic compositions [26-35]. Moreover, it has been demonstrated that metamaterials can be designed to achieve novel response in the THz region, having large values of positive or negative permittivity and permeability with broadband tunability [36-46].

1.2.1 Metamaterials with negative permittivity $\varepsilon_{\mathrm{eff}}<0$.

The most fascinating property of metamaterials is that both the electrical and magnetic responses can be determined by the metallic structures. The effective electrical and magnetic response can be attributed to two parameters, i.e. electrical permittivity $\varepsilon_{\mathrm{eff}}$ and magnetic permeability μ_{eff}. When both of the electrical permittivity and magnetic permeability become simultaneously negative, negative index of refraction can be achieved, producing important applications, such as superlense, in which the imagine resolution can be greatly enhanced [27,28], and cloaking technique, which can make objects invisible in difference wave band [34,35].

In order to achieve negative index materials, we first need to design the electromagnetic response with negative electrical permittivity, that is $\varepsilon_{\mathrm{eff}}<0$.

It is proposed that the periodic thin wire media can be used to achieve negative effective permittivity. As shown in Figure 1-3, a periodic lattice of metal wire form an effective medium, in which the radius of the metal wire is much smaller than the period of wire lattice. The effective permittivity can be described by the following equation which counts the geometry property [27],

$$\varepsilon_{eff} = 1 - \frac{\omega_p{}^2}{\omega(\omega + i\,\varepsilon_0 a^2 \omega_p{}^2 / \pi r^2 \sigma)} \;, \tag{1-1}$$

where ω_p is the intrinsic plasma frequency of metal wires. The electrical response of this wire medium resembles a plasma-like permittivity where the value of the effective permittivity is frequency dependent and becomes negative or positive when below or above the effective bulk-plasma-frequency.

1.2.2 Metamaterials with negative permeability $\mu_{\mathrm{eff}}<0$

Because the existence of magnetic charges is prohibited, natural materials cannot have negative magnetic permeability. However, artificial metallic structures which have strong inductive responses near the resonance frequencies can exhibit negative effective magnetic permeability [28]. The most popular artificial magnetic metamaterials are split-ring resonators (SRRs), as shown in Figure 1-4. It should be noted that the SRRs structures are widely used in the THz metamaterials since they are easy to be fabricated by the conventional photolithography technique. The effective permeability can be described by the following equation which also counts the geometry property:

$$\mu_{eff} = 1 + \frac{f\omega^2}{2c^2 d / \varepsilon\pi^2 r^3 - \omega^2 - i\,2\rho\omega / r\mu_0} \quad , \tag{1-2}$$

where $f = \pi r^2 / a$. This kind of magnetic metamaterials can be designed to achieve negative permeability around the resonant region within a narrow frequency spectrum.

The combination between wire medium and SRRs (see in Figure 1-5) can create a double-negative material with negative refractive index in which both permeability and permittivity are negative.

It is expected that THz metamaterials would play an important role in the progress of THz technology, and may have important applications for designing new THz optoelectronic devices, such as switches, modulators, filters and high-resolution imagine systems.

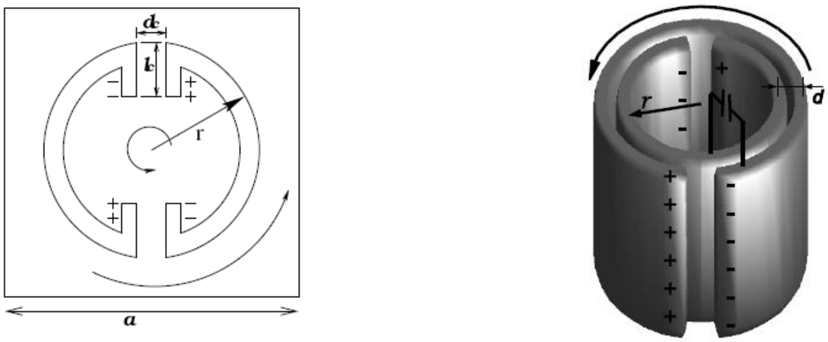

Figure 1-4 Left: the unit cell of array of split-ring resonators (SRRs). The right is the single component of the artificial magnetic metamaterials [28,35].

Figure 1-5 Double-negative material comprised of metal wires and SRRs to realize the negative refractive index metamaterials [31,35].

1.3 Plasmonics and metamaterials for THz slow light technique

Slow light technology is to control and slow down the propagation speed of light signals. As an emerging new field, slow light is not only conceptually fascinating but also has important applications, such as optical communications, signal data manipulation, and quantum information processing [47]. On the other hand, the unprecedented growth and development of wireless communication are requiring higher data rates and broader bandwidth, and the current high speed wireless communication systems that work in the microwave band may not satisfy the future requirement. It can be expected that in future the wireless communication systems will go towards THz region that can support higher communication speed and ultra-wide spectral bandwidth [48-50]. Slow light technology in THz communications will become an important topic due to its potential for manipulating the THz signal delay, and the THz slow light devices are the key element to achieve the tunable signal delay and have important applications including signal synchronization, multiplexing and buffering in the THz communication systems. However, currently in the THz regime, there is a lack of technology that can extremely slow down the THz light, as well as a lack of materials that are suitable to achieve high efficiency slow light devices. Metallic subwavelength structures have recently attracted numerous attentions for their great potential in developing slow light devices. It is thus of great interest and merit to bridge between the fields of metamaterials and slow light, which may pave a way for developing new research directions and important applications. Recent progress on slow light in artificial plasmonic structures [51,52], electromagnetically induced transparency in metamaterials [53-57], and "trapped rainbow" in tapered negative and positive index waveguide [58,59], have demonstrated new scopes and possibilities in both metamaterial and slow light. Various schemes in actively control of light trapping and releasing have been reported in metamaterial structures. Tsakmakidis et al. proposed a three-layer waveguide heterostructure, in which the waveguide core with isotropic negative-index materials was sandwiched by regular dielectric claddings. The scheme for light trapping relies on the negative Goos-Hänchen lateral displacements at the media interfaces, and the trapped light can be released by locally tuning the structure to perturb light path based on the effective Goos-Hänchen lateral displacements [58]. Recently, Gan et al. proposed a graded metallic grating structure that supported spoof surface plasmon polaritons, and the light trapping and releasing were implemented through a thermal-optical effect [52]. At terahertz frequencies, the realization of metamaterial waveguides with isotropic negative index of refraction remains challenging. Due to different material properties, fabrication issues, and increased metal loss, isotropic negative index metamaterials continue to elude the terahertz regime. In addition, to pursue modulation scheme with higher speed compared with the thermal tuning, particularly to be able to use micro-electro mechanical systems (MEMS) based elastic tuning, a novel metamaterial approach that enables high speed dynamic mechanical tuning at MHz switching speed [59-61] is expected.

1.4 Dissertation outline

The objective of this work is to explore the fundamental physics in novel metamaterials functioning in THz region, and to develop passive and active functional devices, such as filters, switch/modulators, waveguides and sensors.

The outline of this report is as follows.

Chapter I generalizes the introduction of plamononic structures, metamaterials and slow light technology combined with THz metamaterials.

Chapter II presents the experimental and numerical demonstrations of membrane metamaterials, which are highly promising candidates towards cost-effective and high-performance devices, such as high- Q THz filters and disposable THz sensors. Moreover, the possibility to implement THz slow-light control through the planar metamaterial devices is demonstrated. A systematically experiment method based on THz time-domain-spectroscopy (THz-TDS) is designed to study the slow-light phenomenon and to evaluate the performance of slow light devices in the THz region. Furthermore, the active control of THz slow light is proposed by using the hybrid planar metamaterials consisting of metals and semiconductors.

Chapter III conducts a comprehensive theoretical study of anisotropic metamaterial waveguides, which exhibit strong wave dispersion and trapping behavior. Further proposed microscopic model reveals the underlying mechanism of light trapping, and helps further engineering of active metamaterials for the transitions between light trapping and releasing. This extreme manipulation of light implemented by metamaterial waveguides is not only conceptually fascinating, but also opens the door for a broad range applications, including optical delay-lines, all optical routers, ultra-broadband absorbers, sensitive detectors and optical sensors benefited from the enhanced light-matter interaction in metamaterial waveguides. Parallel-plate waveguide combined with photonic crystals are also proposed to realize the waveguide switches and modulator, and are expected to be useful in tunable quantum cascade lasers.

Chapter IV demonstrates that surface wave resonance supported by the membrane metamaterials can be incorporated into the design of broadband tunable devices, and show great potential in practical applications such as broadband filters functioning in the far-infrared region. We experimentally studies the role of electric and magnetic dipoles for the excitation of surface waves supported by planar membrane metamaterials. It is confirmed that magnetic dipoles are weakly coupled with surface modes, while electric dipoles can significantly enhance the excitation of surface waves. As potential applications, membrane metamaterials could offer well-performed amplitude and phased modulation schemes implemented by active control the surface mode resonances within a broadband. Furthermore, the coupling and strong interaction between localized mode and surface mode are investigated. The physics and promising functional devices make the surface mediated metamaterials interesting and fascinating for future tunable plasmonic or metamaterial devices.

Chapter V demonstrates that textiles could be applied as functional electromagnetic materials with very novel electromagnetic properties. Moreover, bridging the electromagnetic textile materials with microfluidic systems functioning in the THz region, may pave a way in developing both functional metamaterials and new THz optofluidic systems, such as fluidic controlled metamaterials. Importantly, a new microfluidic sensing platform is demonstrated, which is benefited from the strong light-fluid interaction in textile metamaterials, showing great potential for cost-effective and high performance sensing platform useful in chemistry, biology and medicine applications.

CHAPTER II

PLANAR METAMATERIALS FOR THZ RADIATION

Planar metamaterials are based on frequency-selective surface (FSS) technology [62]. They have attracted a great deal of attention for the promising potential in developing THz functional devices, such as filters [63-67], switch/modulator [37,38,68], waveguides [69-72], THz sensors [73] and slow-light chips [53-57]. However, the development of practical functional devices is impeded by several limitations, including the expensive fabrication , the undesired Fabry-Perot signal in conventional substrates, low quality (Q-factor) resonators and detection limits of sensors. In this Chapter, I proposed that membrane metamaterials are highly promising candidates towards cost-effective and high-performance devices, such as high- Q THz filters, and disposable THz sensors. In our study, a number of factors, including the resonator geometry, dielectric losses of substrates and the membrane thicknesses are found to extensively influence the resonance properties of membrane metamaterials. Moreover, I explore the possibility to implement THz slow light control through the planar metamaterial devices. A systematically experiment method based on THz-TDS is designed to study the slow-light phenomenon and evaluate the performance of slow light devices in the THz region. Furthermore, the active control of THz slow light is proposed by using the hybrid planar metamaterials consisting of metals and semiconductors, and the active control is implemented by the photo-excitation of carriers into semiconductor components.

2.1 Fabrication of membrane metamaterials

Recent reported fabrication methods of membrane resonators use traditional photolithography technique and apply additional processes such as thin film deposition [74], curing [75] or etching [76] for the formation of thin film substrates. Although these processes can well fabricate THz resonators on the membranes, they add complications for the fabrication and only produce a very limited sample size, thus severely increasing the costs towards real life device applications. As an improvement, we directly fabricate metamaterial resonators on inexpensive polymer membranes using simple photolithography technique. The simple fabrication processes allow large-area production of thin-film metamaterials, this paves a way for low cost and well-performed THz functional devices such as filters, and most importantly, enable a large volume of production of THz sensors which are highly desired for single-use components such as disposable THz sensors in chemistry, medicine and biology.

The processes of fabrication method are shown in Figure 2-1. The substrates are commercially available polypropylene or polyethylene thin films with thicknesses ranging from 10 μm to 50 μm. The main procedures are as following: (1) positive photoresist PR1-4000A (Futurrex) of 4000 nm thickness is span coated onto the thin film; (2) the sample is soft-baked in a convention oven at 100^{o}c for 15 minutes; (3) the sample is then tightly contacted with the photomasks and exposed to UV light (436 nm wavelength); (4) the exposed sample is developed using resist developer RD6 followed by thermal metallization of 200 nm thick Aluminum (Al) film; (5) the liftoff of metal is performed in acetone, and the sample is then cleaned and dried up with compressed air. The minimum feature size can reach 4 μm, which is good enough for device tolerance.

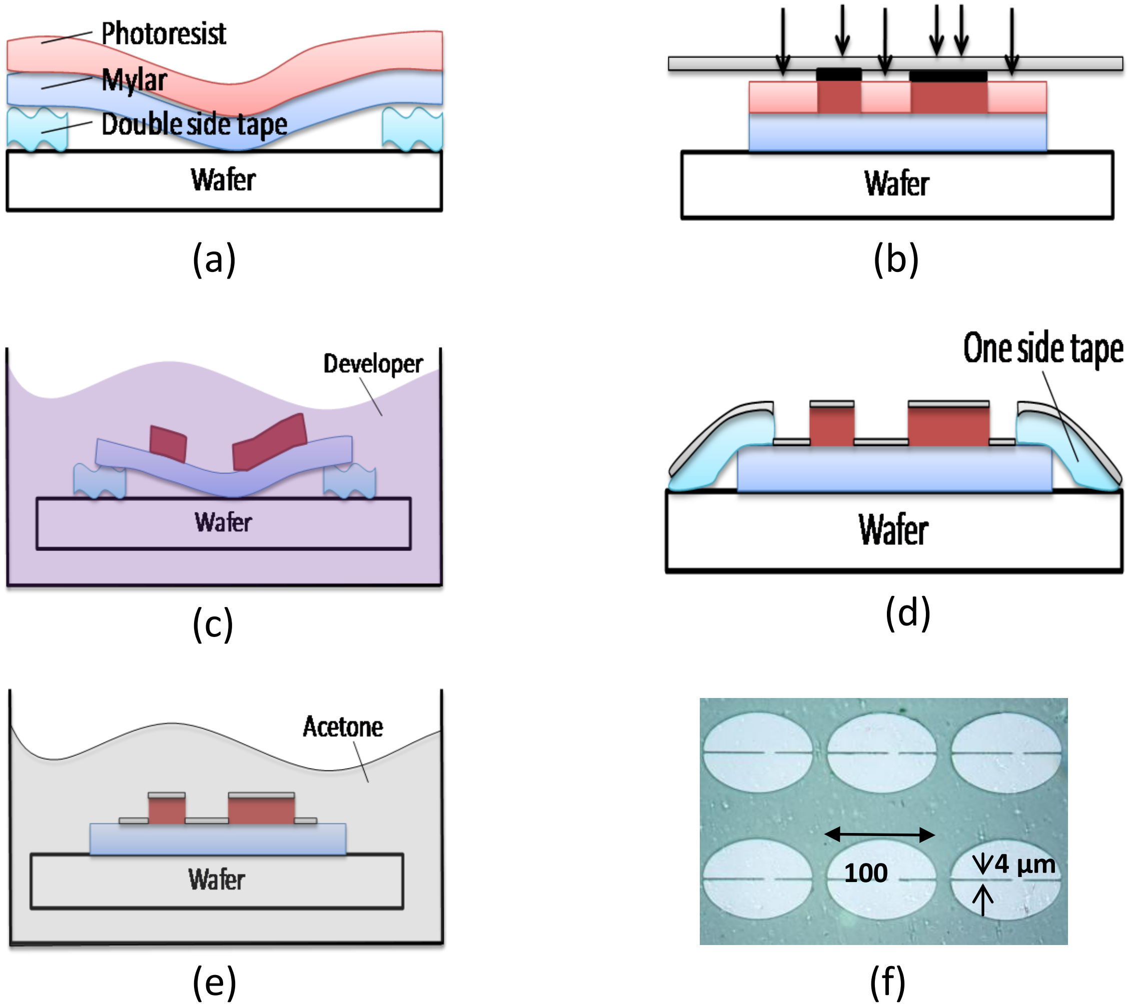

Figures 2-1 Fabrication processes for metamaterial resonators on the thin film substrates. (a) Photoresist coating. (b) Exposure. (c) Development. (d) Metalization. (e) Lift-off. (f) Microscopic image of the sample. In this process, the minimum feature size can reach 4 µm, which is good enough for device tolerance.

However it should be pointed out that the conventional photolithography technique used in our fabrication is difficult to apply for the ultrathin polymer substrates (less than 10 μm), this is due to the issue of thermal expansion mismatch between polymer membranes and coated photoresists, which may seriously influence the quality of the sample fabrication. We plan to use a simple and low-cost photoresist-free shadow mask technique to fabricate future optimized ultrathin devices [77], where no thermal processing is involved. Besides the optimization of fabrication technique, further optimized design of membrane metamaterials devices should consider various factors such as the geometry of the resonator, the dissipation losses of metals and substrates, and the thickness of the membranes substrates, all these elements should work synergistically to achieve well performed devices.

2.2 Membrane metamaterial resonators with high Q resonance

Metamaterial resonators such as split ring resonators (SRRs) are essential elements for building the functional devices, such as THz filters and sensors. However, suffering from radiation loss, the resonances of SRRs are usually broad, seriously influencing the performance of these functional devices. Thus, the developing of THz filters and sensors would get a strong boost from metamaterial resoantors of a high quality factor *Q*. Recent works are focusing on the geometry design of metamaterial unit resonators, which has been conformed as crucial a factor to enhance the performance of metamaterial devices. For example, asymmetric unit structures are introduced in resonators to enable sharp resonances with high quality factors (*Q*-factor) by suppressing radiation losses [63-67,78].

Most of these high-*Q* metamaterial resonators are fabricated on conventional thick substrates, such as silicon and quartz wafers. However, the Fabry-Perot (F-P) oscillations in the substrates can influence the high-*Q* response of the metamaterial devices. To eliminate such F-P effects

[66,79], the unit resonators normally require bonding to a thick wafer via an optical contact in order to extend the separation between the main time-domain pulse and the reflected pulses. This, however, leads to additional complications in the measurements and results in bulky and high-cost devices. In addition, such metamaterial sensors based on conventional substrates may be insensitive to the external analytes due to the dominant contribution of the thick substrates [73].

So far, less attention has been paid to membrane-based high-*Q* metamaterials, which would resolve the problems encountered in conventional substrates, and are particularly advantageous for developing high-*Q* filters and sensors operating at terahertz frequencies. The membranes with subwavelength thickness can easily shift the Fabry-Perot oscillation outside the resonance frequency region [80]. In sensing applications, thin and low dielectric constant membranes typically enhance the contribution of the sensing target, in turn improving sensitivity [81,82]. In this chapter, we study the resonant properties of high-*Q* membrane metamaterial resonators by way of THz-TDS. The geometry of the unit resonators, dielectric loss, and thickness of the membranes are found to dominate the high-*Q* responses of metamaterials. We experimentally compare the resonators patterned on membranes (thin substrates) with identical structures fabricated on thick substrates using THz-TDS characterization and confirm the advantages of membrane based high-*Q* resonators as high-performance filters and sensors. Moreover, an analysis of the membrane thickness-dependent-sensitivity for sensing applications reveals that the high-*Q* membrane metamaterial sensors with moderate thicknesses (dozens of microns) are a good compromise to ultrathin devices (hundreds of nanometers). In turn, this may open a route for straightforward, low-cost, and large-scale productions of the high-*Q* membrane sensors.

2.2.1 Experiment and numerical simulation setup

As a proof-of-principle demonstration, a double-gap elliptical resonator (ER) is proposed as a unit cell to explore the fundamental inductive-capacitive (*LC*) resonance which plays an essential role to realize the desired electromagnetic responses. Figure 2-2 shows the layout of the unit cell, in which an elliptical metal patch is separated by an air gap but electrically connected with a rectangular bar. The double-gap ER is a variant design of the electrically resonant double-split-ring resonators [83]; it accomplishes a goal of effectively breaking the electric balance of the resonator by introducing weak mirror asymmetry, and it allows for analyzing both the *LC* and dipole resonances in a close frequency region, where the influence of the F-P oscillations in the thin substrates can be neglected [80]. The level of mirror asymmetry of the resonator can be engineered by gradually displacing the metal bar from the center of ER.

A square array of double-gap ERs made from 200 nm of Aluminum (Al) is fabricated on commercially available thin Mylar films of 22 μm thicknesses (the membrane). Such substrate thickness is amenable in view of its simple fabrication and offers device robustness over the design of ultrathin membrane resonators. Samples of dimensions 10×10 mm^2 are experimentally characterized in an 8F confocal THz-TDS system [84]. To accurately reveal the sharp resonances, we extend the time domain measurement of the terahertz pulses to 100 ps, corresponding to a spectral resolution of 10 GHz. Besides the experimental measurements, numerical simulations based on a finite integration technique are also carried out using CST Microwave Studio to elucidate the observed transmission properties. In the simulation, periodic boundary conditions are applied to the unit cell where a normally incident plane wave excitation is used to obtain the transmission parameters. The thin Mylar substrate and Al film are modeled with a permittivity of $\varepsilon_M = 2.86 + 0.2i$ [85] and conductivity $\sigma_{AL} = 3.7\times10^7\, S\cdot m^{-1}$ [86], respectively.

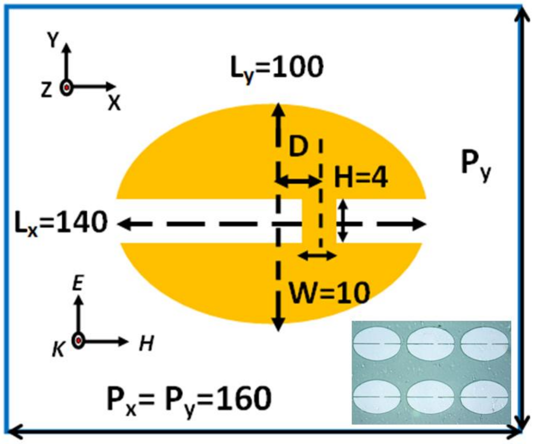

Figures 2-2 Schematic of a unit cell of the elliptical DSRRs, where an elliptical metal patch is separated by an air gap but electrically connected with a rectangular bar. The longer and shorter axes of the elliptical structure are L_x = 140 µm and L_y = 100 µm respectively. The width of the gap is 4 µm, and the dimensions of the bar are W = 10 µm and H = 4 µm. The displacement of the bar from the center is D. The periodicity of the unit cell is P_x = P_y =160 µm. The directions of the electric and magnetic fields indicate the polarization of the incident terahertz wave. Inset: microscopic image of the resonators fabricated on the Mylar substrate with a thickness 22 µm.

2.2.2 Effect of the resonator geometry

Figure 2-3(a) shows the transmission spectra, measured for ER resonators with different levels of geometrical asymmetry. The incident electric field of the terahertz radiation excites two types of resonances, one being the dipole resonance in the high frequency region and the other being the fundamental *LC* resonant at a lower frequency. The numerical results shown in Figure 2-3(b) agree well with the measured data. Furthermore, simulations of surface current distributions on the unit ER resonator are also carried out, in order to get an insight into the physics associated with the observed resonant behaviors. For the symmetric resonators, corresponding to a displacement $D = 0$ μm of the rectangular bar (dashed curve), the transmission reveals two resonant modes located at 0.66 and 1.5 THz respectively, corresponding to the *LC* and the dipole resonances. The *LC* resonance has a measured bandwidth of 112 GHz and a corresponding *Q*-factor of approximately 6. As illustrated in Figure 2-4(a), the surface current distributions of the *LC* resonance show a symmetric pattern, where two surface current loops on the left and right sides are identical and associated with the excitation of a fundamental *LC* resonance suffering from a large radiation loss. When introducing a weak mirror asymmetry $D = 5$ μm (solid curve), a sharp Fano-like resonance was shown around 0.77 THz with a bandwidth of 40 GHz and a *Q*-factor of 19, due to the suppression of radiation loss [78]. The origin of the Fano-like resonance arises from the constructive and destructive interferences of a narrow discrete resonance with a broad spectral line or continuum, resulting in an asymmetric line-shape [87]. It is expected that Fano-like resonance experiences gradual decrease in terms of *Q*-factor when the asymmetry is increased [65,88]. When the displacement of the rectangular bar changes from $D = 5$ to 10 μm, the asymmetric resonance is blue-shifted to 0.83 THz and the original asymmetric current-loops shown in Figure 2-4(b) transform into a single-current-loop on one side of the resonator illustrated in Figure 2-4(c). Consequently, the sharp resonance degenerates to a single SRR *LC* resonance with a relatively broad bandwidth and a low *Q*-factor of 10. The above study indicates that the sharp resonance of the membrane metamaterials can be strongly controlled through a geometrical variation of the resonator parameters. Since the equilibrium of the surface charge distribution on the resonator is broken by the introduction of asymmetric structures, the pattern of current loops associated with the radiation loss can be modulated by the redistribution of surface charges.

Figure 2-5 shows the detailed calculations of displacement-dependent response of the high Q Fano-like resonances. To explore the independent effect of the geometrical asymmetry, we implement the numerical calculation by assuming that the Mylar film is lossless. It is clear from Figure 2-5(a) that resonators with low levels of asymmetry could have high Q responses. However, as shown in Figure 2-5(b), where the resonance strength is represented by the amplitude transmission at the resonance dips, and the lower amplitude transmissions indicate deeper resonance dips associated with stronger resonance strengths. It is obvious that the high Q Fano-like responses of weak asymmetry resonators suffer from weak resonance strength, which may be useless for the filter development and limited in the sensing application due to the poor signal-to-noise level. Choosing a moderate low level of asymmetry such as D= 5 μm for the resonators is a good compromise to obtain a strong Fano-like resonance with a relatively high Q factor, which is useful for practical applications. In the following sections, D=5 μm is chose as an appropriate parameter for the further analysis on the effects of membrane substrates.

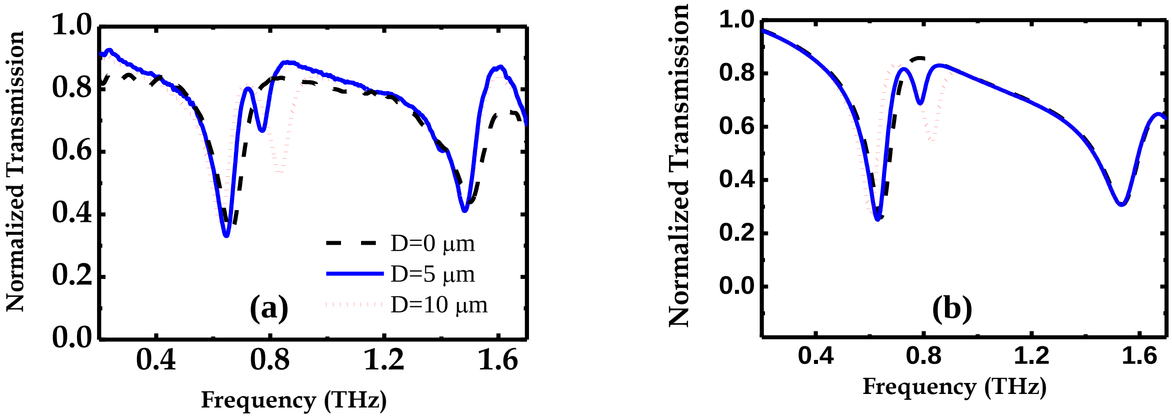

Figure 2-3 Measured (a) and Simulated (b) amplitude transmission spectra through the metamaterial samples with different levels of asymmetry.

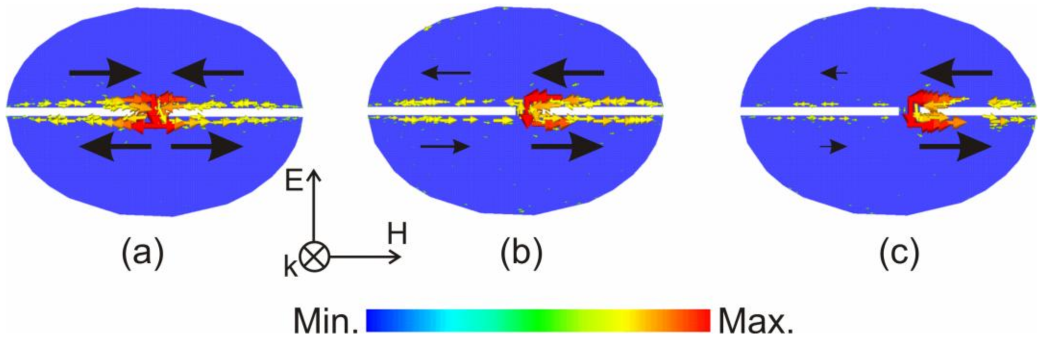

Figure 2-4 Surface current distributions (arrows) associated to the sharp resonances with different levels of asymmetry: (a) $D = 0$ μm at 0.66 THz, (b) $D = 5$ μm at 0.77 THz, (c) $D = 10$ μm at 0.83 THz. The directions of the electric and magnetic fields indicate the polarization of the excitation source.

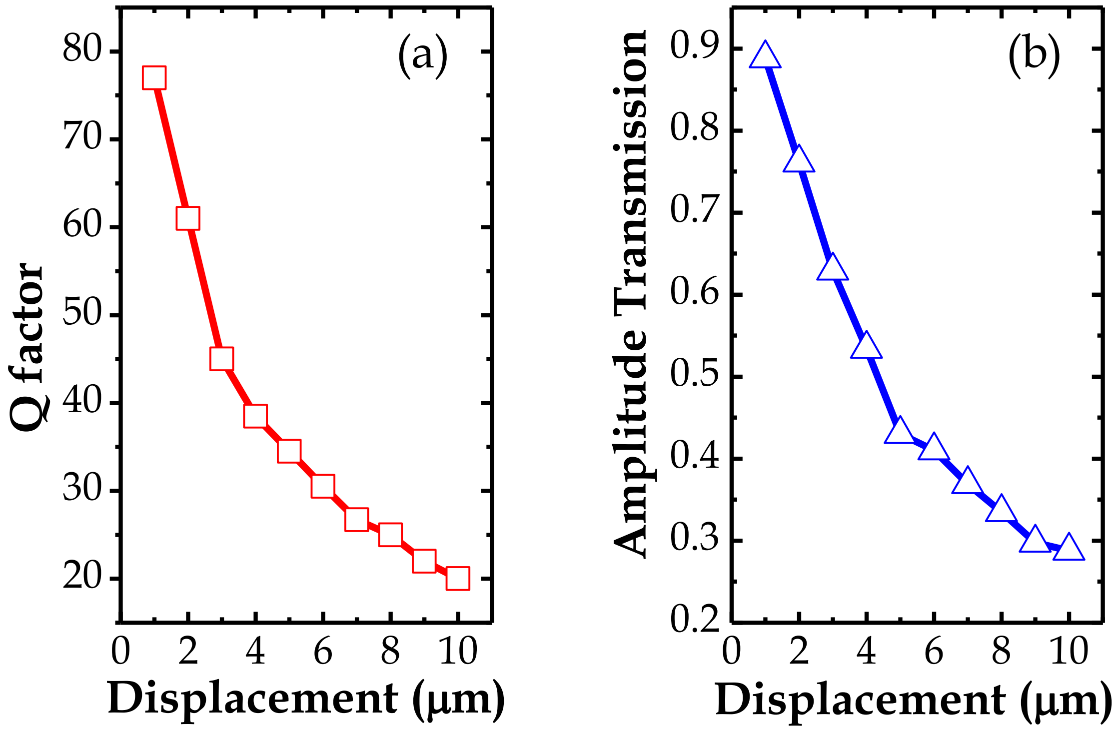

Figure 2-5 (a) Q factors with respect to the levels of asymmetry of resonators. (b) Resonant strength (represented by the amplitude transmission) with respect to the levels of asymmetry of resonators. The Mylar film is assumed to be lossless.

2.2.3 Effect of the membrane substrates

Having discussed the effect of the geometry on the resonators, we will now focus our attention to the properties of the membrane substrate, including its dielectric loss and thickness, which may significantly influence the resonant strength and the *Q*-factor of the sharp resonance. To explore the effects of the membrane properties on the sharp resonance, the geometry of the resonator is fixed, with D = 5 μm in our case. The dielectric loss-dependent resonances are simulated, as shown in Figure 2-6(a), by assuming that the membrane substrate is a thin Mylar film with a thickness of 22 μm and with a real part of the dielectric constant $\mathrm{Re}(\varepsilon_M) = 2.86$. The imaginary part of dielectric constant $\mathrm{Im}(\varepsilon_M)$ is associated with the dielectric loss through the loss-tangent $\delta = \mathrm{Im}(\varepsilon_M)/\mathrm{Re}(\varepsilon_M)$. The influence of dielectric losses is shown in detail in Figure 2-6(b), where the resonance strength is defined by the amplitude transmission at the resonance dips. It is evident that membranes with small loss-tangent have minor electromagnetic energy dissipation in the substrate region, thus supporting strong and sharp resonances. For example, polymer membranes, such as polypropylene or polyethylene films, allow for a controllable thicknesses and a relative low dielectric loss (δ =0.02) in the terahertz regime [85,89]. Thin films formed by silicon compounds, such as silicon nitride, enable very low-loss (δ =0.005) and ultrathin membrane substrates with nanometer thicknesses. Obviously, these membrane materials are appropriate for the implementation of high-*Q* resonators at terahertz frequencies. However, the sharp response can be seriously degraded or even totally suppressed in terms of both resonance strength and *Q*-factors for high-loss membranes, such as Polyaramid films with δ = 0.12 in the terahertz regime.

The thickness of the membrane is another essential factor that significantly affects the resonant properties of metamaterials. Variations in membrane thickness have dual effects on the sharp Fano-like resonance. First, decreasing the membrane thickness will gradually raise the sharp resonance frequency. As shown in Figure 2-7(a), the sharp resonance originally located at 0.81 THz blue shifts with decreasing membrane thicknesses. This is because the resonant electromagnetic field permeates through the thin membrane and interacts with the ambient air below the membrane. This leads to an effective substrate medium with a reduced effective permittivity when accounting for the contributions of both the membrane and the "lossless" air. Thus decreasing the membrane thickness will gradually reduce the effective permittivity of the membrane-air resulting substrate and hence will blue-shift the resonance frequency. Secondly, a thinner membrane implies a less lossy medium interacting with the electromagnetic field, hence diluting the dielectric loss associated with the effective membrane-air substrate. As shown in Figure 2-7(b), this effect leads to an enhancement in both the resonance strength and *Q*-factor of the sharp resonance with decreasing membrane thickness. Therefore, the issue of dielectric loss hindering the high-*Q* resonance in the bulk media could be resolved in membrane substrates with decreasing thicknesses.

However it should be pointed out that the conventional photolithography technique is difficult to apply for the ultrathin polymer substrates (less than 10 μm) due to the issue of thermal expansion mismatch between polymer membranes and coated photoresists, which may seriously influence the quality of the sample fabrication. We plan to use a simple and low-cost photoresist-free shadow mask technique to fabricate future optimized ultrathin devices, where no thermal processing is involved. Besides the optimization of fabrication technique, further optimized design of high-Q membrane devices should consider various factors such as the geometry of the resonator, the dissipation losses of metals and substrates, and the thickness of the membranes substrates, all these elements should work synergistically to achieve well performed devices, however the further optimized device is beyond the scope of this paper and will be presented in a separate work. We believe that the above studies can expand our understanding on the resonant properties of membrane based high-*Q* resonators, and pave the way to the engineering and optimization of the resulting functional devices, such as terahertz filters and sensors.

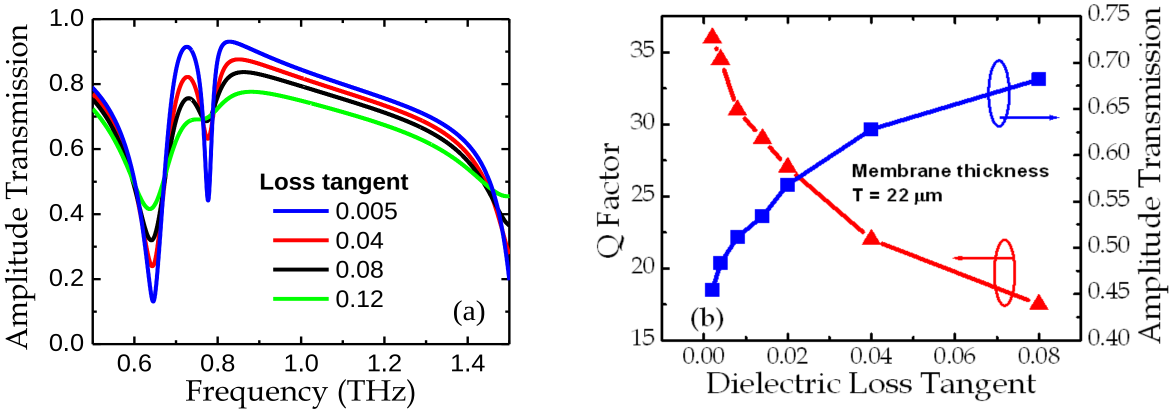

Figure 2-6 (a) Resonant properties with respect to the dielectric loss of the membrane substrate. (b) Loss-dependent resonant strength and *Q*-factors of the sharp resonance. The resonator geometry is fixed, with *D* = 5 μm.

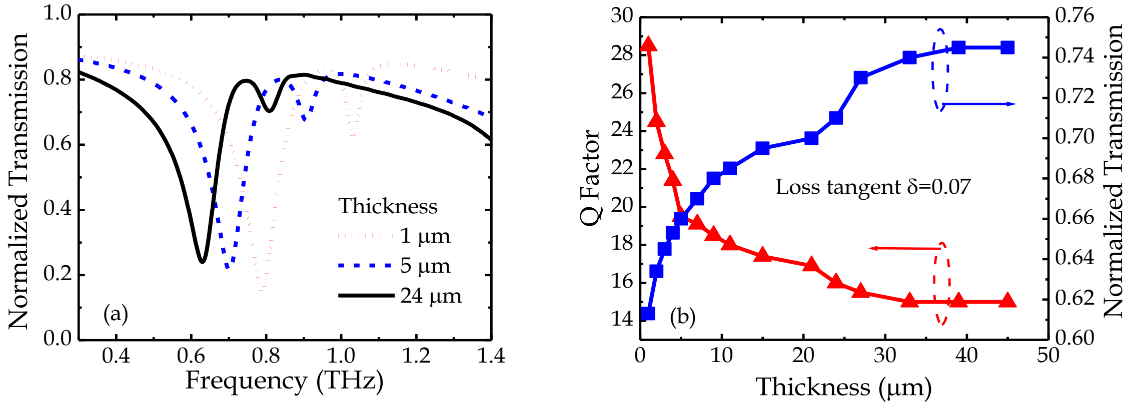

Figure 2-7 (a) Resonant properties with respect to the thickness of the membrane substrate. (b) Thickness-dependent resonant strength and *Q*-factors of the sharp resonance. The resonance strengths for various membrane thicknesses are represented by the normalized transmission, which is defined by the amplitude transmission at the resonance dips of resonators normalized over that of a blank membrane substrate with an identical thickness. The resonator geometry is fixed, with *D* = 5 μm.

2.3 Enhanced performance of sensing in membrane metamaterial resonators

To demonstrate the potential of using membrane metamaterial resonators in sensing, a layer of photoresist S1813 of 1 μm thickness, acting as the analyte, was spin-coated on the surfaces of the ER resonators fabricated on both the 22-μm-thick Mylar film and a double side polished silicon wafer of 540 μm thickness, respectively. In order to accurately characterize the sharp resonance and the small frequency shift, the silicon resonator device is optically contacted to a 10-mm-thick high resistivity, double side polished silicon wafer to suppress Fabry-Perot oscillations. The frequency shift of the sharp Fano-like resonances is monitored via the THz-TDS transmission spectra. As shown in Figure 2-8(a), the dielectric layer coated on the silicon based resonators results in a 7 GHz red-shift for the sharp resonance. In contrast, the dielectric layer applied on the membrane based resonators delivers a 40 GHz red-shift, as shown in Figure 2-8(b), indicating a significantly improved sensing performance.

The physical reason that membrane resonators have better sensitivity compared with the resonators fabricated on silicon can be explained as following: The double-gap ERs patterned on the substrates behave as *RLC* resonators, where the shifts of resonance frequencies are induced by the capacitance changes of sensing targets, this is the key to implement the metamaterial sensing [73]. High-permittivity silicon substrate contributes a dominant capacitance to the resonators; therefore the shifts of resonance are insensitive to the small capacitance changes induced by the sensing targets. The membrane substrates with low permittivity such as Mylar contribute less capacitance to the resonator, and therefore the resonance shifts induced by the capacitance change of targets are increased and results in an enhanced sensitivity. Moreover, as demonstrated in the above section, when accounting for the contributions of both the membrane and the air, decreasing the thickness of membrane substrates can reduce the effective permittivity of substrates and hence may increase the shifts of the resonance as well as sensitivity.

Furthermore, we explore the influence of the membrane thickness on the sensitivity to the analytes. Here the sensitivity $S = \Delta f / (\Delta n \cdot t)$ is defined by the resonance shift Δf per refractive index unit Δn at a thickness t [82]. Figure 2-9 shows the simulated thickness-dependent-sensitivity for the Mylar substrate coated with a 1 µm S1813 photoresist layer with a refractive index n = 1.65 [90]. The sensitivity monotonically increases with decreasing membrane thicknesses. A sensitivity saturation effect is also observed when the thickness of the membrane is larger than 50 µm. In Figure 2-9, it is observed that an ultrathin membrane device with 500 nm thickness enables a sensitivity $S = 4.7 \times 10^{-2}\, GHz/nm$, which is more than an order of magnitude enhanced over that of silicon based resonators (with a sensitivity $S = 0.43 \times 10^{-2}\, GHz/nm$). This is consistent with the experimental results using membranes with several hundred nanometers thicknesses [82]. The dependence of the sensitivity on the membrane thickness also reveals that our high-*Q* membrane metamaterial sensors with a moderate thickness (ranging from 10 to 50 µm) can be a good compromise to the ultrathin devices (hundreds of nanometers thickness) previously proposed. The sensitivity for a 20 µm thick Mylar membrane is $S = 2.4 \times 10^{-2}\, GHz/nm$, however, when the thickness is reduced to 500 *nm*, the sensitivity becomes double, i.e. $S = 4.7 \times 10^{-2}\, GHz/nm$. This is a relatively unremarkable advantage when compared to the use of moderately thick (10-50 µm) membranes, which could greatly simplify device fabrication, and lower the corresponding cost of such high-*Q* membrane sensors for realistic applications. In turn, this may also solve the issues related to the use of ultrathin-membrane based metamaterial devices, where a very limited sample size and complication in fabrication processes may significantly increase the difficulties and costs towards real life device applications.

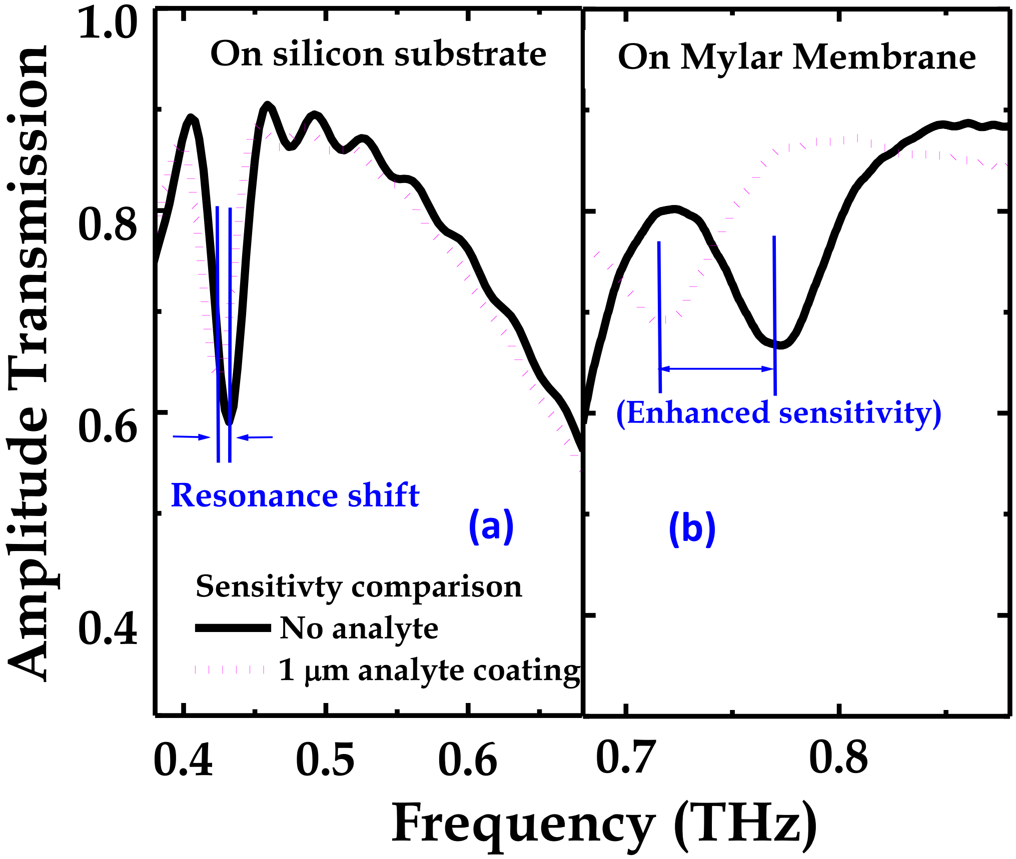

Figure 2-8 THz-TDS measured transmission spectra of the resonators fabricated on Si substrates and thin Mylar films, respectively, with and without photoresist coating. Again, the resonator geometry is fixed, with $D = 5$ µm. (a) sensing response obtained with a high-Q LC resonance on a Si substrate, (b) sensing response obtained with a high-Q LC resonance on Mylar films.

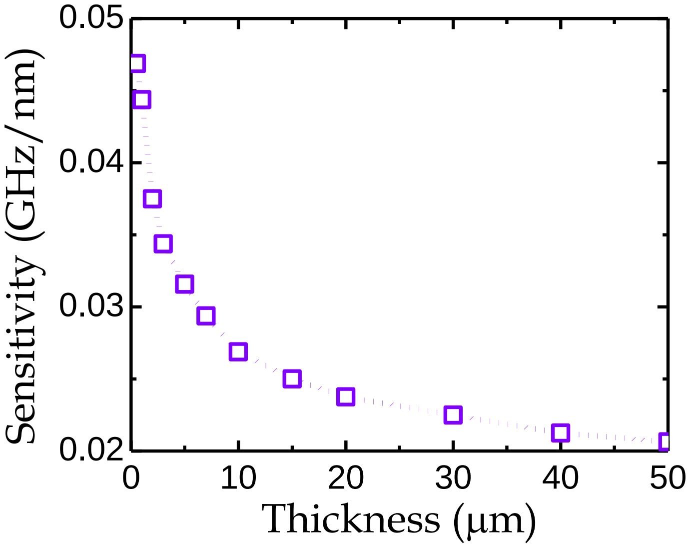

Figure 2-9 Simulation result of membrane thickness-dependent sensitivity.

2.4 THz slow light chips based on planar metamaterials

Slow light technology is to control and slow down the propagation speed of light signals. As an emerging new field, slow light is not only conceptually fascinating but also has important applications, such as optical communications, signal data manipulation, and quantum information processing [47-49]. However, currently in the THz regime, there is a lack of technologies to implement effective slowing down the THz light, as well as a lack of materials that are suitable to achieve high efficiency slow light devices. It is thus of great interest and merit to bridge between the fields of metamaterials and slow light, which may pave a way for developing new research directions and important applications.

In this section, we explore the possibility to control the speed of THz wave through the planar metamaterial slow-light chips. A systematically experimental method based on THz-TDS is designed to study the slow-light phenomenon and evaluate the performance of slow light devices (systems) in the THz region. It is proposed that the active control of THz slow light can be achieved through a chip comprised of planar metamaterials on the substrates based on the photo-excitation of carriers into semiconductor substrates.

An unambiguous and systematic experimental method to study the slow-light phenomena is essential to reveal the underlying physics, and to evaluate the performance of slow light devices (systems) in the THz regime. Here, we propose that THz-TDS is an ideal experiment tool for this purpose. We suggest that three factors can be given by THz-TDS as the measures of performance for the THz slow-light devices.

(1) Time delay: The time delay of THz signal passing through the slow light device is an important measure of performance. In order to gain the time delay information within a broad

spectrum, we use group delay as a measure of the transit time of signals through the device versus signal frequency. The group delay is related to the frequency derivative of the transmission signal phase shift.

$$T_g = -\frac{d\varphi(\omega)}{d\omega} \quad , \tag{2-1}$$

where $\varphi(\omega)$ is the phase shift of light single pass through the device at specific center frequency, and ω is the angular frequency. The group delay T_g as a measure has several merits since it can be applied to slow light devices, such as waveguides with a much larger spatial size than the wavelength of operation signal along the propagation direction, and also suitable to the chip-scale configurations where the device size is much smaller than the wavelength of the signal. Also, it has no limitation to characterize the nonuniform devices such as tapered waveguides, where both the group velocity and the group index are not appropriate as a measure for the nonuniform slow light system.

(2) Transmission loss: Light signal may attenuate after passing though a slow-light element. The transmission loss is given as a figure of merit to evaluate the device loss which limits the system performance, and can be derived by the equation:

$$L = \left|\frac{O(\omega)}{I(\omega)}\right|^2 \quad , \tag{2-2}$$

where $I(\omega)$ and $O(\omega)$ are the complex amplitudes of the input and output signal.

(3) Signal distortion: The original waveform of the input signal may be altered comparing with the output signal after propagation through slow-light devices. The signal distortion will degrade the performance of slow-light systems and should be evaluated to optimize the device design. . By using the system response function $H(\omega)$ which is derived by the broadband THz-TDS

measurement (the details are not shown), a constructed input signal with a designed waveform can be used to derive the output signal after passing through the slow light systems,

$$p(t) = \int_{-\infty}^{\infty} H(\omega) \cdot \left[\tfrac{1}{2\pi} \int_{-\infty}^{\infty} s(t) e^{i\omega t} dt \right] \cdot e^{-i\omega t} d\omega \ , \qquad (2\text{-}3)$$

where $s(t)$ is the constructed input signal with a designed waveform, and $p(t)$ is the output signal. In this way, the waveform discrepancy between any input and output signals can be analyzed to evaluation the distortion.

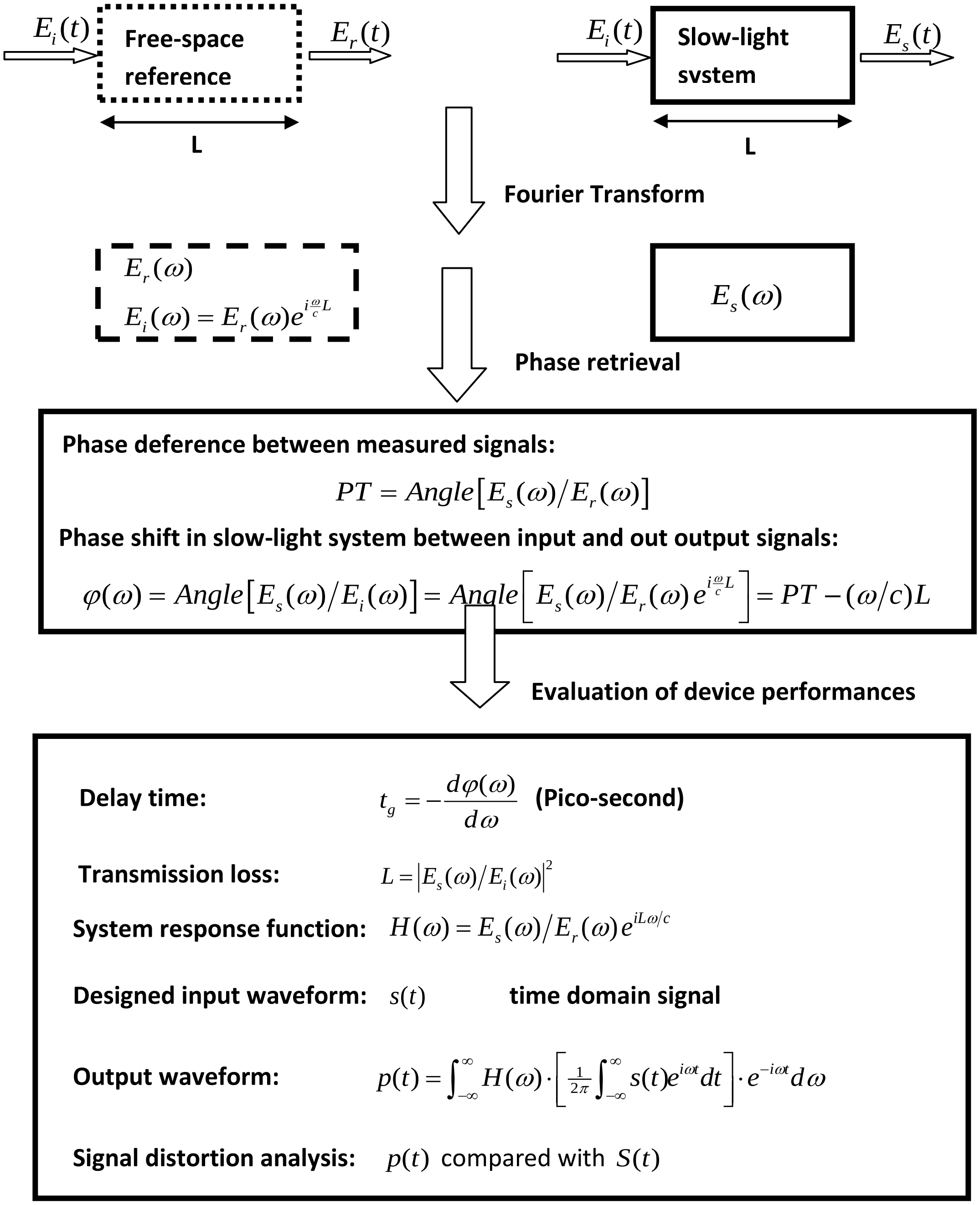

Figure 2-10 Schematic of THz-TDS slow light measurement.

As we discussed above, in order to evaluate the performance of THz slow-light devices we need to acquire three factors which can be characterized by the THz-TDS system. As illustrated in Figure 2-10, the physical size of slow-light system along the propagation direction is assumed as **L.** In the time domain, we measure the amplitudes of THz pulses passing through the free-space reference and the slow light devices, respectively, and then using the Fourier-Transform to obtain the spectra for both of the signals. Here, the initial input signals for the reference and slow-light system are identical and denoted by $E_i(t)$, the pulse signals of free-space reference and slow-light system are $E_r(t)$ and $E_s(t)$ corresponding to the frequency spectrums $E_r(\omega)$ and $E_s(\omega)$, respectively. The phase shift in slow-light system between the input and output signals is retrieved from the Fourier analysis, by using Equations (2-1) and (2-2), we can implement the analysis for the time delay, transmission loss and signal distortion to evaluate the performance of slow-light devices.

As an example, a recent proposed planar slow-light metamaterial [57] is characterized by the THz-TDS measurement. The meta-material is consisted of a unit cell where a SRR is surrounded by a larger closed ring with structure parameters shown in Figure 2-11(a). As shown in Figure 2-11(b), the coupling or interference effect between the inner SRR and outer closed ring lead to a narrow resonance associated with a transparent window where the strong dispersive behaviour contributes to the delay of the light. Through THz-TDS measurement, the time-delay and transmission loss are achieved to characterize the performance of the slow-light metamaterial. Through the measurement we can obtain the corresponding time-domain signals shown in Figure 2-12(a), consequently, the spectrum and phase information can be derived by Fourier transform, and the time delay and transmission loss are achieved from the THz-TDS slow-light measurement, as illustrated in Figures 2-12(b) and (c).

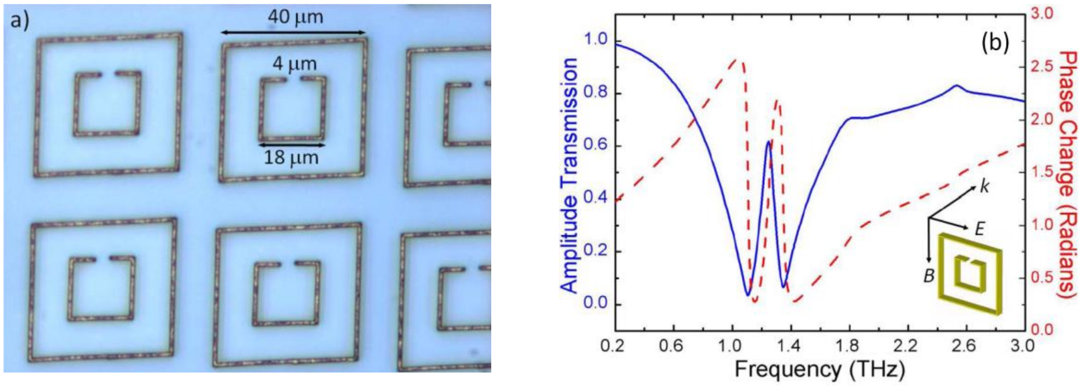

Figure 2-11 (a) Structural parameters of the unit cell. (b) Amplitude transmission (solid curve) and corresponding phase change (dashed curve) of the metamaterial schematically illustrated in the inset [57].

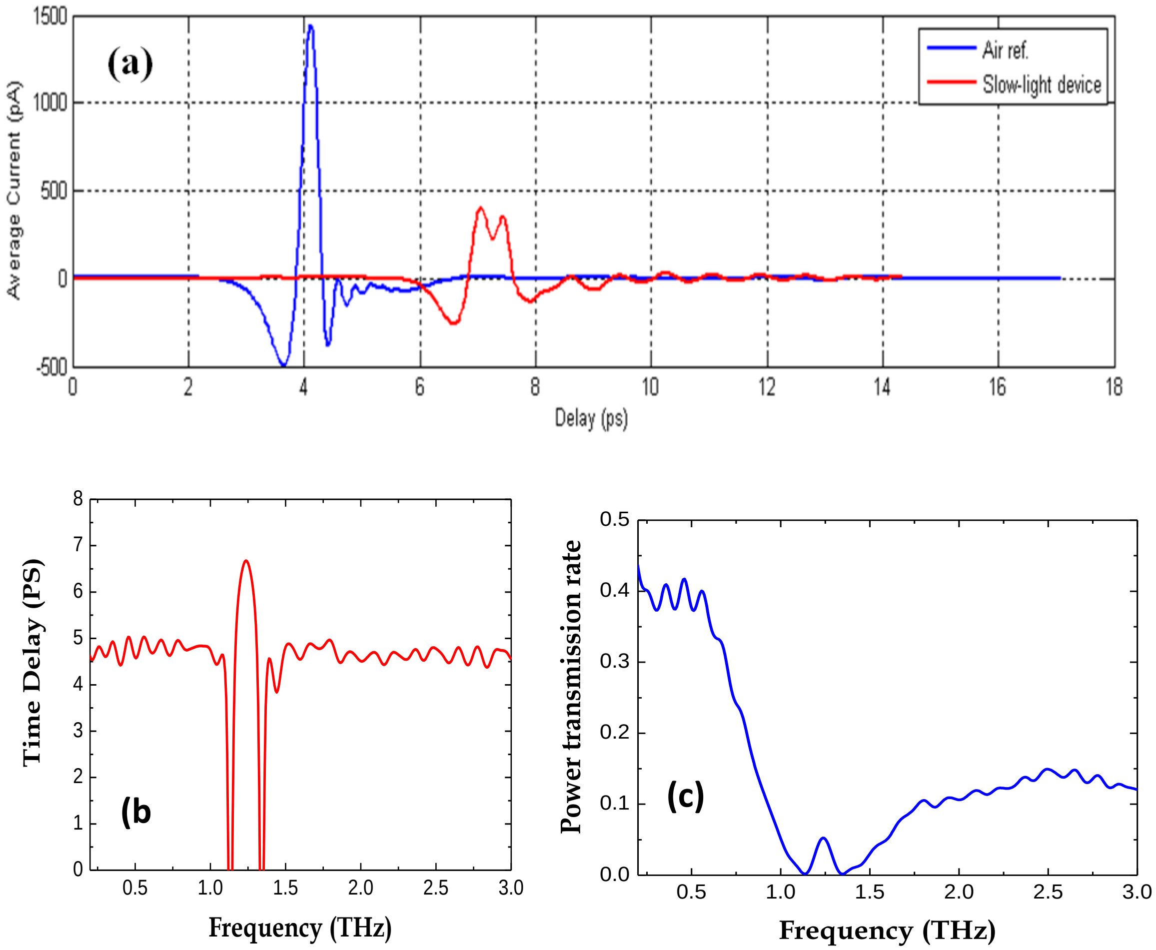

Figure 2-12 (a) Reference pulse (blue line) and slow-light pulse (red line). (b) Measured time Delay of THz wave passing through the slow-light metamaterial. (c) Transmission loss of slow light.

2.5 Conclusion

We investigate the resonant properties of membrane metamaterial resonators operating in the terahertz regime. The effects associated with the geometry of the resonators and the dielectric loss and thickness of the membranes are shown to significantly influence the resonance strength and Q-factor of the sharp Fano-like resonance. We demonstrate that membrane based high-Q resonators may overcome the limitations of the counterparts fabricated on conventional thick substrates and as such, they are very promising tools towards the development of high-performance integrated terahertz filters and sensors.

CHAPTER III

METAMATERIAL WAVEGUIDES TOWARDS THE EXTREME MANIPULATION OF THZ RADIATION

The planar metamaterials can just modestly control electromagnetic waves due to the limited wave-matter interaction length. They are incapable to implement the extreme manipulations of light, such as light trapping/storing, stopping/releasing, which are very promising in the application of optical communications, optical signal data manipulation, quantum information processing and nonlinear optics. In this chapter, I present a comprehensive theoretical study of anisotropic metamaterial waveguides, which exhibits strong wave dispersion and trapping behavior. Further proposed microscopic model reveals the underlying mechanism of light trapping, and affect further engineering of active metamataerials for the transitions between light trapping and releasing. This extreme manipulation of light implemented by metamaterial waveguides is not only conceptually fascinating, but also opens the door for a broad range applications, including optical delay-lines, all optical routers, ultra-broadband absorbers, sensitive detectors and optical sensor benefited from the enhanced light-matter interaction in metamaterial waveguides. Parallel-plate waveguide combined with photonic crystals are also proposed to realize the waveguide switch and modulator, and are expected to be useful in tunable quantum cascade lasers

3.1 Trapping THz radiation in metamaterial waveguides

It is known that metallic subwavelength structures have recently attracted numerous attentions for their great potential in developing novel devices and artificial materials with unique electromagnetic response. Notable examples include negative index metamaterials [29-31], effective plasmonic crystals [20], and high index metamaterials [91-93]. It is of great interest and merit to bridge between the fields of metamaterials and slow light, which may pave a way for developing new research directions and important applications. Recent progress on slow light in artificial plasmonic structures [51,52], electromagnetically induced transparency in metamaterials [53-57], and “trapped rainbow” in tapered negative index waveguide [58] have demonstrated new scopes and possibilities in both metamaterial and slow light.

In this section, we demonstrate that metamaterial waveguides comprised of tapered cut-through metallic systems can spatially trap different frequency components of an electromagnetic wave. By adding an elastic property to the waveguide, the resulted effective elasto-optic effect enables a transition between the states of light trapping and releasing. More fundamentally, we show that the mechanism of light trapping and releasing is governed by the local Bragg condition and cavity resonance of the waveguide. The light trapping and releasing approach can be exploited in developing novel devices for active control of light speed in a broad spectrum range.

A heterostructured metamaterial waveguide as a typical two dimensional cut-through metallic system, as illustrated in Figure 3-1, is comprised of two dielectric claddings and a metamaterial core formed by arrays of metal slats. Such a cut-through design, which has no closing metal substrate, enables mechanical or elastic tuning. Here, we focus on the frequency band from microwave up to the threshold of the THz regime where metals can be treated as perfect conductors. A light wave with TM polarization propagating along the waveguide, and the wavelength of light is assumed to be much longer than the slit width. In region I, the field inside the slits can be expressed as a combination of forward and backward TEM subwavelength propagating modes. In regions II and III , the fields are a sum of diffractive waves, which should be evanescent in the dielectric claddings to maintain the bounded guiding wave along the waveguide. By matching boundary conditions for both electric and magnetic fields at the interfaces between different regions, we can deduce the following equations,

,

$$\sum_{n=-\infty}^{\infty} \varepsilon_2 \frac{d}{p} \frac{\sin c^2(\frac{\beta_n d}{2})}{\tau_{(2,n)}} = -\frac{\varepsilon_1}{k_1}\left[\frac{A\sin(\frac{k_1 L}{2}) - B\cos(\frac{k_1 L}{2})}{A\cos(\frac{k_1 L}{2}) + B\sin(\frac{k_1 L}{2})}\right]$$

, (3-1)

$$\sum_{n=-\infty}^{\infty} \varepsilon_3 \frac{d}{p} \frac{\sin c^2(\frac{\beta_n d}{2})}{\tau_{(3,n)}} = -\frac{\varepsilon_1}{k_1}\left[\frac{A\sin(\frac{k_1 L}{2}) + B\cos(\frac{k_1 L}{2})}{A\cos(\frac{k_1 L}{2}) - B\sin(\frac{k_1 L}{2})}\right]$$

where *p* and *L* are the periodicity and thickness of the metal slats, respectively, and *d* is the width of slits. $k_i = \sqrt{\varepsilon_i}\, \omega/c$ is the wave-vector in different dielectric regions with dielectric constants ε_i , and $i = 1, 2, 3$ represents regions I, II and III, respectively. ω is light frequency and c is the speed of light in vacuum. $\beta_n = \beta + n\frac{2\pi}{p}$ $(n = -\infty, ...0, ... + \infty)$ is the momentum along the *z* direction of the nth diffraction order of guided waves with β the propagation constant. $\tau_{(i,n)}^2 = k_i^2 - \beta_n^2$ is the transverse momentum along the *x* direction and $\beta_n > k_i$ for evanescent diffractive waves. *A* and *B* are coefficients. The dispersion relation of the waveguide can be derived by solving Equation (3-1).

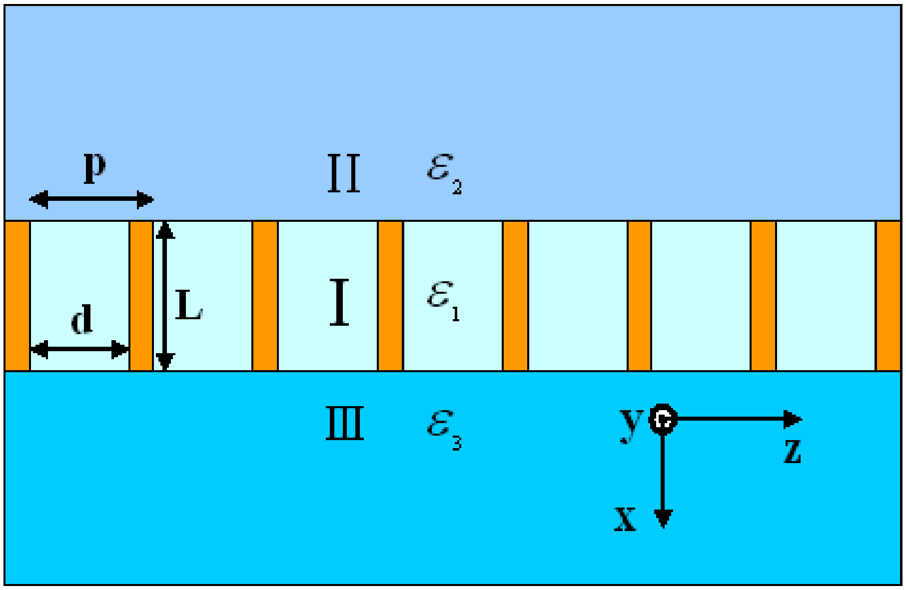

Figure 3-1 Schematic of the heterostructured waveguide consists of dielectric claddings and a metamaterial core formed by arrays of metal slats (yellow).

The mechanism for light trapping and releasing in the metamaterial waveguide is governed by both the local Bragg condition and cavity resonance, which exist in the tapered periodic cut-through metallic system. Our goal is to explore the insight into the physics of wave propagation in the tapered waveguide. We first assume that the thickness variation along the propagation axis is much smaller than the wavelength and the wave guiding is thus along a locally uniform grating structure, as depicted in the inset of Figure 3-2. The Bragg condition occurs when the wave vector of the guided mode is at the Brillion Zone Boundaries where the dispersion curve becomes discontinuous and approaches the band-edge.

It is noted when light propagates along the waveguide, the tapered structure will gradually couple light into the guided mode with wave vectors approaching the Brillion Zone boundaries, thus may resolve the issues of mode coupling and momentum mismatch. Figure 3-2 shows the dispersion relation of the fundamental mode in the first Brillion Zone at the zone boundary where $k_z = \frac{\pi}{p}$. Now, we consider guided waves supported by a section of local uniform metal slats, the propagation wave vectors satisfy the Bragg condition, $\overrightarrow{k_z} = \beta_{Bragg} = \frac{\pi}{p}$ (the higher order Bragg vectors are neglected as an approximation), as shown in Figure 3-3, the waves will be reflected back during the forward propagation along z axis and form the backward propagation wave, which is equal to the forward wave but with an opposite wave vector $\overleftarrow{k_z} = -\frac{\pi}{p}$. The superposition of such forward and backward waves forms a standing wave with stationary fields around the waveguide.

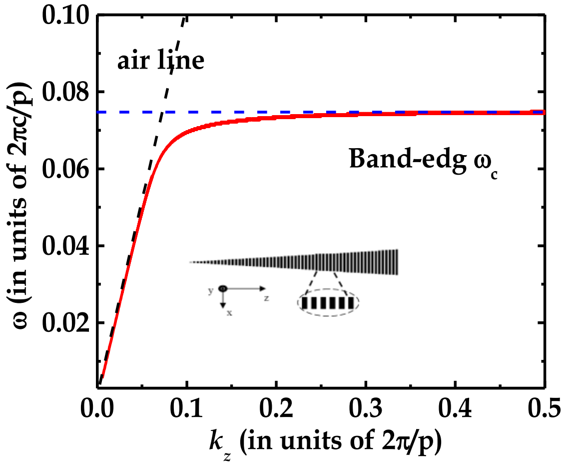

Figure 3-2 Dispersion relation in the first Brillion Zone of the fundamental mode supported by the metal slat waveguide with geometry parameters, $\frac{p}{d}=7$,and $\frac{L}{d}=45$.

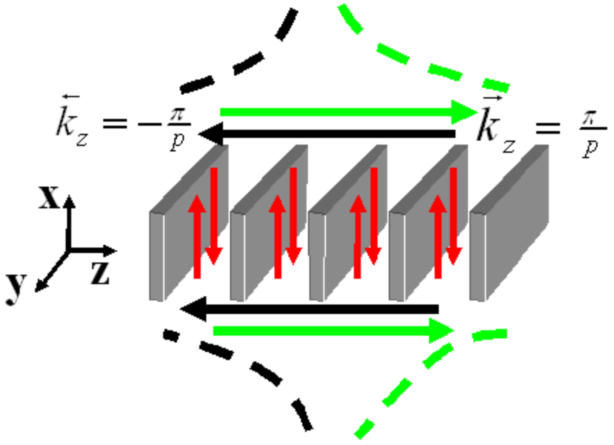

Figure 3-3 Light trapping governed by the local Bragg condition and cavity resonance. The green and black arrows represent forward and backward guided-waves along z axis, the evanescent fields along x direction are represented by green and black dashed curves. The cavity resonances (light trapping) inside the metal slits are indicated by the red arrows.

Moreover, along x direction, the fields inside the metal slits are formed by the oscillating subwavelength modes, and the fields outside the slits are formed by stationary evanescent waves, thus maintaining the highly confinement of light around the slits and create a nonradiative local cavity resonance inside the slits and trap light in these cavities, as shown in Figure 3-3. It should be emphasized that although the waveguide analyzed here is two-dimensional, by exploiting the existence of local Bragg condition and cavity resonance in three dimensions in the tapered cut-through metallic system, the mechanism and concept can be generalized to the three dimensional waveguides comprised of periodic metal pieces or particles. It is expected that the variations of local geometry by the mechanical or elastic tuning will change both the local Bragg condition and cavity resonance of the waveguide and influence the light trapping effect. The light trapping in the tapered waveguide can be described by an analytical formula,

$$\left[\beta_{Bragg}^2 - (\tfrac{\omega}{c})^2\right]^{-\frac{1}{2}} \sin c^2(\tfrac{\beta_{Bragg} d}{2}) = \frac{p}{d}\frac{\cot(\frac{\omega}{2c}L)}{\frac{\omega}{c}}, \tag{3-2}$$

where the left side term is dominated by the local Bragg condition $\beta_{Bragg} = \frac{\pi}{p}$, and the right side term represents the cavity resonance depending on the local geometry characterized by the local periodicity p, thickness L, and slits width d. Equation (3-2) accounts for contributions of both local Bragg condition and cavity resonance. It is derived from Equations (3-1) in which higher order diffraction waves are neglected as an approximation on the condition that the wavelength λ_o of light is much larger than the slat periodicity p, and by considering the Bragg condition $\beta_{Bragg} = \frac{\pi}{p}$ as well as local geometrical structure of the waveguide. From Equation (3-2) we can find that different frequency components ω of the guided waves are trapped at corresponding sections of the waveguide with different thicknesses L. In addition, the "rainbow phenomenon" of the waveguide which is related to the spatial separation of different light frequencies, can also be verified by the above light trapping equation. We assume that the waveguide is linearly tapered with a small tapering angle α, and the variation in waveguide thickness L along the propagation axis z can be approximately expressed as $L = \alpha z$. By substituting the above relation in Equation (3-2), one can obtain the following “Rainbow Equation”,

$$\left[\beta_{Bragg}^{2} - (\tfrac{\omega}{c})^{2}\right]^{-\frac{1}{2}} \sin c^{2}(\tfrac{\beta_{Bragg} d}{2}) = \frac{p}{d}\frac{\cot(\frac{\omega\alpha}{2c}z)}{\frac{\omega}{c}}\,. \qquad (3\text{-}3)$$

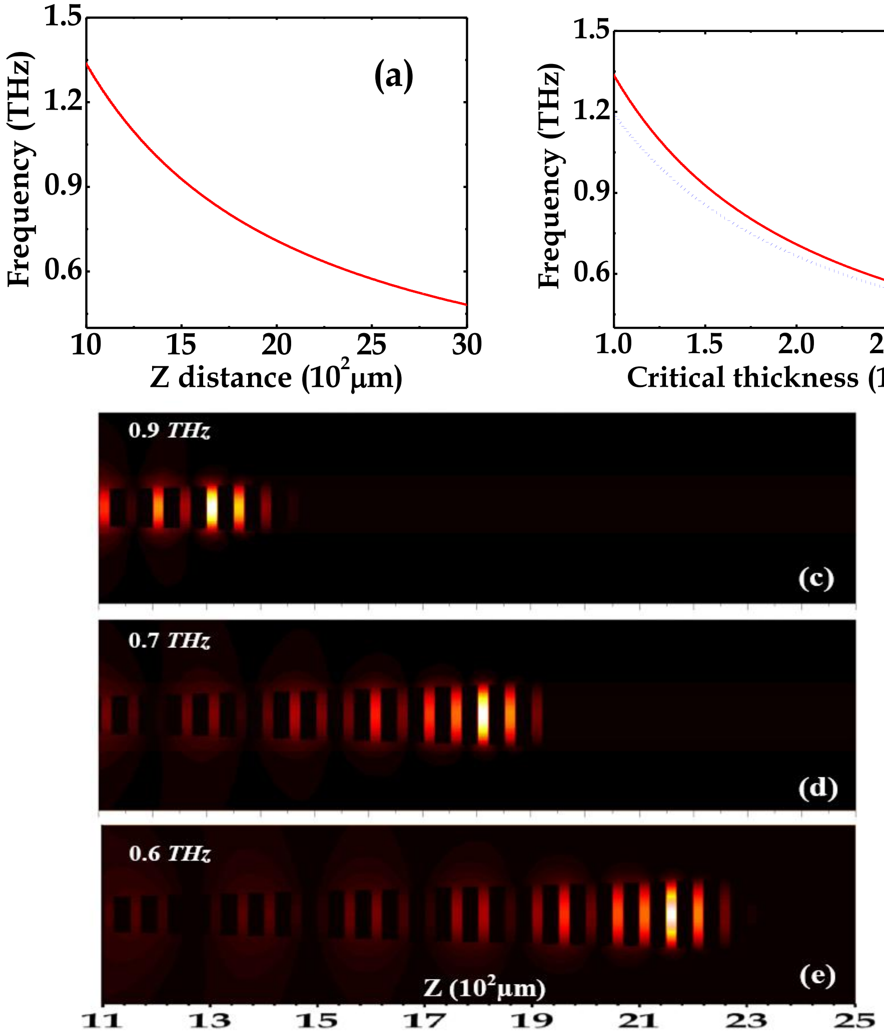

Figure 3-4 (a) "Rainbow phenomenon" of the waveguide. (b) Trapping light at different critical waveguide thicknesses. The solid curve is derived from Equation (3-3) as an approximation. The dotted curve considers the higher order diffraction waves for comparison with the approximation. The geometry parameters are chosen as $p = 50$ μm, $d = 20$ μm, the length of the waveguide along the propagation axis is 3000 μm including 60 metal slats, and the slat thickness L increases from 5 to 300 μm by a step of $\Delta = 5$ μm for each period. (c)-(e) The frequencies of trapping light at $f = 0.9$, 0.7 and 0.6 THz correspond to the critical thicknesses $L = 140$, 190 and 225 μm, respectively. The field distributions are represented by the magnetic field of light.

The Equation (3-3) predicts the spatial separation of different frequency components along the propagation axis, *z*. Figure 3-4(a) illustrates the "rainbow" phenomenon along *z* axis, where light trapping at different critical waveguide thicknesses is observed, as shown in Figure 3-4(b). Here, we employ the normalized length $L_o = 1$ in order to facilitate the Scaling-Laws scaled to the frequency range from microwave to the THz regime. In the practical application the normalized length L_o will be assigned the real length units depending on the size of working space. It should be noted that in order to accurately determine the critical thickness, one needs to consider higher order diffraction waves compared to the approximation in Equation (3-3); this is well verified by the FDTD simulations. As shown in Figures 3-4 (c)-(e), for instance, in the units of $L_0 = 10^2$ μm the frequencies of trapping light at f = 0.9, 0.7, and 0.6 THz are spatially separated corresponding to the critical thicknesses at L = 140, 190, and 225 μm, respectively.

3.2 Releasing THz radiation in metamaterial waveguide

After trapping light in the waveguide, we now show how to release light using the effective elasto-optic effect. As mentioned above the metal slats are designed to possess elastic property, and the geometrical parameters such as periodicity p and slit width d can be varied by compressing or stretching the metal slats along the propagation axis. The effective index $n = p/d$ can be regarded as a parameter associated with the elasto-optic effect. The variations of local geometry will change both the local Bragg condition and cavity resonance of the waveguide and influence the light trapping effect derived from Equation (3-3). Figure 3-5(a) illustrates the variation of light trapping at different waveguide thicknesses through compression of the tapered section. By compressing the slats along z axis, the trapped light at corresponding waveguide thickness blue shifts. Meanwhile, in the dispersion diagram of a section of uniform waveguide, as shown in Figure 3-5(b), for the relaxation state without any compression, the dispersion curve of the trapped light approaches cutoff frequency (band-edge) and its slope is nearly flat, indicating a close to zero group velocity. However, by compressing the waveguide, light releasing occurs as evidenced by the fact that the slope of the dispersion curve for the same frequency region becomes obviously tilted. Since the elastic element can be compressed and restored, light trapping and releasing are reversible states. The dynamic transition between the two states leads to deceleration and acceleration of light propagating along the waveguide.

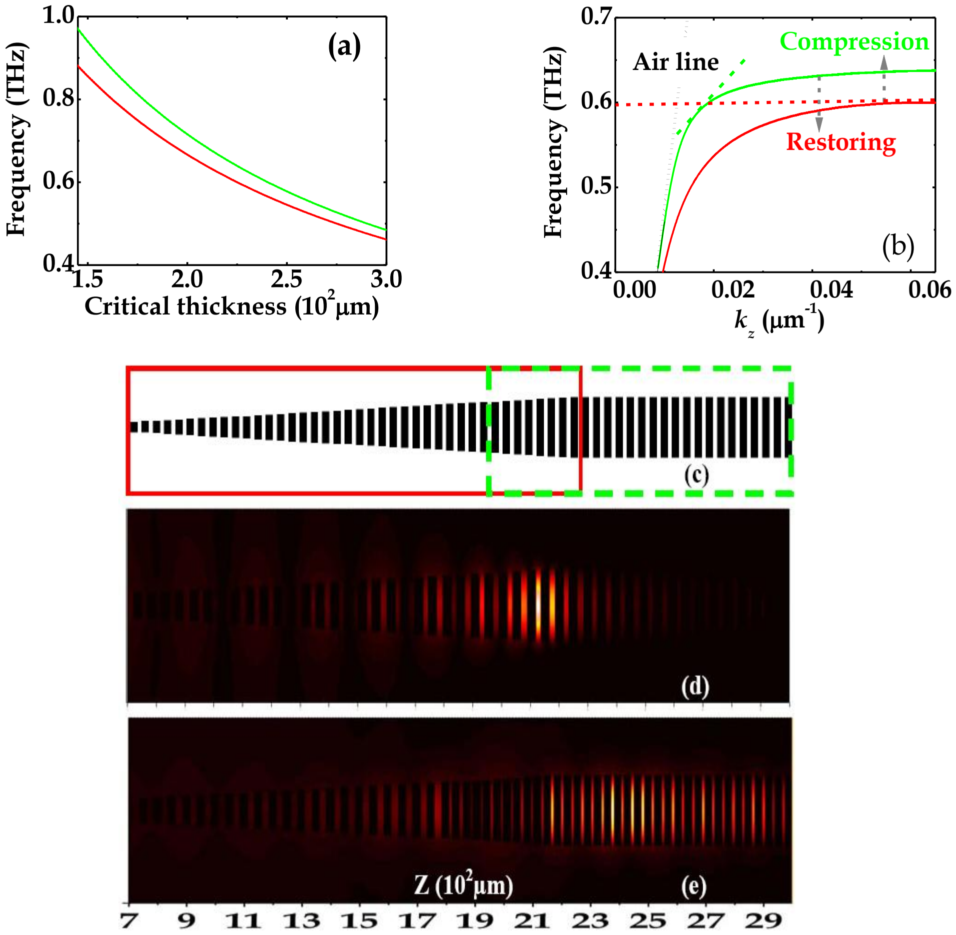

Figure 3-5 (a) Variation of trapping light at different waveguide thicknesses through compressing the tapered region. The waveguide structure is same as that in Figure 2. The periodicity and slit width are changed from p = 50 µm, d = 20 µm (red curve) to p = 35 µm, d = 5 µm (green curve) due to compression. (b) Variation of the dispersion diagram through the compression on a section of uniform metal slat array. The metal slat array has a constant thickness L = 225 µm with same periodicity and slit width in (a). The red and green dashed lines represent the slope of the dispersion curves. The transition between light trapping and releasing is reversible as indicated by the dashed arrows. (c) The tapered section for trapping light (the red box) is followed by a uniform section for extracting light. The elastic property and compression are added to the uniform section as well as the thick slats of the tapered section (green box). (d) and (e), Transition between light trapping and releasing demonstrated by FDTD simulations.

In order to implement the transition between the trapping and releasing states, the waveguide design, as shown in Figure 3-5(c), is comprised of a tapered metal slat waveguide functioning as a light trapping device followed by uniform slats with elastic and compressible properties which can extract light from the tapered section by the compression process. To explicitly demonstrate the influence of local geometry variation on the trapping light effect, the elastic and compressible properties are also added on the thick region of the tapered waveguide, which is a small section containing several metal slats, as shown in the overlap region between red and green box in Figure 3-5(c). The compression at the thick region modifies the local geometries, thus tuning the local Bragg condition as well as cavity resonance and influencing light trapping in that region.

The transition between the states of light trapping and releasing is modeled by FDTD simulations. The length of the first tapered section of the waveguide along the propagation axis is 2250 μm including 45 metal slats, and the slat thickness L increases from 5 to 225 μm with an interval of $\Delta = 5$ μm at each period. Following the tapered section, an array of metal slats with a constant thickness L = 225 μm forms a uniform section and has the same periodicity and slit width with those of the tapered slats. When compression applies, the periodicity and slit width change from p = 50 to 35 μm and d = 20 to 5 μm. As shown in Figure 3-5(d), for the relaxation state without compression, the light with frequency 0.6 THz is trapped at the end of the taped section, corresponding to the critical thickness L = 225 μm. In Figure 3-5(e), by compressing the uniform and tapered thick region, as shown in the green box of Figure 3-5(c), the trapped light is released from the confinement region and propagates along the uniform section.

3.3 Electric field enhancement and active slow light waveguide based on the MEMs tuning

Besides the 2D planar geometries described above, metamaterial waveguides are an alternative approach in developing THz slow-light devices. Recently, we demonstrated that light trapping and releasing can be realized in a THz metamaterial waveguide based on a synergetic effect of Bragg reflection and cavity resonance [94]. As a proof-of-concept demonstration, a heterostructured metamaterial waveguide comprised of dielectric claddings and a tapered metamaterial core formed by arrays of metal slats was analytically and numerically investigated. To continue this effort, we propose to systematically investigate novel slow light mechanisms with a goal of experimentally implementing THz slow light devices in metamaterial waveguides. Specifically, we plan to develop on-chip active control of THz slow light using MEMS devices integrated onto metamaterial waveguides. We also expect to achieve slow light induced field enhancement in the waveguides, which could significantly enhance the light-matter interaction at THz frequencies [95-97]. THz wave trapping, releasing, and the resulted field enhancement are quite interesting phenomena that have not yet been explored and will have promising applications in developing tunable delay lines and optical buffers in THz communications, and nonlinear THz spectroscopy.

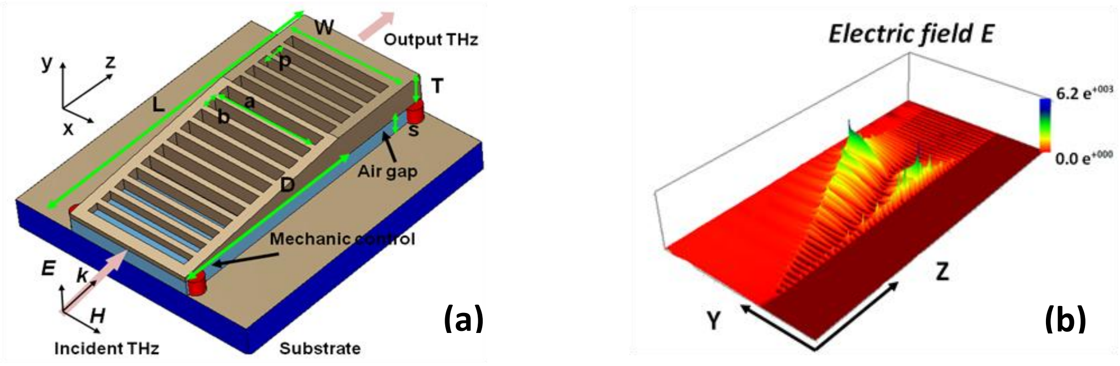

Figure 3-6 (a) Schematic of a metamateiral waveguide comprised of a metallic wedge of periodic slots and a coated substrate. A 300 nm metal layer is deposited on the dielectric substrate. The length and width of the guided region are *L* = 15 mm, *W* = 12 mm, respectively. The thickness *T* of metal wedge various from 4 (tapered input region) to 110 μm (the output region). The width and length of the metal slots are *a* = 30 and *b* = 10,000 μm with a periodicity p = 50 μm. The substrate and metal wedge is sandwiched with a tunable air gap *s* under MEMS switching which controls the movement of the wedge along y axis. Free space THz radiation with transverse magnetic (TM) polarization is coupled from the tapered region of the waveguide. (b) The phenomenon of slow light induced electric field enhancement in the waveguide demonstrated by FDTD simulations.

Figure 3-6(a) illustrates a proposed prototype metamaterial waveguide comprised of a wedged metamateiral and a metal coated silicon substrate. The through periodic slots on the wedged metamaterial will be fabricated using laser micromachining. The plain metal film of 300 nm thickness coated on the substrate is a unique design which will highly confine the THz wave in the channel region between the substrate and wedged metamaterial, preventing the THz radiation from leaking or coupling into otherwise a dielectric substrate. The separation between the substrate and wedged plate will be controlled by high speed MEMS switching components. As recently demonstrated, the key to engineering desired optical properties of metamaterial waveguides depends on the existence of subwavelength propagation modes in the slots [91,92]. Moreover, the mechanism of light trapping/releasing relies on the balanced/unbalanced synergetic effect between local Bragg reflection and cavity resonance in the waveguide. The mechanism for slowing down the light in the proposed metamaterial waveguide is different from that in photonic crystal based slow light devices, in which the synergetic effect is missing and only Bragg reflection dominates the slow light effect .

In the proposed metamaterial waveguide illustrated in Figure 3-6(a), the transition between light trapping and releasing can be implemented by an adequate control of the separation between the wedged plate and substrate. Such a one dimensional displacement along the y direction can break the balance between the local Bragg condition and cavity resonance of the waveguide. Meanwhile, the local dispersion of light is strongly affected by the small deformation. As schematically shown in Figure 3-7(a), the slop of the trapped light is nearly flat associated with a group velocity $V_g = 0$, However, by increasing the gap between metal wedge and substrate, light releasing occurs on the condition $V_g > 0$ which is evidenced by the fact that the slope of the dispersion curve for the same frequency region becomes obviously tilted in the dispersion curve. Figures 3-7 (b) to (d) illustrates the transition of light trapping and releasing at 1 THz. Light is first trapped at a specific region in the waveguide. By opening the gap between the wedge and substrate [Figures 3-7 (c) to (d)], the trapped light is released from the confinement region and propagates forward along the waveguide. When the group velocity of THz radiation in the waveguide is gradually slowed down and eventually approaches zero, light "stops" at a particular location where the THz field accumulates, giving rise to a significant enhancement. This effect is well verified by the FDTD simulation [98]. As shown in Figure 3-6(b), in the region where light "stops", the electric field is localized at the surface of the wedge and the gap between the wedge and substrate with an enhanced amplitude which can be more than two orders of magnitude than that of the incident THz wave.

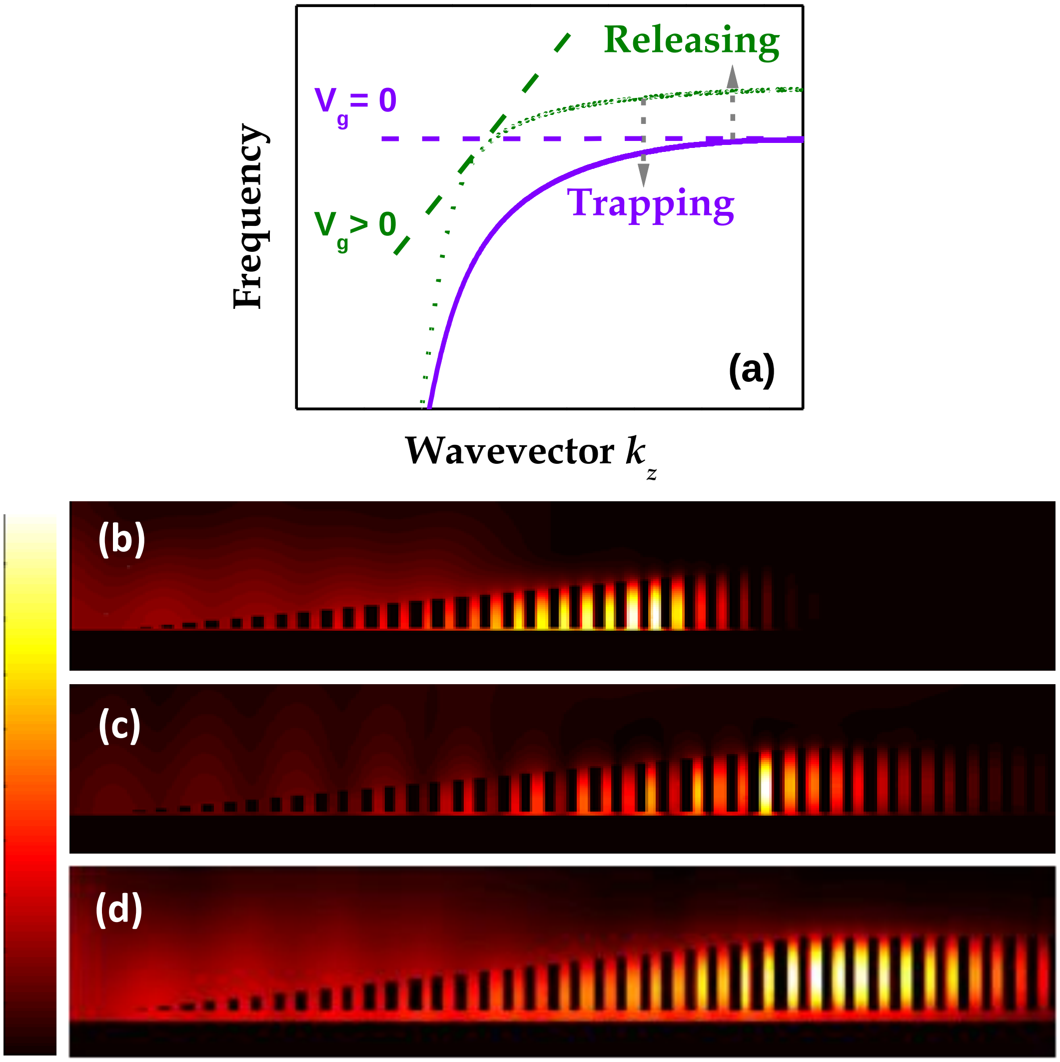

Figure 3-7 (a) Local dispersion of slow light controlled by varying the air gap between the substrate and metal wedge. (b) Light trapping in the waveguide. (c)-(d) Light releasing by gradually increasing the air gap. *s* with (b) *s* =1.5 µm, (c) *s* = 4 µm, and (d) *s* = 15 µm. The above phenomena are demonstrated by FDTD simulations. The THz wave is TM polarized and the field distributions are represented by the magnetic field.

The challenge here is the unique design and practical implementation of such prototype metamaterial waveguides which possess: (1) high free space-to-waveguide coupling efficiency and low propagation losses in the waveguide, and (2) novel MEMS components that enable high speed dynamic control of trapping and releasing of THz radiation through tuning the separation between the wedge and substrate. We plan to carry out systematic numerical simulations and use the currently well-established microfabrication techniques, including photolithography and laser micromachining to optimize the device design and fabrication. High speed MEMS switching devices will be integrated between the wedge and substrate to implement the mechanical control. To promote an efficient and broadband coupling between the free-space THz radiation and the waveguide modes, plano-cylindrical silicon lenses will be integrated at both ends of the waveguide assembly. In addition, near-field THz probes will be implemented to characterize the electric field distribution at the surface of the wedge and estimate the enhancement of the slow light signal in the waveguides.

3.4 Tunable photonic slow-light waveguides based on MEMs control

As a counterpart of metallic microstructures applied in metamaterial waveguide, dielectric composites or dielectric metamterials can also well engineer the electromagnetic properties of opto-electronic devices based on the artificial materials [69-72], and these dielectric microstructures are suitable for slow light waveguides. Since the transmitted slow light in the device have long life time, the devices coupled with slow light are very sensitive to the micro-deformation.

Here we proposed that the slow-light waveguides based on dielectric microstructures can be integrated with MEMS components on a chip to implement high efficiency on-chip switch/modulators.

As shown in Figures 3-8, the periodic dielectric array can support bandgap effect which forbids the propagation of light at certain frequency region. However, by introducing defects in the array, narrow transparency windows associated with slow light effect can be opened, and it is expected that only a small displacement of the moving plate B can efficiently switch or modulate the light propagating along the waveguide. Our preliminary numerical simulation results have well demonstrated the possibility to implement the slow light wavegude switch/modulor based on the MEMs control. As illustrated in Figure 3-8(b), the geometry parameters are: periodicity $P = 55\mu m$, a unit length of the dielectric microstructures $L = 25\mu m$, the length of a dielectric defect $D = 60\mu m$, the refractive index of the dielectric microstructures $n = 1.7$, initial gap between the two plates is H_o=13 μm. The total length of the waveguide is 8 mm. A narrow transparency window with 12 GHz bandwidth is located at 3.1 THz and associated with the propagation light in the waveguide. After pulling-in the plate B by a 500 nm displacement, the induced transparency window red shifts, meanwhile the transmission at 3.1 THz goes down to zero. The transmission modulation efficiency is defined as: $(T_{\max} - T_{\min})/T_{\max}$, where T_{max} is the transmission maximum and T_{min} is the transmission minmum at the same frequency. Although our proposed design is a preliminary test, the transmission modulation efficiency has already achieved 93% through sub-micron displacement which further adds the possibility to implement high-speed switching.

We propose to integrate other THz waveguides connected with the MEMS controlled slow-light waveguide on the same substrate to implement the high efficient light-on-chip switch and modulator. For example, as illustrated in Figure 3-8(c), the MEMs controlled waveguide combined with a metal-metal THz quantum cascade laser (QCL) can implement the external switching or amplitude modulation on a chip. Moreover, the high Q and tunable resonance of the active waveguide can be applied for tuning the frequency of THz-QCLs and thus may implement tunable THz lasers which are desirable im many application such as communication, sensing and spectroscopy. As illustrated in Figure 3-9(a). The THz-QCL metal-metal structure is located at the defect region in the active waveguide and form a cavity laser. As shown in Figure 3-9(b), the frequency of the laser associated with the resonance of the active waveguide can be shifted in a broadband range by the small displacement of the movable plate. Since the optical properties of the dielectric microstructures and geometry of the waveguide can be engineered by well-established micro-fabrication techniques, the idea of MEMs controlled waveguide switch/modulator can be extended to other frequency band in the THz region.

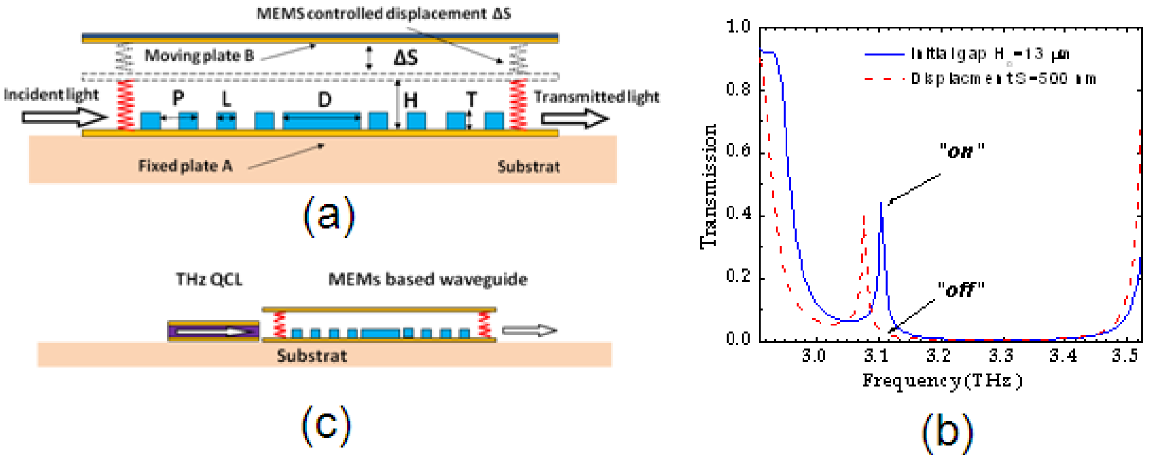

Figure 3-8 (a) a proposed prototype device, which is made from a metallic paralle plates waveguide filled with dielectric microstructures. The fixed plate A is a thin metal layer deposited on a substrate, an array of dielectric strips are fabricated on the metal surface uing convential photolithography thecnique. A thin dielectric plate coated with metals is implemented as the moving plate B. The MEMs components integrated onto the substrate separate the two plates with a gap H and will implement the vertical displacement control of moving plate B within a sub-micron range. (b) The "on/off" modulation by the shift of plat B with submicron displacement. (c) A THz Quantum cascade laser (QCL) coupled with a MEMs based waveguide modulator to implement the external waveguide switch and modulator.

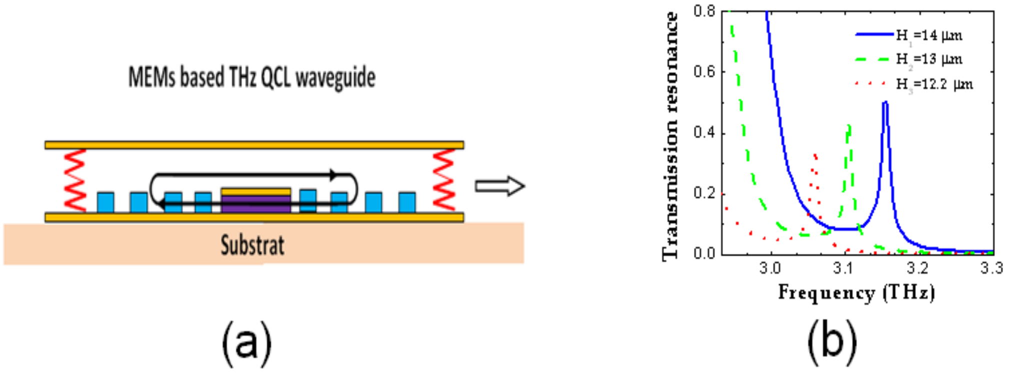

Figure 3-9 (a) Schematic of THz-QCL metal-metal structure located at the defect region in the active waveguide. (b) The frequency of the laser associated with the resonance of the active waveguide can be tuned by the small displacement of the movable plate.

3.5 Conclusion

Metamaterial waveguides are good candidate to implement the extreme control of light, such as light trapping and releasing. Our microscopic model reveals the underlying mechanism of light trapping, and assists further engineering of active metamataerials for the transitions between light trapping and releasing. This extreme manipulation of light implemented by metamaterial waveguides is not only conceptually fascinating, but also opens the door for a broad range applications, including optical delay-lines, all optical routers, ultra-broadband absorbers, sensitive detectors and optical sensor benefited from the enhanced light-matter interaction in metamaterial waveguides. Parallel-plate waveguide combined with photonic crystals is a special type of dielectric metamaterials, and are very promising to achieve tunable quantum cascade lasers.

CHAPTER IV

BROADBAND TUNABLE METAMATERIALS MEDIATED BY SURFACE WAVES

Tunable metamaterials have attracted a great attention for their promising potential in developing functional devices, such as broadband filters, switches and modulators. Currently, these functional devices are implemented by altering the effective capacitance or inductance of metamaterial resonators [37,38,100].. We demonstrate that surface wave resonance supported by the membrane metamaterials can be incorporated into the design of broadband tunable devices, and show great potential in practical applications such as broadband filters functioning in the far-infrared region. We experimentally study the role of electric and magnetic dipoles for the excitation of surface waves supported by planar membrane metamaterials. It is demonstrated that magnetic dipoles are weakly coupled with surface modes, while electric dipoles can significantly enhance the excitation of surface waves. As potential applications, we demonstrate that well-performed amplitude and phased modulation can be implemented by active control the surface mode resonances within a broadband. The physics and promising functionalities of devices make surface wave mediated metamaterials interesting and fascinating, and could be useful for broadband tunable plasmonic or metamaterial devices.

4.1 Surface modes excitation in membrane metamaterials

Besides the localized mode resonance introduced in Chapter II, surface mode resonance can also exist in the membrane-based metamaterials. The planar microstructures such as split-ring resonators (SRRs) are fabricated on membranes, and act as electric or magnetic dipoles coupled with surface modes supported in the membranes. Thus, the roles of electric and magnetic dipoles for the excitation of surface waves are crucial, and need to be explicitly explained.

4.1.1 Surface modes supported by a membrane without planar metamaterial resonators

Surface modes can exist in the membrane-based metamaterials. As shown in Figure 4-1(a), the membrane itself acts as a waveguide system where electromagnetic waves are confined in the membranes and propagate along the surfaces. The fundamental mode as well as the higher-order modes can be exited in the Membrane. As depicted in Figure 4-1(b), the transverse field distribution along X direction can distinguish different mode types. For example, the fundamental mode has a transverse field distribution with zero node along X, thus being marked as m=0 mode. Higher-order modes may have multiple nodes for the transverse field distribution. For example, the second and the third order modes have one and two field nodes in the transverse plane of waveguides, and the corresponding mode numbers are m=1 and m=2, respectively. According to the polarization states, the guided modes can be classified as TE and TM modes, as shown in Figures 4-1(c) and (d). The TE fundamental mode only has an electric filed component in Y direction thus be named as “Transverse Electrical” (TE) mode. The TM fundamental mode, named as “Transverse Magnetic” (TM) mode, indicates it has only one magnetic field component in the transverse Y direction [99].

The surface modes have corresponding cutoff wavelength λ_{cutoff} which is the maximum wavelength for a surface mode propagating in the membranes. The "cut-off" means that any surface mode with a wavelength larger than λ_{cutoff} will be prohibited propagation in the membrane and cannot resonate with external couplings. The cutoff wavelength can be predicted by the following equation:

$$\lambda_{cutoff} = \frac{W \cdot 2\pi(\varepsilon_1 - \varepsilon_2)^{\frac{1}{2}}}{m \cdot \pi + \arctan\left[C \cdot \left(\frac{\varepsilon_2 - \varepsilon_3}{\varepsilon_1 - \varepsilon_2} \right)^{\frac{1}{2}} \right]} \tag{4-1}$$

$m = 0,1,2...$

$C = 1$ For TE modes; $C = \varepsilon_1 / \varepsilon_3$ For TM modes

Where $m = 0,1,2...$ is the order numbers of surface modes, W is the thickness of membranes, ε_1 is the dielectric constant of membrane, ε_2 and ε_3 are dielectric constants of media in region II and III, respectively. For a membrane in the air environment, $\varepsilon_2 = \varepsilon_3$, the equation of cutoff wavelength can be simplified as:

$$\lambda_{cutoff} = \frac{2W(\varepsilon_1 - \varepsilon_2)^{\frac{1}{2}}}{m} \tag{4-2}$$

From the above Equation (4-2), the fundamental surface mode with $m = 0$ in the membrane waveguides has an infinite cutoff wavelength. This implies that the fundamental surface mode has no cutoff and can always exist in the waveguides. However, the resonances of higher-order modes have finite cutoff wavelength and are limited by the waveguide cutoff condition because $m \geq 1$ for all of the higher order modes.

For the applications of surface waves such as filters, modulators and sensors which will be discussed in the following sections, the excitation of higher order modes become a negative factor that may degrade the strength of resonances for surface modes. The multiple surface wave resonances due to the existence of higher order modes can decentralize the coupling energy into each surface mode and result in weak surface wave resonances. In order to prevent the excitation of higher-order surface waves, the single mode operation is very necessary within a broad frequency region. The single-mode-operation (SMO) should satisfy the condition:

$$\lambda_{SMO} \geq 2W(\varepsilon_1 - \varepsilon_2)^{\frac{1}{2}} \tag{4-3}$$

This equation is derived by finding the cutoff wavelength of the second-order mode with $m = 1$. It is noted that the SMO condition is dominated by the thickness of the membrane and the differences of dielectric constants between the membrane and its environment medium. The fabrications of membrane optoelectronic devices in the THz region are compatible with thin film substrates whose thicknesses range from nanometers to micrometers. As an example, a thin film has a refractive index 1.7 in the THz region. From the Equation (4-3), one can get the SMO condition: $\lambda_{SMO} \geq 2W(\varepsilon_1 - \varepsilon_2)^{\frac{1}{2}} = 2.75 \times W(\mu m)$, which depends on the thickness of the thin film. Supposing a membrane with thickness 20 µm, the single mode operation is $\lambda_{SMO} > 55\mu m$ and the frequency range is $f < 5.45$ THz. As a comparison, a thinner membrane has submicron thickness 0.5 µm, the SMO is $\lambda_{SMO} > 1.375\mu m$ and the frequency range is $f < 218$ THz which is located in the near-inferred region. This simple calculation indicates that a membrane with a moderate thickness can implement the broadband single-mode-operation for surface wave resonances. This information implies that (1) the fabrication of membrane optoelectronic devices based on the surface wave resonances can be relatively easy and low-cost in the THz region, and that (2) the well-performed single-mode-operation surface wave devices can be extended to higher frequency regions range from THz to near-infrared spectrum.

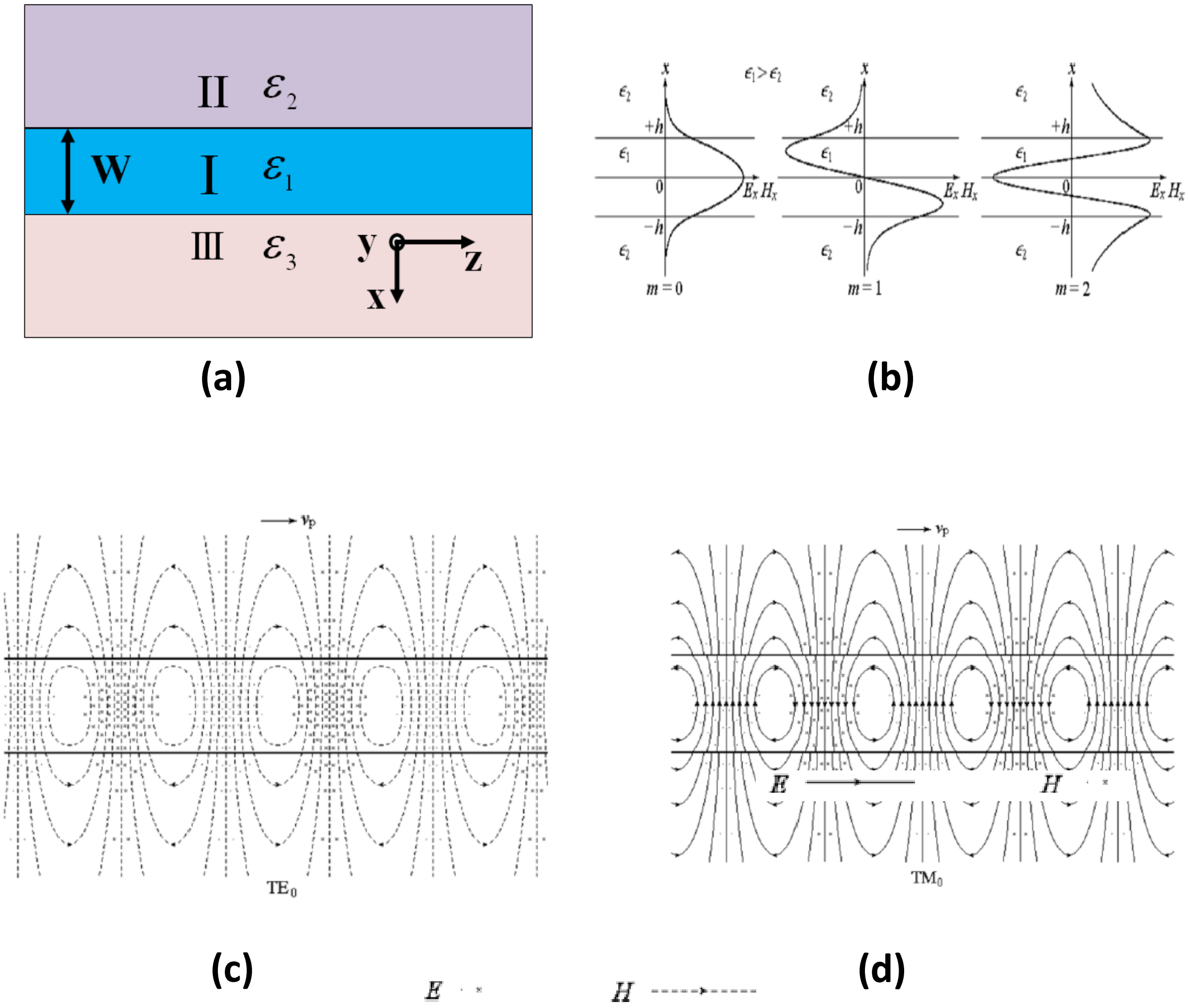

Figures 4-1 (a) Schematic of the slab waveguide consists of claddings and a dielectric core formed by a membrane. The dielectric constant of membrane is ε_1 , the dielectric claddings are in region II and III which are above and below the membrane with dielectric constants ε_2 and ε_3 respectively. (b) The transverse field distribution for different modes. (c) The electric and magnetic field distribution of fundamental TE mode. (d) The electric and magnetic field distribution of fundamental TM mode [99].

4.1.2 Surface mode excitation by metamaterial resonators on a membrane

Planar microstructures such as split-ring resonators (SRRs) could be fabricated on membranes. Each resonator acts as a small dipole antenna, first coupling with the incident radiation and then reradiating electromagnetic waves to the free space. There are two types of dipole antennas distinguished by their oscillation patterns, as shown in Figure 4-2(a). One is the electric dipole, characterized by a separation of positive and negative charges. The other one is the magnetic dipole, induced by a closed circulation of electric current. As an example shown in Figure 4-2(b), a square array of split rings resonators (SRRs) made from t= 300 nm of Aluminum is fabricated on a Mylar membrane of W=22 μm thickness, where a= 80 μm, b=80 μm, h= 22 μm, g=6 μm, periodicity P=250 μm. The electric and magnetic dipole oscillations can be induced under different incident polarization states. The periodic array of such electric or magnetic dipoles can transfer the lattice momentum from the indecent light to surface modes (SW), thus satisfying the surface wave resonance condition through the momentum matching expressed by the following equation:

$$K_{SW} = k_x \pm nG_x \pm mG_y \tag{4-4}$$

Where K_{SW} is the wavevector of surface mode, $k_x = (\omega/c)\sin\theta$ is the components in the (x-y) plane of antenna array, and $G_x = G_y = 2\pi/p$ are lattice momentums offered by the diffraction of the antenna arrays. It should be noted that due to the array of SRR antennas in the membrane, SW cannot be permanently sustained on the membrane because SRRs act as radiators, and thus will radiate into free space. In order to study the surface waves excitation with respect to the incident polarizations, we measured the angular dependent transmission for different polarization states. The TE and TM rotation modes with respect to the incident polarizations are shown in the inset of Figure 4-2(b).

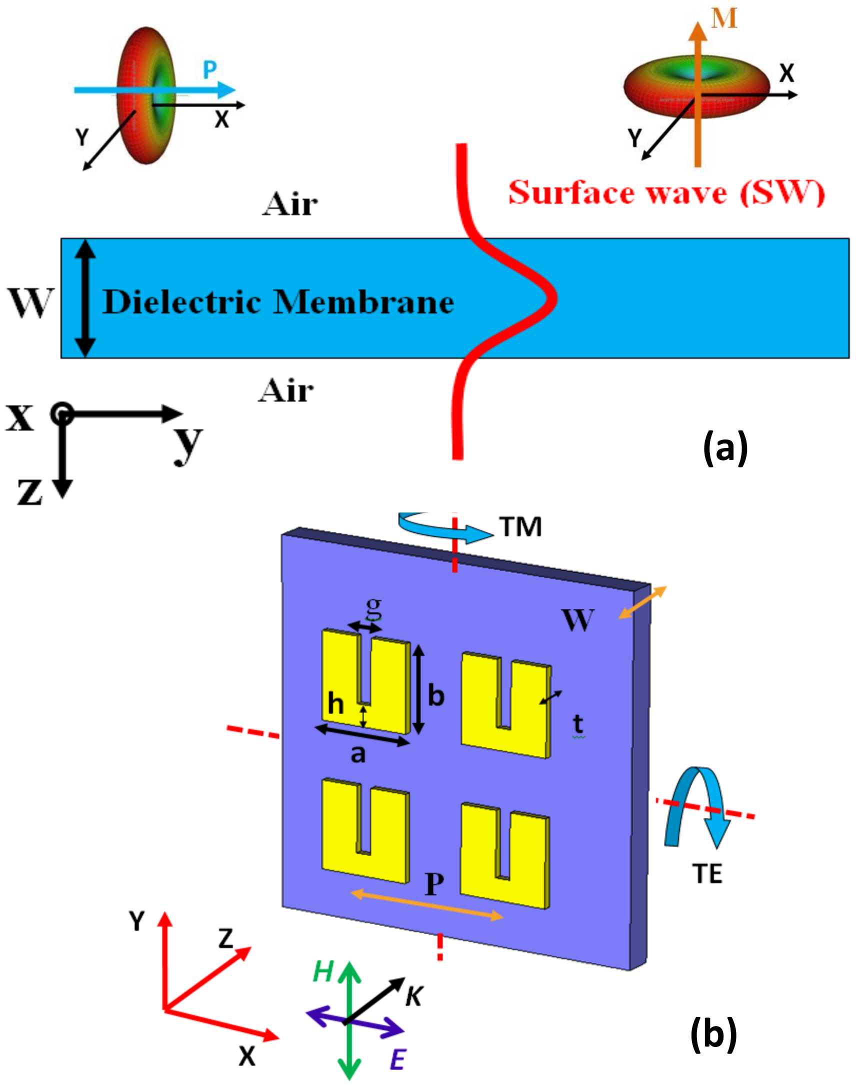

Figure 4-2 (a) Electric dipole (left) and magnetic dipole (right) coupled with surface mode sustained by a membrane. (b) Square array of split rings resonators (SRRs) with respect to the rotation modes under different polarization states.

4.1.3 The role of electric and magnetic dipoles for the excitation of surface modes

We conducted experiments to study the effects of electric and magnetic dipoles for the excitation of surface modes. In order to induce the electric and magnetic dipole independently, the SRRs are illuminated under different polarization conditions as depicted in Figure 4-3, classified as (A), (B), (C) and (D), respectively. The corresponding transmission spectra are shown in Figures 4-4 (a) and (b). We used angular transmission spectrum measurement to map the dispersion curves for TE and TM modes under different polarization conditions. In the dispersion diagrams shown in Figure 4-5, the flat black curves have very small dispersions, thus being recognized as localized modes. The red curves shown in these diagrams are associated with SW modes, which usually have very dispersive nature. As shown in Figures 4-5(a) and (b), we can see that for the type A and B associated with the excitation of magnetic dipole, both of the resonant SW modes shift to the lower frequency region, indicating an isotropic excitations of SW modes. However, as a comparison shown in Figures 4-5(c) and (d), the excitations of electric dipoles corresponding to type C and D, present an anisotropic effect for the SW excitations. It is evident that for TE mode the surface wave resonances will redshift because of the momentum transfer under the TE rotation. However, we can see that the SW dispersion of TM mode is almost flat, indicating no momentum transfer under the TM rotation. Intuitive physical pictures shown in Figure 4-6 could reveal the underlying physics associated with these observed phenomena. As shown in Figure 4-6(a), for the situations of type C and D, the incident polarized light (along x) induces electric dipoles parallel to the x direction. From the radiation patterns for the x oriented electric dipoles, the radiations mainly generate along y direction, resulting a uniaxial SW excitation due to the momentum transfer only along a single axis. As a comparison shown in Figure 4-6(b), the incident polarized light induces magnetic dipoles perpendicular to the x-y plane, and the radiation pattern of the perpendicular magnetic dipole is omnidirectional, thus leading to SW excitations along both axes, i.e. biaxial SW excitation, where the incident polarized light can transfer its momentum to SW propagation along both x and y axes.

(a) Magnetic dipole oscillation

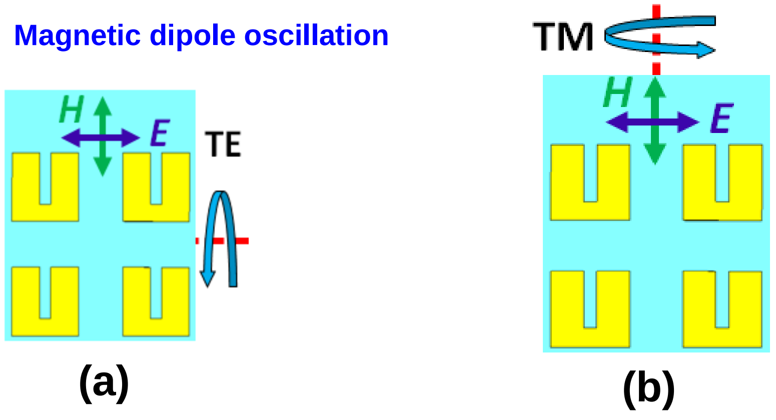

(b) Electric dipole oscillation

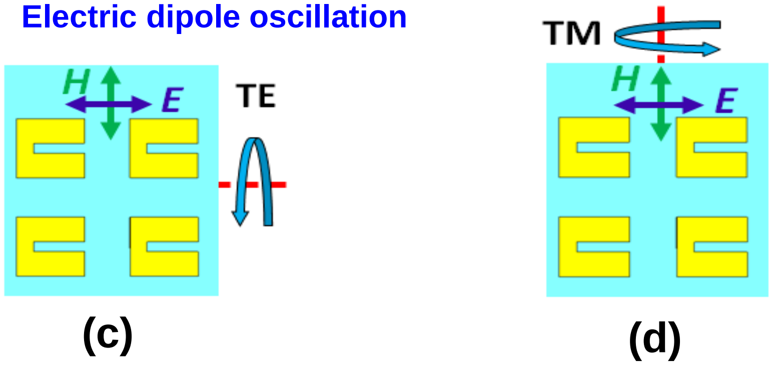

Figure 4-3 (a) Magnetic dipoles excited by different rotation modes with respect to the incident polarized light. Type A and type B corresponding to TE and TM rotation modes, respectively. (b) Electric dipole with respect to different rotation mode. Type C and D are related to TE and TM rotation modes, respectively.

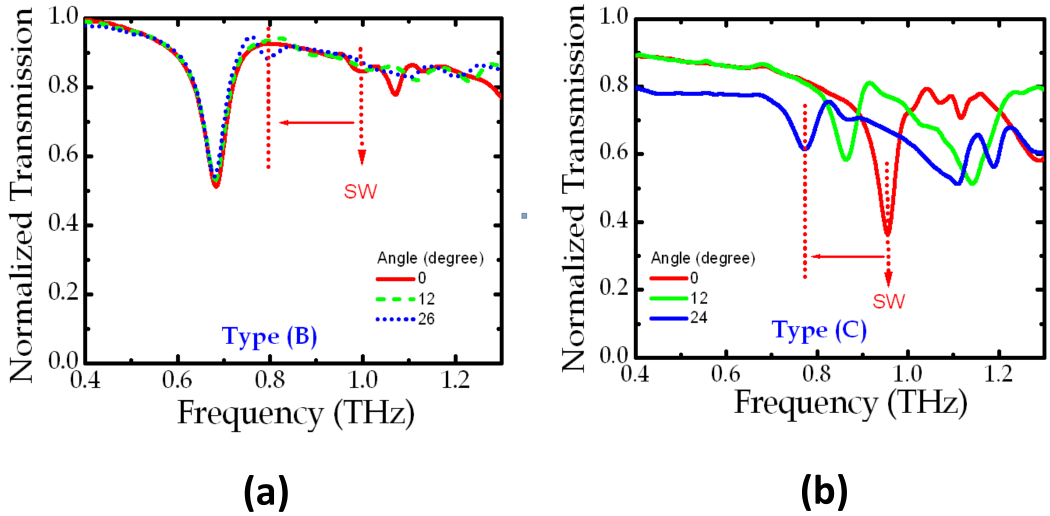

(a) (b)

Figure 4-4 (a) The angular transmission spectrum of type B. (b) The angular transmission spectrum of type C. The "SW" indicates the surface mode resonance.

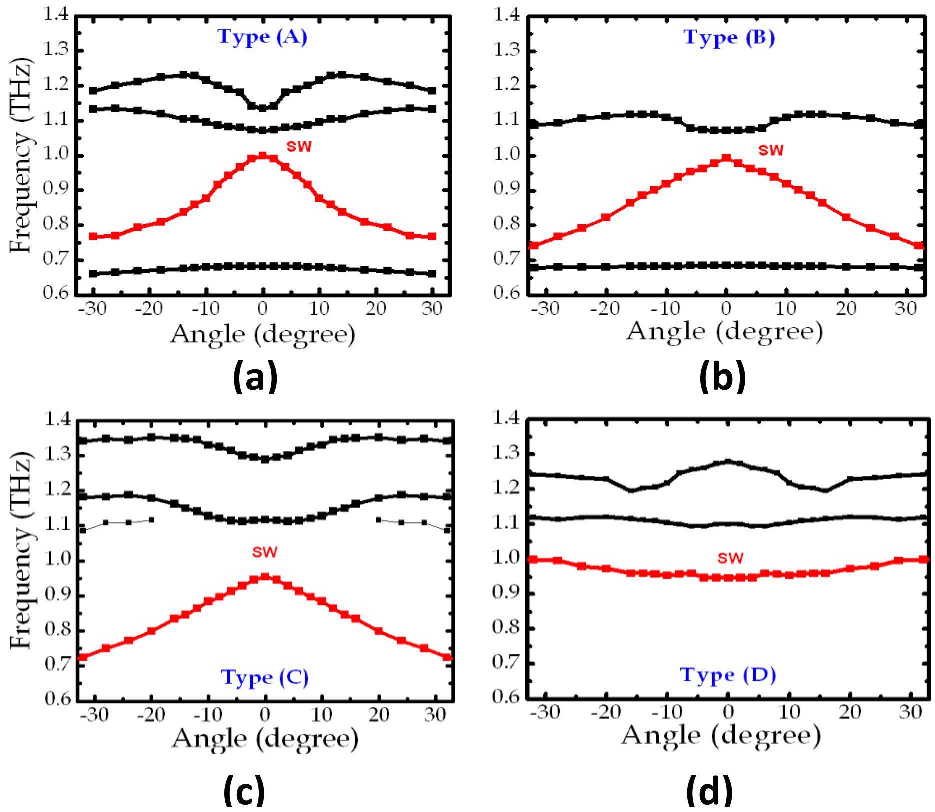

(a) (b) (c) (d)

Figure 4-5 Dispersion diagrams corresponding to type A, B, C, and D. (a) The dispersion curves of type A. (b) The dispersion curves of type B. (c) The dispersion curves of type C. (d) The dispersion curves of type D. The red curves indicate surface modes, and the black curves are associated with localized modes.

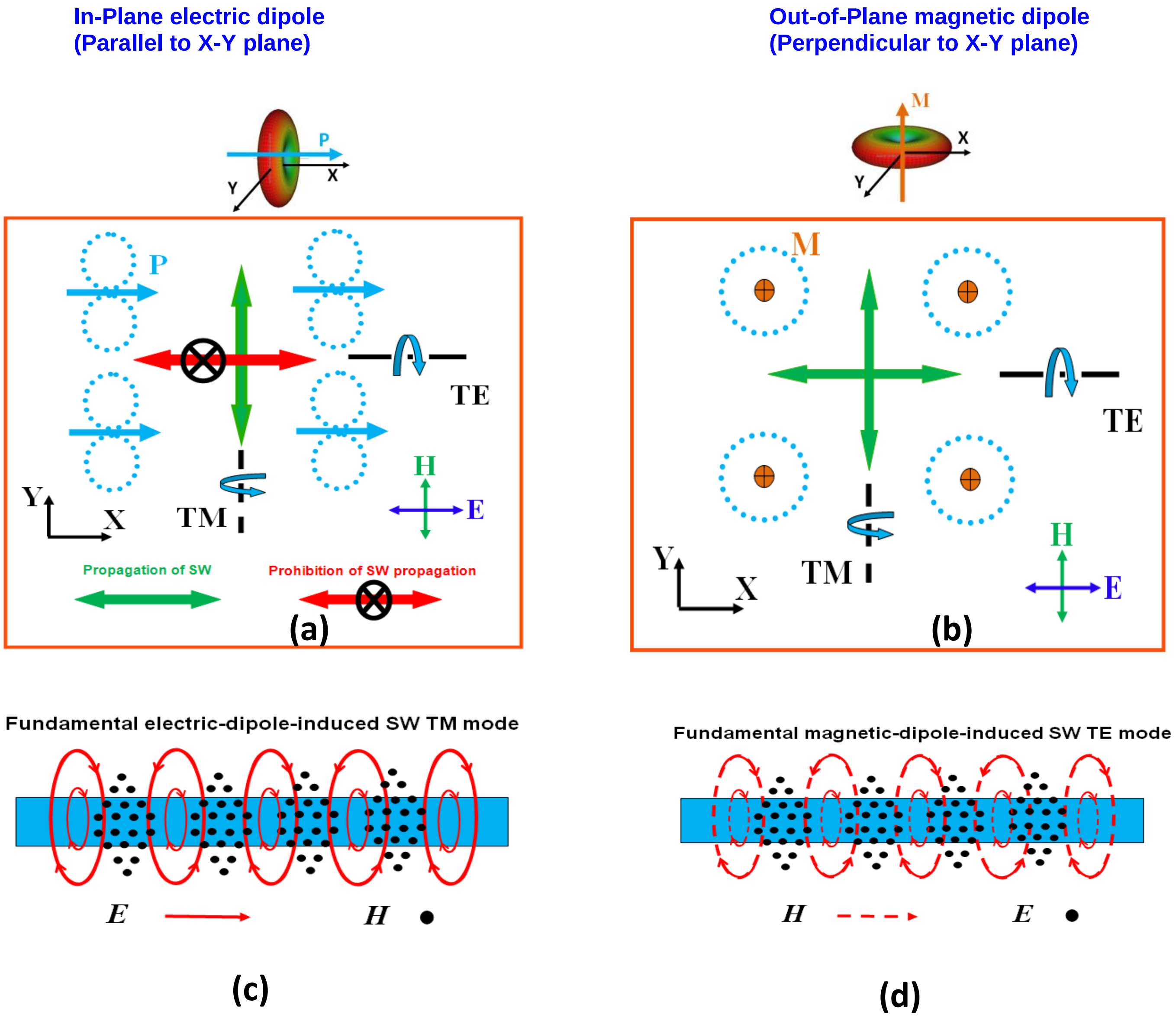

Figure 4-6 (a) The uniaxial SW excitation determined by the radiation pattern of in-plane electric dipoles. (b) The biaxial SW excitation determined by the radiation pattern of out-of-plane magnetic dipoles. (c) The transverse magnetic (TM) mode of in-plane electric dipole induced SW. (d) The transverse electric (TE) mode of out-of-plane magnetic dipole induced SW.

By comparing the effects of electric and magnetic dipole induced SW modes, we can make the following conclusions: (1) The electric dipole sustains uniaxial SW excitation; (2) It supports strong SW resonance, thus being a good SW coupler; (3) From the radiation pattern, the electric dipole induced SW is a transvers magnetic modes, shown in Figure 4-6(c); (4) The magnetic dipole can support biaxial SW excitations; (5) It is relatively incapable to strongly excite SW modes, thus being recognized as a poor SW coupler; (6) The electric dipole induced SW is a transverse electric (TE) mode, deduced from the radiation pattern shown in Figure 4-6(d).

4.2 Surface-wave mediated broadband filters on membrane metamaterials

It has been demonstrated that electric dipoles can strongly couple with surface waves sustained by membrane metamaterials. As a potential application, we experimentally demonstrate a broadband-tunable filter that can be implemented by plasmonic electric dipole arrays. A variety of two-dimensional arrays of rectangular plasmonic antennas fabricated on thin-film substrates are prepared and characterized by the THz time domain spectroscopy (THz-TDS). The zero-order transmission spectra are measured for the analysis of surface mode resonances in the membrane based plasmonic antennas. As shown in Figure 4-7(a), a square array of plasmonic antennas with a periodicity p is fabricated on a thin-film substrate, the unite cell is a rectangular plasmonic antenna with dimensions $a \times b$, and the thickness of the thin-film is W. The fabrication method is the same as the membrane-based resonators mentioned in Chapter II.

As an example, an array of plasmonic antennas with $a = 80$ μm, $b = 100$ μm and $p = 240$ μm is fabricated on thin Mylar films with a thickness 22 μm. The antennas are made of Aluminum (Al) film with a thickness 150 nm. The total size of the sample is $10 \times 10\ mm^2$ and is positioned at THz beam waist. The incident THz beam is polarized along the Y direction parallelling to the surface of the membrane. As depicted in Figure 4-7(b), the membrane plane can rotate around X and Y axis corresponding to the excitation of TM and TE modes, respectively. The transmission spectrum in the frequency domain can be extracted from the Fourier-transformed amplitude of the THz pulses measured in the time domain and defined as $\left|T(\omega)\right| = \left|E_s(\omega)/E_{ns}(\omega)\right|$, where $E_s(\omega)$ is the amplitude spectrum of plasmonic antenna samples, and $E_{ns}(\omega)$ is the amplitude spectrum of an empty holder without loading the samples.

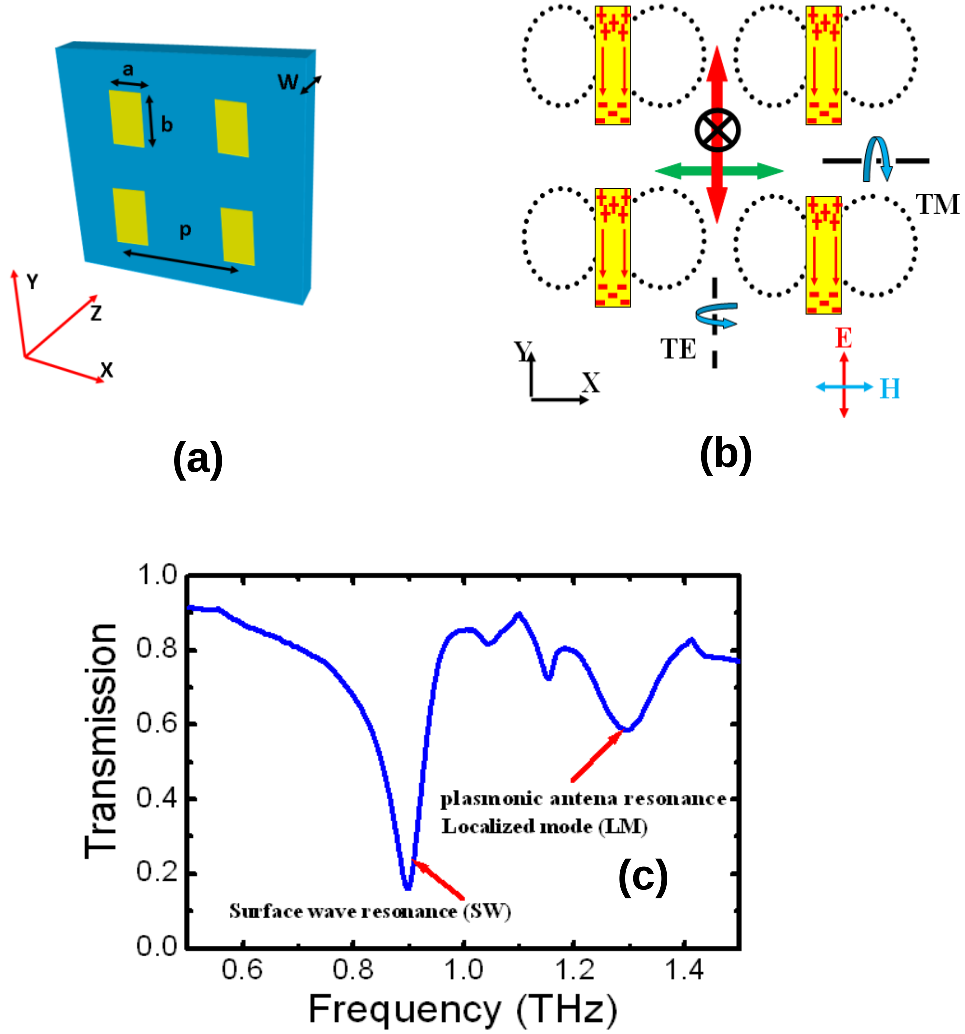

Figure 4-7 (a) A square array of plasmonic antennas fabricated on thin-film substrates. (b) Two types of rotations corresponding to TE and TM rotation modes of the membrane-based plasmonic antennas. The green arrow shows the propagation of surface wave along X direction, the red arrow with a cross indicates the prohibition of surface modes. (c) Surface wave resonance and localized plasmonic resonance.

The responses of the sample by zero-order transmission measurement are shown in Figure 4-7(c). The spectrum indicates several distinct features. For normal incidence, there are two resonant dips in the transmission spectrum. One locates at 0.91 THz with a narrow and strong resonance. The other one is at 1.28 THz which is a relatively weak resonance with broad bandwidth. It is found that the localized plasmonic resonance as well as the collective surface wave resonance can be excited in the membrane, and that the properties of these two resonances are significantly different. In order to make a distinction between these two types of resonances, finite-element numerical simulations are carried out to show the electric and magnetic field distribution of these two resonances and to elucidate the observed phenomenon in the transmission spectra. The periodic boundary conditions are applied to a unit cell, and the normally incident plane wave with a broad frequency band (0 to 3 THz) is applied to excite the resonant modes. The thin Mylar substrate and Al film are modeled with a permittivity of $\varepsilon_M = 2.9 + 0.9i$ and a conductivity $\sigma_{Al} = 3.7 \times 10^7 S.m^{-1}$, respectively. Figures 4-8(a) and (b) show the electric and magnetic field distribution for the resonance at 0.91 THz. It is shown that the magnetic field has only one component in Y direction, and the antenna array is strongly coupled by the electric fields. The patterns of electric and magnetic fields indicate that this resonance is due to the strongly coupled antennas which lead to a surface collective mode with transverse magnetic (TM) polarization. As a comparison, the resonant dip located at 1.28 THz associates with strong electric fields localized at individual antenna. The coupling fields among neighboring antennas are weak, as depicted in Figures 4-8(c) and (d). This localized mode is due to the electric dipole resonance of plasmonic antennas.

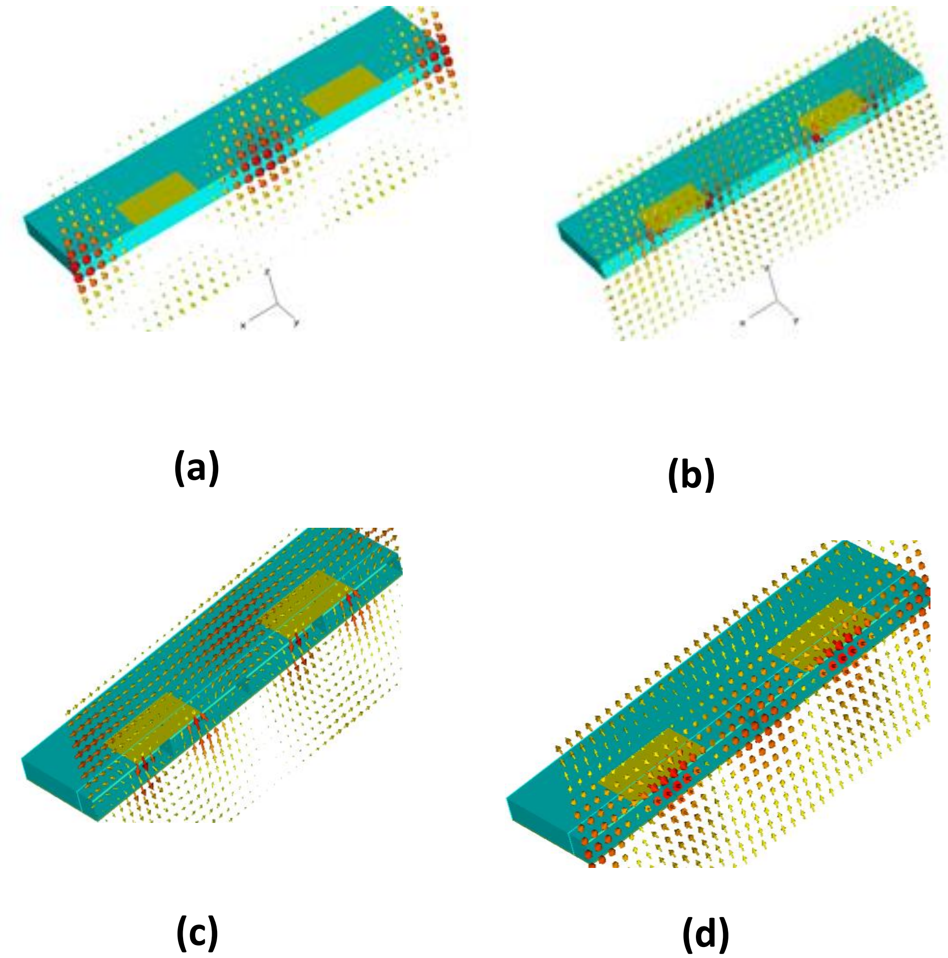

Figure 4-8 (a) and (b) are the electric and magnetic field distributions at 0.91 THz, respectively. (c) and (d) are the electric and magnetic field distributions at 1.28 THz, respectively.

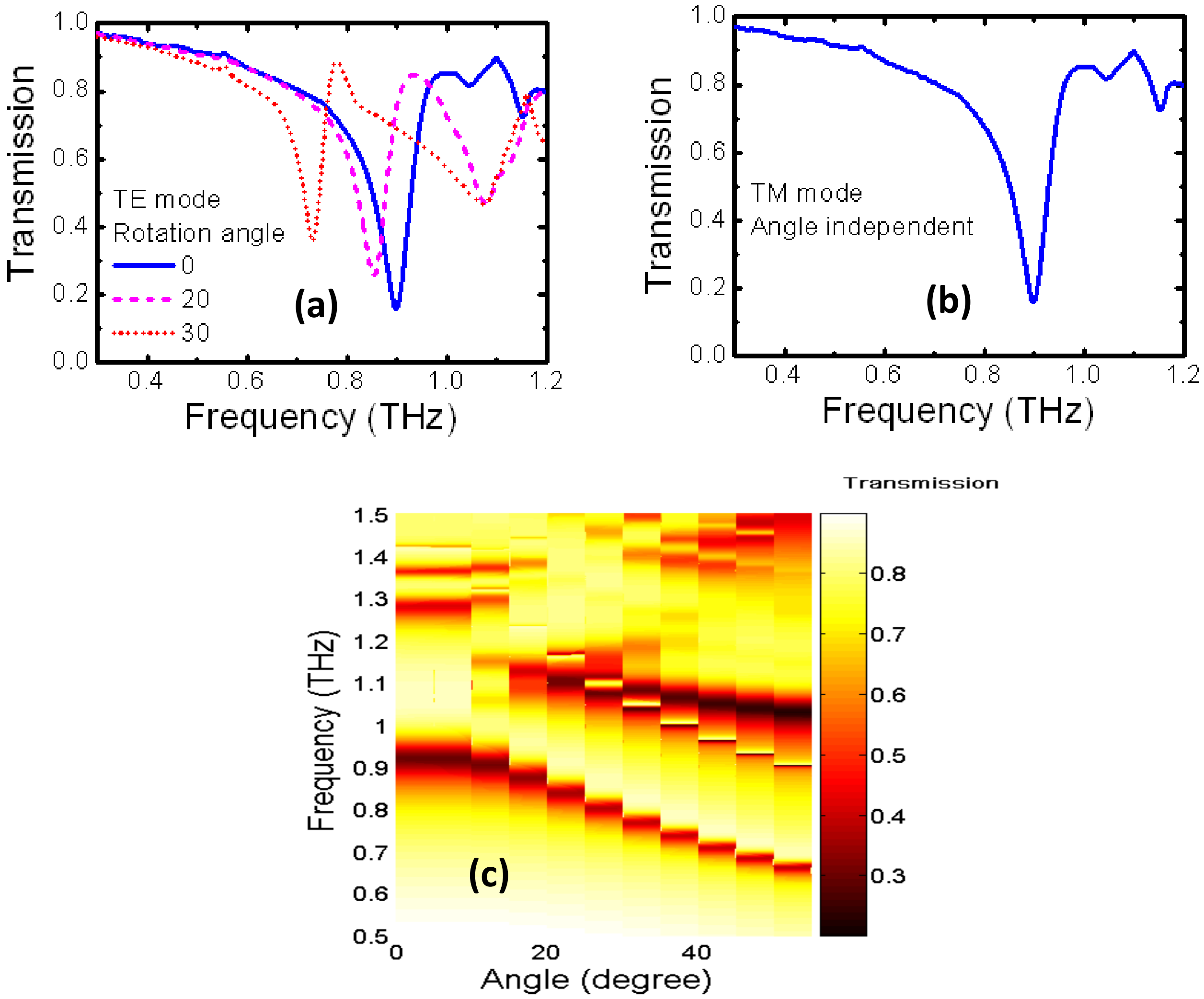

Figure 4-9 (a) The transmission spectrum of TE mode, the rotation of the plasmonic antenna array is around Y axis. (b) The transmission spectrum of TM mode, the rotation of the plasmonic antenna array is around X axis. The response of TM mode is angular independent. (c) Dispersion relation of the membrane based plasmonic antennas.

We have conducted the angular transmission experiment to examine the transmission response with respect to angular change. As shown in Figure 4-9(a)**,** the original surface mode resonance at 0.91 THz red shift by rotating the array plane around Y axis, and the tuning of the resonance is very sensitive to the angular variation. However, the localized dipole resonance of the plasmonic antenna is relatively inactive to the angular change. For TM rotation mode shown in Figure 4-9(b), the rotation of the plane is around X axis and the response is angular independent due to the propagation direction of the surface modes perpendicular to the rotation plane. We will explain the details in the following paragraphs.

There are two important clues relating the above phenomena with the excitation of fundamental surface mode propagating in the membranes. The first one is the absence of strong surface mode resonances for plasmonic antenna array fabricated on bulk substrates. As we discussed in the beginning of section 4.1, the bulk substrate may support multiple guided modes that can decentralize the input energy coupling into the resonances of surface modes. Although multiple guided modes may be exited in the substrate, the strength of these resonances are very weak and cannot be observed in the experiment. Another clue is the strong angular dependence of the transmission spectrum for the membrane based plasmonic antenna arrays. As shown in Figure 4-9 (c), the resonant dip around 0.9 THz shifts significantly for changing angles. From the dispersion relation plotted in Figure 4-9(c), it is found that the angular sensitive resonances have no splitting or degeneracy and thus keep a single mode operation in a broadband region ranging from 0.6 to 0.9 THz. This phenomenon exactly demonstrates that the incident light couples with the fundamental surface modes. The surface modes are propagating waves bounded on the surface of membranes and can be excited by matching the momentums by the incident waves. Due to the momentum matching, the surface mode resonances can be expressed as the following equation:

$$K_{SW} = k_x \pm nG_x \pm mG_y \tag{4-5}$$

where K_{SW} is the wavevector of surface mode, $k_x = (\omega/c)\sin\theta$ is the components in the plane of antenna array. $G_x = G_y = 2\pi/p$ are lattice momentums offered by the diffraction of the antenna arrays.

The dipole oscillations of the plasmonic antennas play an essential role on the excitation and propagation direction of surface modes. As shown in Figure 4-7(b), the external electric fields along Y direction will drive the electrons oscillating on the surfaces of antennas and reradiate electromagnetic waves. The radiation pattern of a dipole indicates that surface waves can't be excited along Y direction due to the minimum radiative fields along the Y axis. The orientation of the maximum field radiation is along the X axis and determines the propagation direction of surface modes.

It is worth to note that the angular dependent resonances of surface modes on the plasmonic antenna array are sensitive to polarization and the propagation axis of surface modes. For electric fields parallel to the Y axis, if the propagation axis X of surface modes parallels to the rotation plane X-Y, the rotation of the array can tune the surface mode resonances by offering additional momentum matched with surface waves. However, for the case of surface mode propagation axis X perpendicular to the rotation plane Y-Z, the rotation of the antenna array has no effect on the resonance tuning for surface modes because there is no additional momentum offered by the rotation of antenna arrays. By considering the polarization and propagation direction of surface modes, the surface mode resonances equation can be modified as follows:

$$\text{For } E \,//\, Y\text{ ; } \quad K_{SW} = k_x - nG_x \tag{4-6}$$

$$\text{For } E \,//\, X\text{ ; } \quad K_{SW} = k_y - mG_y \tag{4-7}$$

Moreover, several factors including the filling factor of plasmonic antennas and intrinsic dielectric loss of membrane can significantly influence the strength of surface mode resonance. First, the excitation of surface modes depends on the electric dipole oscillations of the plasmonic antennas and the density of electric dipoles can influence the strength of surface mode resonance. As shown in Figure 4-10(a), the filling factor of plasmonic antennas is defined as $F = \frac{a \times b}{p^2}$, and the shapes of the rectangular antennas is conserved by a constant ratio between the length a and width b of the antenna. We keep the periodicity $p = 240\mu m$ a constant, and scale the antenna size by changing $b = 60$ to $140\mu m$ with a constant ratio. The resonant frequencies of surface mode and localized antenna resonance both produce red shift due to the increased size of antennas. It is clear that a small filling factor of antenna leads to the diluted electric dipole oscillations and degrades the strength of surface mode resonance. It is expected that larger filling factors will increase the density of electric dipole oscillations and enhance the resonant strength of surface modes. However, a remarkable feature is that the bandwidth of the surface resonance gradually become broad with the enlargement of antenna size, and this resonance broadening may be due to the increased mutual coupling among electric dipoles. The other key factor is the dielectric loss of the membrane. It is assumed that the real part of dielectric constant for the Mylar thin film is $\mathrm{Re}(\varepsilon_M) = 2.9$. The imaginary part of ε_M associated with the degree of the dielectric loss can be described by the parameter loss-tangent $\delta = \mathrm{Im}(\varepsilon_M)/\mathrm{Re}(\varepsilon_M)$. As depicted in Figure 4-10(b), the excitation strength of surface mode and localized antenna resonances seriously degrade with the increasing of the dielectric loss of thin film substrates. Other factors such as the periodicity of antenna array, various shapes of antennas, the thickness of the membranes, and the types of metals may all have influence on the resonance of surface modes. It is beyond the scope of this report to describe the details of all these works.

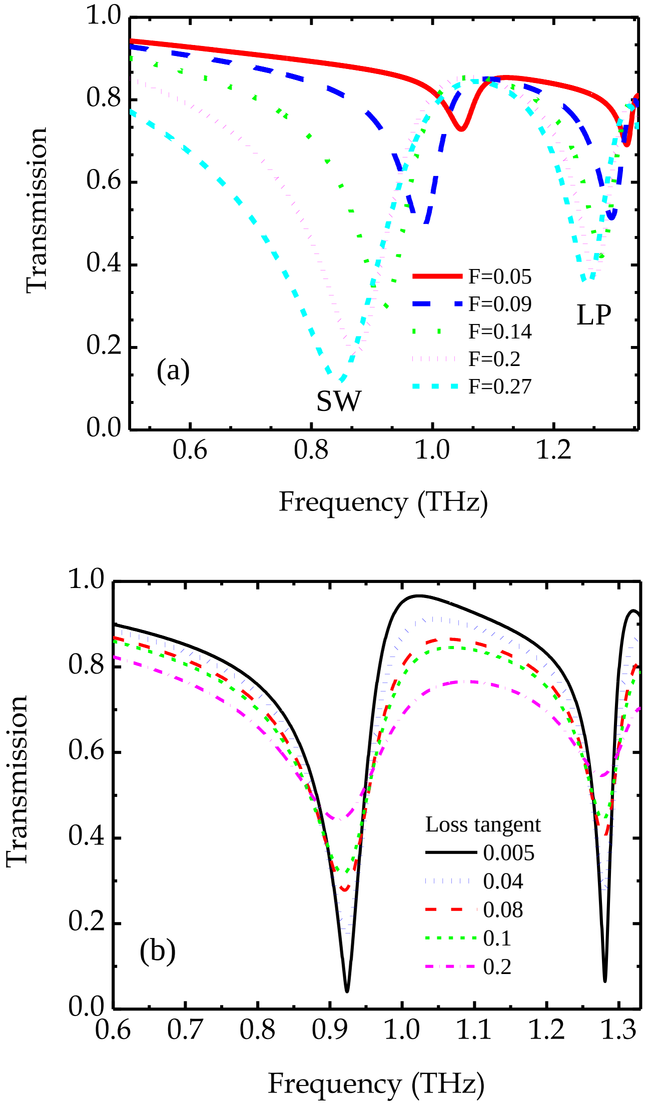

Figure 4-10 (a) The influence of antenna filling factor on the resonant strength of surface modes and localized plasmonic antenna resonance. (b) The dielectric loss dependent resonances of surface modes and localized plasmonic antenna mode.

4.3 Angular sensitive THz amplitude and phase modulation based on surface waves

With the development of THz technology, novel functional devices including sensors, filters, switches, and modulators are very necessary for THz sensing and communication. The ability for tuning the response of functional devices in THz region is very useful to implement the active control for the THz radiation. Recently reported active THz devices have demonstrated the possibility to implement the amplitude and phase modulation by using plasmonic and metamaterial devices. Chen *et al.* achieved amplitude and phase control over THz radiation on the active meta-surfaces driven by the external voltage [37]. The electrically controlled active meta-surfaces can tune the response by changing the conductive loss of split ring resonators (SRRs). Besides the electrical control, the opto-excitation of semiconductors combined with THz functional elements offers other possibilities for the active devices. Chen *et al.* demonstrated the ability to implement redshift tunability through the photoconductive increase in the capacitance of the metamaterial resonators [38]. Shen et al. experimentally achieved broadband buleshift tunability by changing the inductance of SRRs resonators with photoexcitation [100].

In this section, we show that surface wave resonances in plasmonic or metamaterial surfaces can implement amplitude and phase modulation for THz radiation. Instead of aforementioned method for tuning capacitive or inductive response of local resonators, the surface wave modulator actively controls the surface mode resonances by changing the coupling momentum of incident THz beam. For example, in section 4.3, it is demonstrated that a membrane-based plasmonic antenna array can achieve very strong surface mode resonance. From the dispersion of surface modes shown in Figure 4-11(a), there is a flat region (green dashed line) ranging from 0 to 15 degrees where the surface mode resonances is insensitive to the rotation of the sample due to the excitation of band-edge modes. However, beyond the flat region ranging from 20 to 50 degrees, the surface mode resonances become significantly sensitive to the angular change. The modulation of amplitude and phase for THz radiation is implemented within the angular sensitive region called “surface wave modulation region” marked by a dashed blue line in Figure 4-11(a). The detailed broadband transmission responses are shown in Figure 4-11(b). It is worth to note that the surface mode excitation is associated with a narrow resonant dip in the transmission spectrum. The resonances of surface mode can be tuned within a broadband range from 0.65 THz to 0.85 THz by changing the angle from 15 degrees to 60 degrees. Although the tuning is implemented in a broadband frequency region, the strength and line-shapes of surface mode resonances are almost unaltered. This property ensures a linear response for both the amplitude and phase modulation.

Another property is that the surface mode resonance is very sensitive to the angle variation since a small angular rotation of the sample will make a significant shift of the resonances. From the standpoint of the THz modulators based on the resonance-shift tuning, it is crucial to evaluate the potential for the amplitude and phase modulations. The evaluation can be implemented by checking the “complete tuning” as shown in Figure 4-12, where the maximum variation of amplitude and phase can be achieved. For example, as shown in Figure 4-13, the plasmonic array is first tilted by 25 degrees off the propagation axis of incident THz beam. The initial tilt angle makes the surface mode resonances fall into the angular sensitive region where the amplitude and phase modulation are implanted by rotating the sample with small angles. It is shown that a complete-tuning can be achieved through rotations angles less than 5 degrees. The figure of “complete tuning” shown in Figure 4-13(a) indicates that the maximum amplitude modulation can be implemented by tuning the surface mode resonances “on/off” for THz radiation at 0.77 THz. About 50% amplitude maximum modification can be achieved by a 5 degrees rotation angle. The complete-tuning for phase modulation, however, does not occur at the resonance region of 0.77 THz, and is a little off-resonance locating at 0.75 THz. Figure 4-14(a) shows that the amplitude modification is approximately linear function with the rotation angle and very sensitive to the angular variation. Figures 4-14(b) and (c) demonstrates the ability for the phase modulation. A phase shift of 0.8 rad under a 5 degrees rotation can be achieved with a transmission fluctuation less than 10%. The above amplitude and phase modulation based on the surface mode excitation can be implemented within a very broadband ranging from 0.65 to 0.85 THz. The tunability for broadband blueshift and redshift is very challenging by using the electrical control and photoconductive excitation methods. As a comparison, the realization of broadband buleshift / redshift switch by using surface mode resonance is quite simple as shown in Figure 4-14(d), because one just needs to choose an initial angle of the sample and tune the resonance at will by changing the rotation angles. The fabrication of membrane-based resonators such as plasmonic array or metamaterials working in the THz region is very compatible with current microfabrication method. The strong resonances with high angular sensitivity may combine MEMs technique to implement the high speed MEMs modulators or switches, active filter, and spatial light modulators function at THz region.

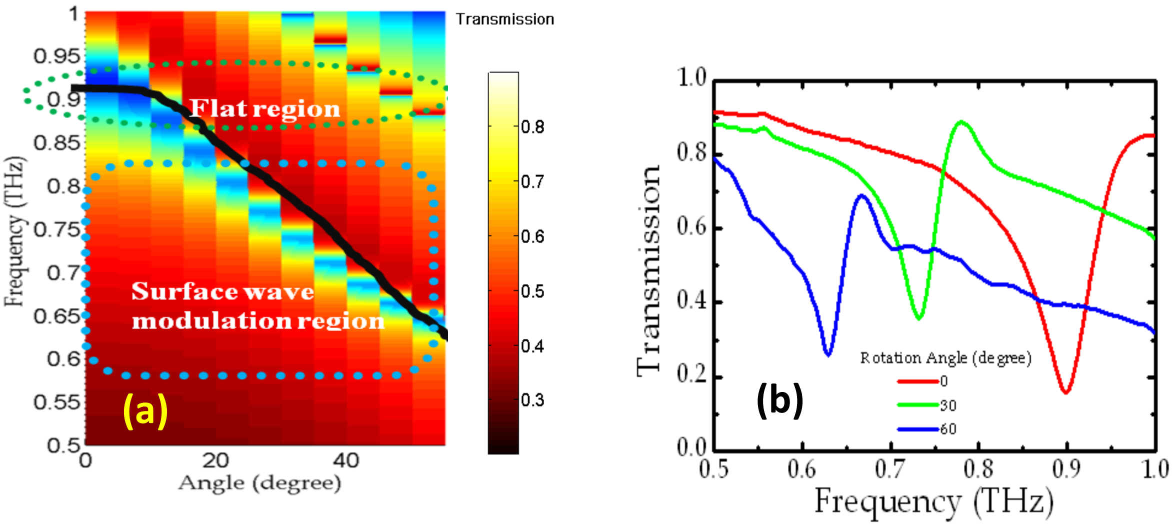

Figure 4-11 (a) The dispersion of the fundamental surface mode. The bold black line represents the dispersion curve of surface mode. The flat region and surface wave modulation region are marked by green and blue dashed lines, respectively. (b) The zero order transmission spectrums for the surface modes controlled by the rotation angle.

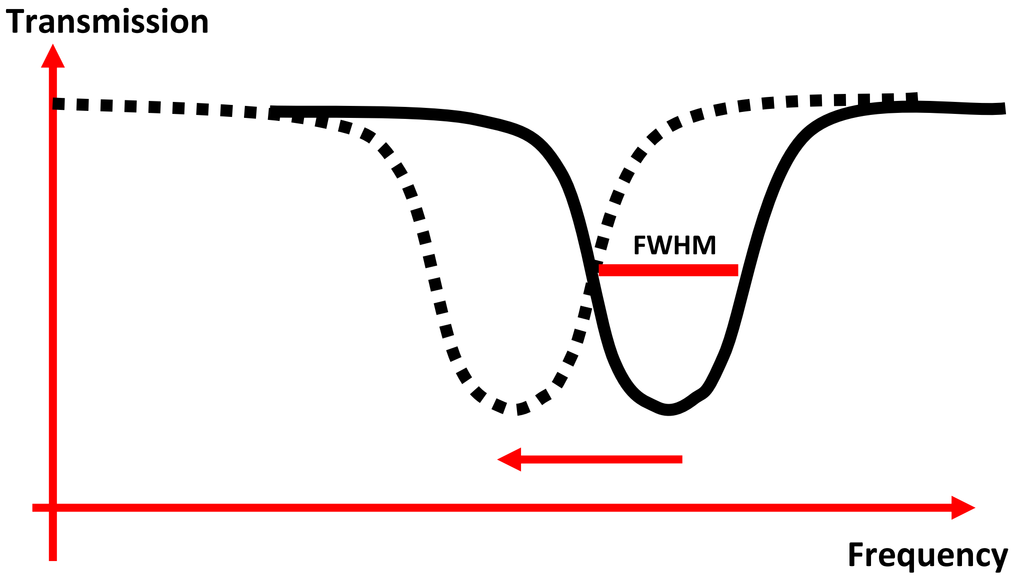

Figure 4-12 The "complete tuning" of modulators based on the resonance-shift tuning. Bold red line represents the full-width-a- half –maximum (FWHM) for the resonances.

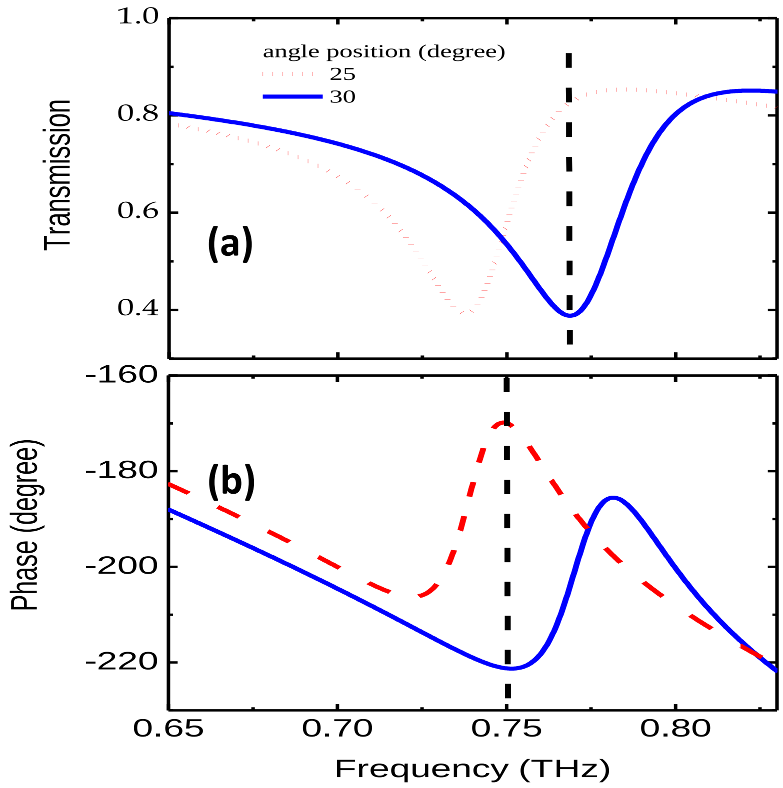

Figure 4-13 The “complete tuning” associated with angle positions of the plasmonic arrays. The “complete tuning” for amplitude modulation (a), and phase modulation (b). Black dashed lines related to the amplitude or phase modulations at specific frequencies

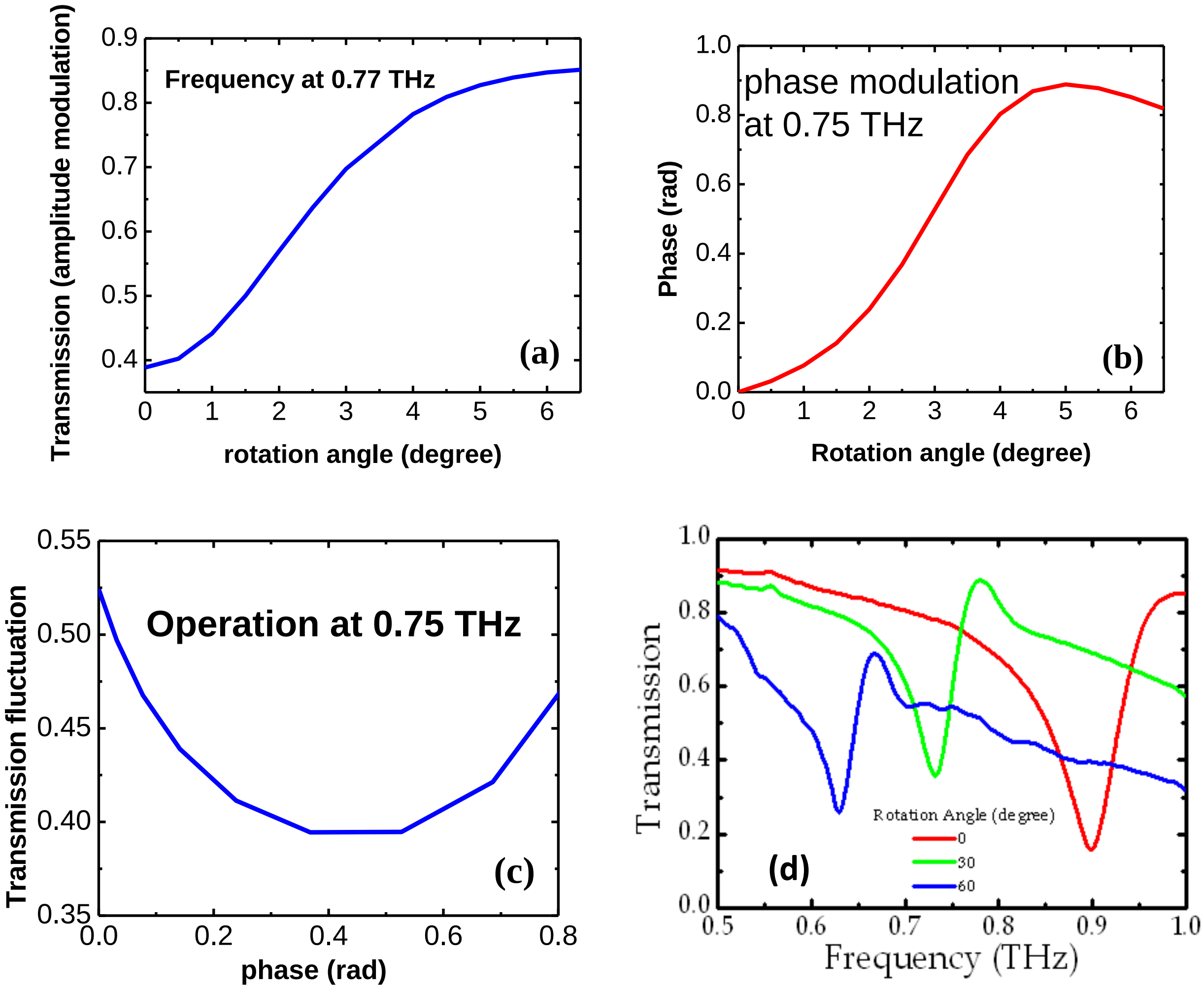

Figure 4-14 (a) The amplitude modulation by rotation angle. (b) The phase modulation within a small angular range. (c) The transmission fluctuation associated with phase modulation. (d) Broadband red-shift and blue-shift switches based on the surface mode resonances.

4.4 Conclusion

It is demonstrated that both electric dipole and magnetic dipole can excite surface mode resonance on the membrane metamaterials. It is found that electric dipoles can strongly couple with SW modes; however, as a comparison, magnetic dipoles are relatively incapable to excite the surface modes. As potential applications, membrane metamaterials comprised of electric dipole resonators may be used to implement broadband filters. Moreover, benefited from its angular sensitive responses, the membrane meta-surfaces can realize THz switches and phase shifters. The strong resonances with high angular sensitivity could be compatible with MEMs technique to implement the frequency agile modulators or switches mediated by surface modes.

CHAPTER V

MICROFLUIDIC SENSING PLATFORM BASED ON TEXTILE PLASMONIC METAMATEIRALS

In this chapter, with a great interest and merit, we bridge between the electromagnetic textile materials and microfluidic systems functioning in the THz region. This combination may pave a way in developing both functional metamatrials and new THz optofluidic systems, such as fluidic controlled metamaterials. Importantly, a new microfluidic sensing platform is demonstrated, which is benefited from the strong light-fluid interaction in textile metamaterials, showing great potential for cost-effective and high performance sensing platform useful in chemistry, biology and medicine applications.

5.1 Textile materials and microfluidic systems

Textiles are flexible woven materials consisting of a network of natural or artificial fibers. They are now essential in our daily life, and are well-known as long history artificial materials. The fabrication technique of textile materials is “weaving”, in which two distinct sets of threads are interlaced at angles to form a fabric, and the geometries of the material can be engineered. The weaving technique is also an ancient fabrication method, which is now being developed to be an accurate assembling method in cloth fabrications.

Without a doubt, the capability of textiles to strongly interact with electromagnetic (EM) fields will lead to novel electromagnetic artificial materials, and bring new scopes and possibilities in manipulating EM waves. On the other hand, textiles, consisting of periodic networks of microfibers, can transport small volumes of fluid because of the fluidic flow driven by the capillary force of fibers. This capability makes textile materials to be promising microfluidic systems, which have been proven to be particularly beneficial in biomedical and chemical applications.

In this work, we show great interest and merit to bridge between the electromagnetic textile materials and microfluidic systems functioning in the THz region. This combination may pave a way in developing new THz optofluidic systems, such as fluidic tunable metamaterials, and create a new microfluidic sensing platform benefited from the strong light-fluid interactions in textile metamaterials, possessing great potential for cost-effective and high performance sensing, which is extremely desirable in chemistry, food science, medicine, and biology applications.

It is not surprised that the dielectric textiles do not directly strongly interact with the incident THz radiation as they only behave like a thin dielectric layer with respect to the normally incident waves, and no strong electromagnetic response is expected. However, introduction of metallic properties into the textile will make it as a plasmonic material, which supports freely oscillating electrons, and thus could strongly couple with the electromagnetic fields. The electromagnetic properties of these textile materials sensitively depend on their configurations and geometries, making it possible to engineer their electromagnetic response over a broad range of controllable parameters by using weaving technique.

As shown in Figure 5-1, two kinds of textiles associated with different weaving styles (more details seen in the following sections) are measured using THz-TDS method. It is evident that the dielectric textiles show no prominent electromagnetic (EM) response. However, strong well-defined resonance dips appear for both samples after the metallization process. At a first sight, one may think that this phenomenon can be simply explained as the inductive response supported by a metal mesh, which is a well-known resonant filter for the EM waves. However, we will show in the following sections that the fundamental resonance behavior in the textile materials is quite different and distinguishable from that of a metal mesh.

Our next goal is to combine the plasmonic textile materials with microfluidic systems. The textile formed by microfibers can act as a pump-free fluidic guiding system [101], benefited from the capillary force of microfibers driving the fluidic flow along the fibers. As shown in Figures 5-2 (a)-(c), the microfluidic flow in textiles may be implemented in two modes. The first one is freely uniform spreading in the periodic systems, thus named as “freely spreading mode”. The other one is called “directional guiding mode”, which can confine and guide the fluid in well-defined channels. These microfluidic channels may be formed by surface patterned fabrication in textiles. For example, photoresist-soaked textiles with a mask defining the surface patterns can be implemented using the photolithography method. For simplicity, we demonstrate microfluidic controlled EM response within the freely spreading mode. As shown in Figure 5-2(d), the type ***A*** textile made from cotton tread is used to implement the experiment. It is clear that the original resonance before loading the liquids locates at the high frequency region; however, after loading the liquid (10 μL liquid is enough to make a saturated frequency shift), the resonance significantly redshifts, thus demonstrating that the fluid loading can effectively tune the resonance of textile materials. Furthermore, as shown in Figure 5-2(e), a small refractive index change associated with biochemical signals of analytes could be readout by a resonance shift of the textile material. As demonstrated in the experiment, a 0.06 refractive index change induces a 23 GHz shift, corresponding to a high sensitivity $S = \Delta\lambda / \Delta n = 2.18 \times 10^5 \ {}^{nm}\!/_{RIU}$ for THz sensing.

However, the nature of the fundamental resonances and how THz radiation interacts with microfluidic channels are still unclear. The following sections are aimed to explicitly explain the underlying physics.

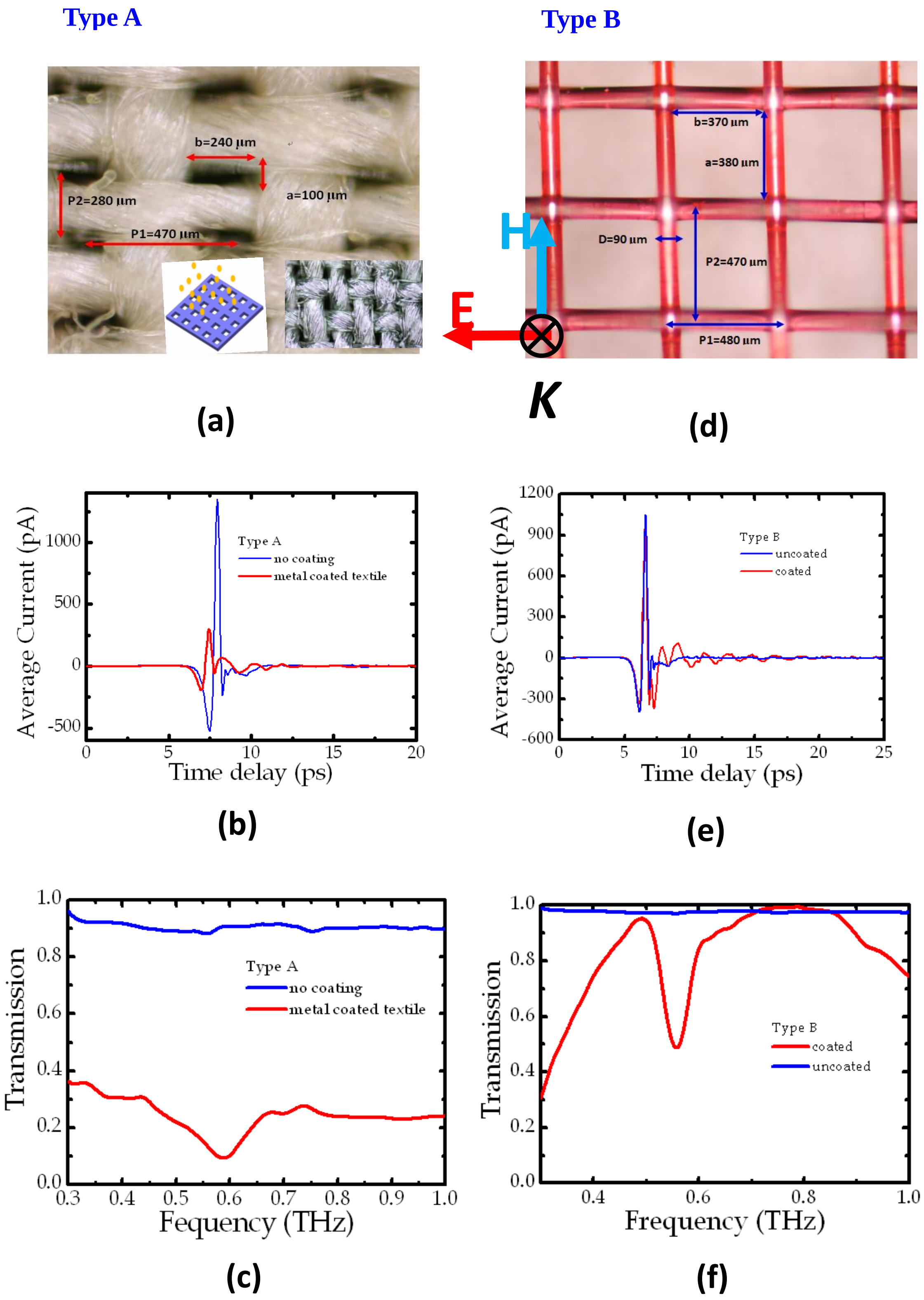
Type A
b=240 μm
a=100 μm
P2=280 μm
P1=470 μm
(a)
Type B
b=370 μm
a=380 μm
D=90 μm
P2=470 μm
P1=480 μm
H
E
K
(d)
Average Current (pA)
1000
500
0
-500
0
5
10
15
20
Time delay (ps)
Type A
no coating
metal coated textile
(b)
Average Current (pA)
1200
900
600
300
0
-300
-600
0
5
10
15
20
25
Time delay (ps)
Type B
uncoated
coated
(e)
Transmission
1.0
0.8
0.6
0.4
0.2
0.0
0.3
0.4
0.5
0.6
0.7
0.8
0.9
1.0
Fequency (THz)
Type A
no coating
metal coated textile
(c)
Transmission
1.0
0.8
0.6
0.4
0.2
0.0
0.4
0.6
0.8
1.0
Frequency (THz)
Type B
coated
uncoated
(f)

Figure 5-1 (a) Type A textile with respect to the incident polarizations. (b) Time domain measurements for type A textile with and without metallization. (c) The corresponding resonance in transmission spectrum. (d) Type B textile. (e) Time domain measurements for type B textile with and without metallization. (f) The corresponding resonance in the transmission spectrum. In the metallization, 500 nm Aluminum (Al) coating is achieved under deposition rate 1~2 nm/s for 30 s, keeping 5 nm/s to the end.

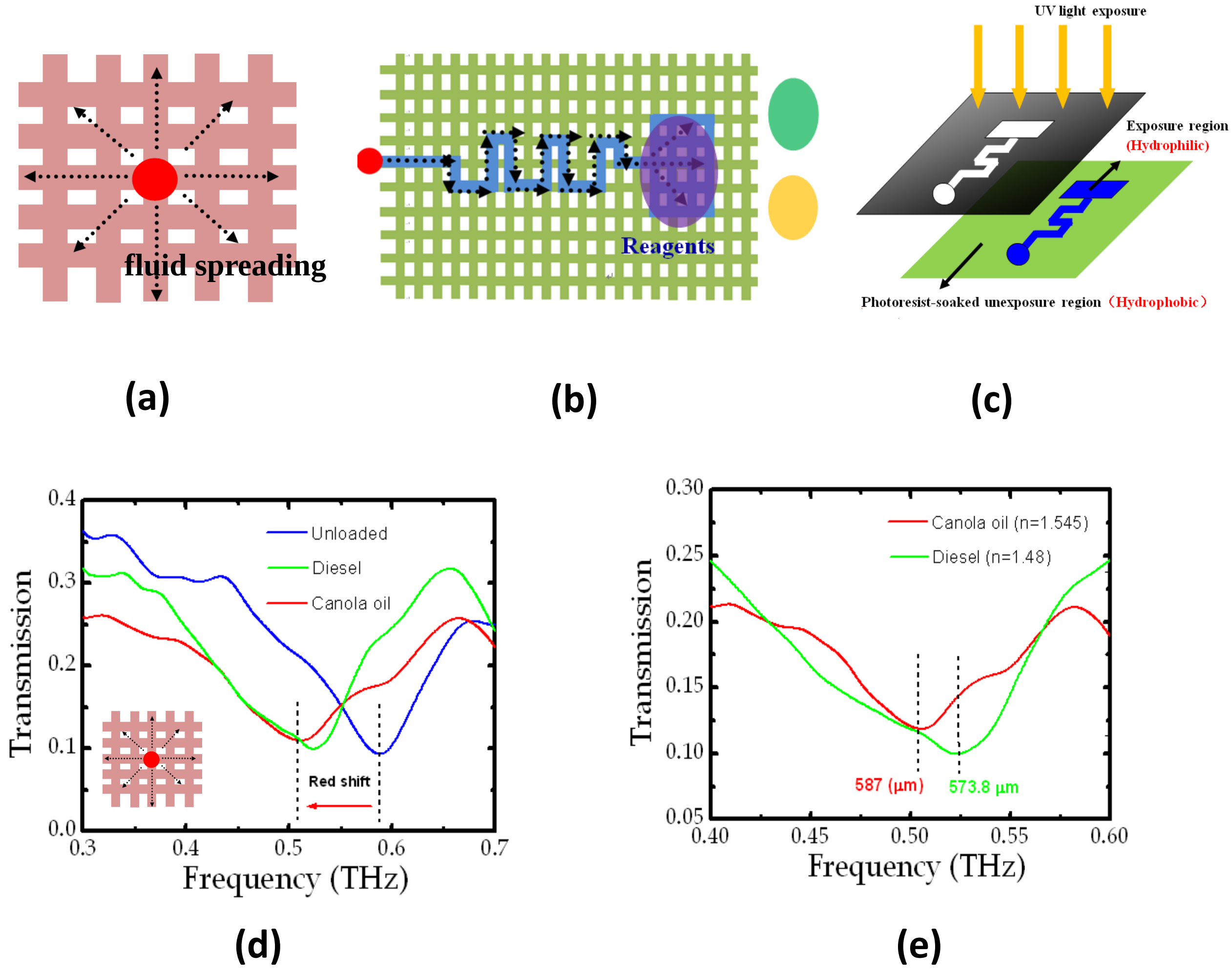

Figure 5-2 Microfluidic system combined with the textile materials. (a) Freely spreading mode in textile. (b) Directional guiding mode by surface patterned textiles. (c) Surface pattern made using photolithography method. (d) Microfluidic controlled resonances. (e) Microfluidic plasmonic label-free sensing based on the textile materials.

5.2 Novel electromagnetic response in textile materials associated with weaving styles

In this section, we introduce novel electromagnetic phenomena related to weaving styles of the textile materials. It is found that isotropic and anisotropic polarization responses appear in different types of textile materials, which could be defined by weaving styles. As shown in Figures 5-3(a)-(c), the resonances of the type-A textile materials present an anisotropic polarization response, where a well-defined dark mode resonance (resonance dip) shows up when being illuminated by a horizontal polarized (H) light. However, no remarkable resonance presents with vertical (V) polarizations. As a comparison shown in Figures 5-3(d)-(f), the type-B textile materials have well-defined dark mode resonances, being remarkable for both H and V polarization conditions.

The observed phenomena are due to the different weaving styles forming different types of textiles with variable electromagnetic responses. We introduce two weaving styles shown in Figure 5-4, based on their general representativeness in weaving technique. The first one is called “Plain Dutch Weave”, where crimped wires along the parallel direction interlace with straight wires along the vertical direction. The other one is “Plain Weave (double crimp weaving)”, in which two crimped wires interlace with each other. From the experiments, it is evident that the polarization responses are relevant to different weaving styles where the wire configurations of the warp and weft play the key roles. In order to explicitly show the effect of wire configuration, we focus on metal wire textiles which have a clear space distribution for warp and weft under the microscope, and support strong and sharp resonances which are very promising in sensing applications.

From the experiment for “Plan Dutch weave” shown in Figure 5-5, the wire has an obvious crimp along the parallel direction, which leads to a strong resonance dip in the transmission spectrum.

Along the vertical direction, the wires are almost straight compared to that of parallel direction, and this configuration leads to a broad passband response, and the sharp and strong resonance that was showing up along the parallel direction disappears. In the experiment of “Plain Weave”, wires are crimped along both parallel and vertical directions, resulting in an isotropic polarization response where the same resonance behavior presents for both parallel and vertical directions.

Although we have confirmed that the weaving style can determine the polarization responses, the origin of this phenomenon and the resonance behaviors associated with different textiles are still not clear. In the next section, we will reveal the nature of the fundament resonances in the textiles. This will help us understand the origins of the observed novel electromagnetic phenomenon in the textile metamaterials, which could affect further engineering of the textile metamaterials.

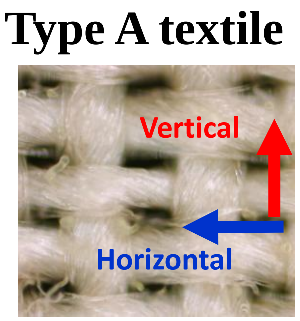
Type A textile
Vertical
Horizontal

(a)

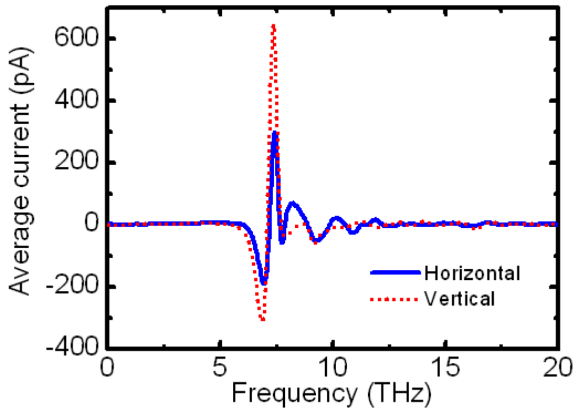
600
400
200
0
-200
-400
Average current (pA)
0
5
10
15
20
Frequency (THz)
Horizontal
Vertical

(b)

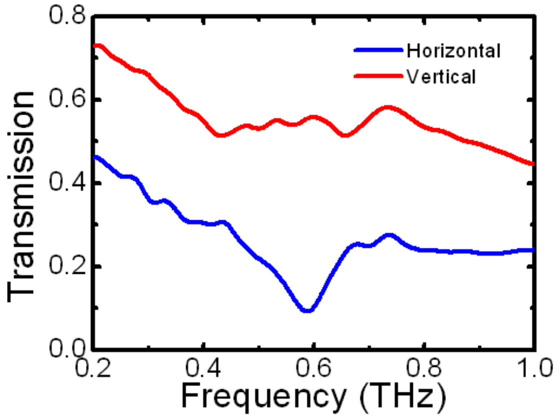
0.8
0.6
0.4
0.2
0.0
Transmission
0.2
0.4
0.6
0.8
1.0
Frequency (THz)
Horizontal
Vertical

(c)

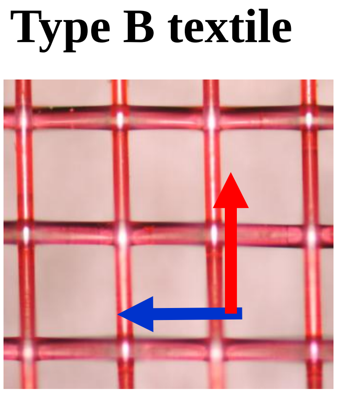
Type B textile

(d)

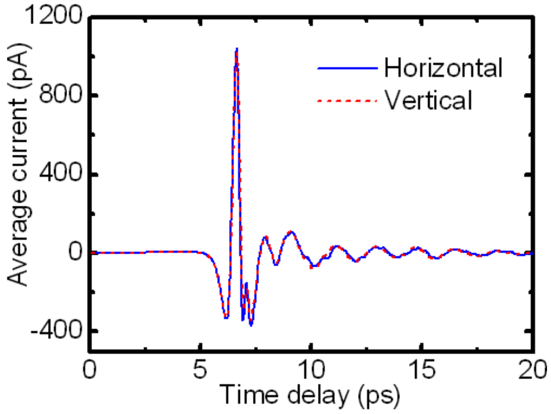
1200
800
400
0
-400
Average current (pA)
0
5
10
15
20
Time delay (ps)
Horizontal
Vertical

(e)

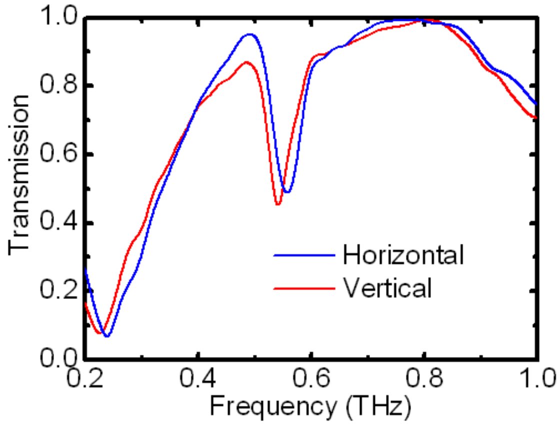
1.0
0.8
0.6
0.4
0.2
0.0
Transmission
0.2
0.4
0.6
0.8
1.0
Frequency (THz)
Horizontal
Vertical

(f)

Figure 5-3 (a) Type A textile with respect to the incident polarizations. (b) Time domain measurements for type A textile under the P and V polarization. (c) Corresponding resonance presents an anisotropic response in transmission spectrum. (d) Type B textile under P and V polarization. (e) Time domain measurements for type B textile. (f) Corresponding resonance presents an isotropic response in the transmission spectrum

Plain Dutch Weave: Type A

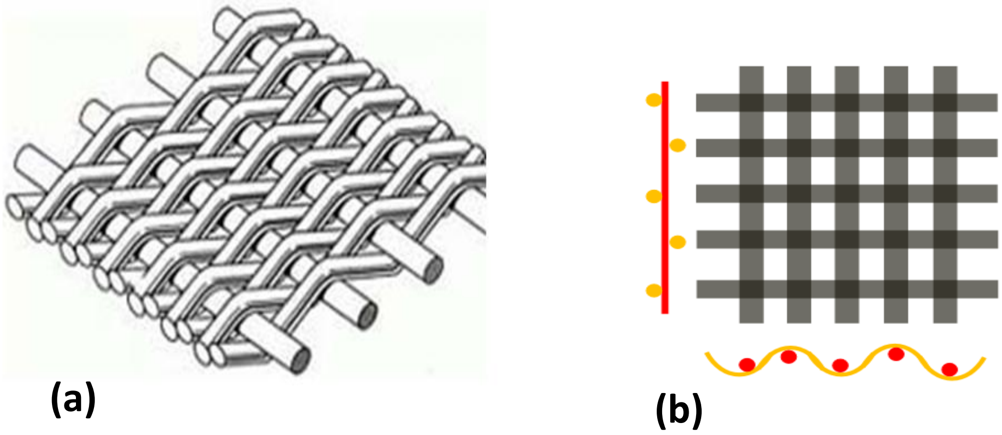

Plain Weave (Double Crimp weaving): Type B

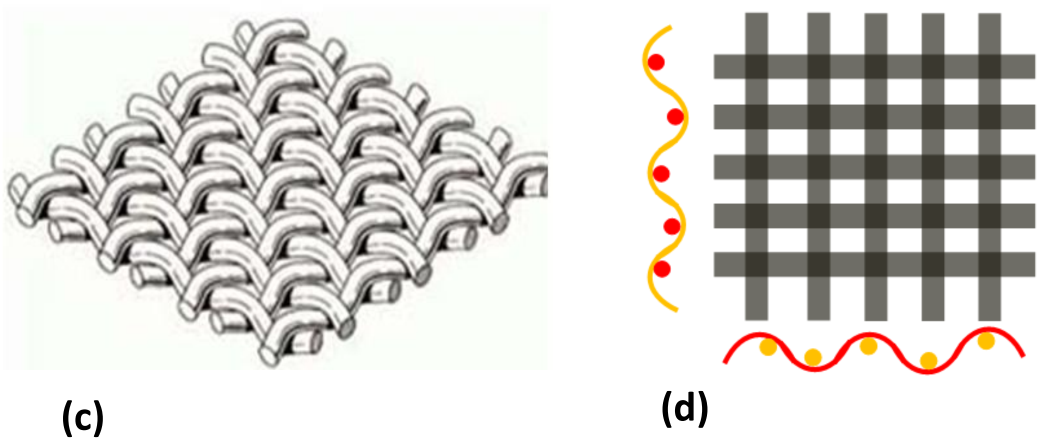

Figure 5-4 Configuration of various weaving styles. (a) “Plain Dutch Weave” corresponding to Type A textile. (b) Space configuration of Type A. (c) “Plain weave (double crimp weaving)” corresponding to type B. (d) Space configuration of type B.

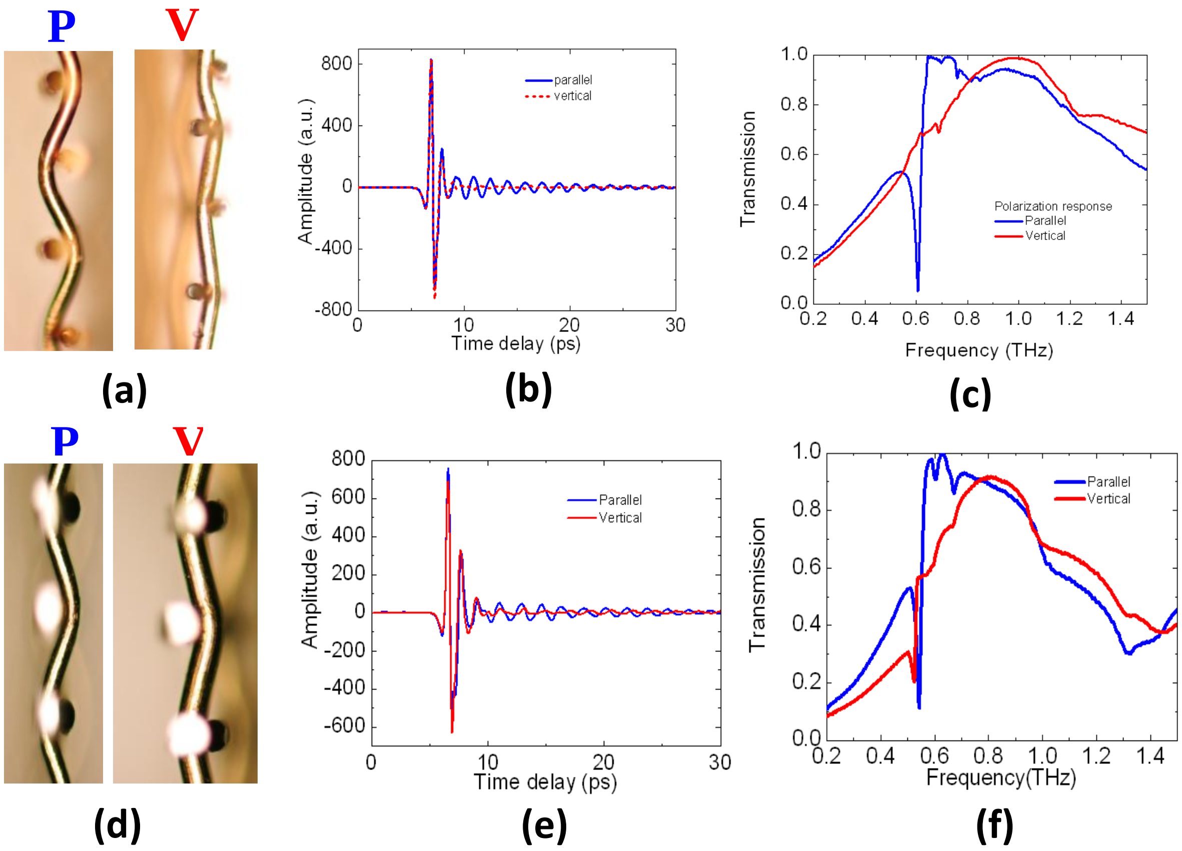

Figure 5-5 Wire textiles associated with weaving styles. (a) Profiles of "Plain Dutch Weave" and corresponding polarization states. (b) and (c) Time domain signal and transmission spectrum of type A textile, respectively. (d) Profiles of "Plain Weave" and corresponding polarization. (e) and (f) Time domain signals and corresponding transmission spectrum of type B, respectively

5.3 Distinguishing wood's anomaly, surface-plasmon-polariton (SPP) and localized plasmonic resonances in the textile metamaterials

Understanding the origin of the resonances in textile metamaterials is crucial to reveal the underlying mechanism of the sensing effect, and could help further designing and optimizing of the devices. It is known that the plasmonic textile metamaterial is essentially formed by periodic metallic structures, and the corresponding electromagnetic responses are generally attributed to three different excitation modes, i.e., diffraction effect, the Surface Plasmon Polaritons (SPPs) and localized plasmonic response. (1) In the diffraction effect, the "Wood's Anomaly (WA)" is the most prominent effect when dealing with subwavelength structures. WA is recognized as a non-resonant process, associating with a diffracted order, becoming tangent to the plane of the grating-like structures. (2) Surface Plasmon Polaritons (SPPs) are collective oscillations of conduction electrons confined at metal-dielectric interfaces. SPPs could be supported by hole array (metal mesh) structures, where an enhanced transmission of light through the mesh structures can be observed and associated with the excitation of SPPs. (3) The localized plasmonic response, in which the local oscillations of electrons play a key role in determining the resonance behavior, and are closely related to the local geometries and interacting materials.

We argue that the fundamental resonance applied in textile metamaterial sensing belongs to the category of the localized plasmonic resonance, and the configurations of crimped wires play a key role to control the resonance behaviors. As a comparison shown in Figure 5-6(a), we use a modified textile material with flattened-trimmed wires compared with the normal textile materials depicted in Figure 5-6(d). This structure changes the original configuration of the curved wires, leading to a transition from localized plasmon mode to SPP resonance, and thus making the textile materials behave more like a plasmonic hole array system (metal mesh structures).

Here, we use the angular-transmission-spectra to map the dispersions of the textile metamaterials as well as that of a corresponding modified structure. By comparing the dispersion curves, different resonance behaviors are explicitly distinguished, revealing the fundamental differences among these electromagnetic responses existing in plasmonic textile materials. First, the Wood's Anomaly (WA) mode due to the tangent diffraction has a following dispersion relation for the two dimensional (2D) periodic systems:

$$\frac{\omega_{WA}}{c} = k_{//} = \left| \frac{\omega_{WA}}{c} \sin\theta \pm nG_x \pm mG_y \right|, \tag{5-1}$$

Where ω_{SW} is the frequency of WA, $k_{//}$ is the momentum parallel to the surface (x-y plane) of textile materials, $\frac{\omega_{WA}}{c}\sin\theta$ is the in-plane wavevector component of the incident light, with a rotation angle θ with respect to the normal direction of the textile surface. $G_x = {}^{2\pi}\!/_{p_x}$ $G_y = {}^{2\pi}\!/_{p_y}$ are lattice momentums offered by the diffraction of the periodic system. From the above equation, the dispersion relation (momentum $k_{//}$ versus frequency ω) of WA mode always holds the relation:

$$k_{//} = \frac{\omega_{WA}}{c}\ , \tag{5-2}$$

It indicates that the WA mode has the same dispersion relation with free-space light, and its dispersion line (characterized by rotation angle θ versus frequency ω in our experiment) acts as the boundary of "light zone" [the yellow region in Figures 5-6(c) and (e)]. It should be noted that although the WA mode propagating along the textile surfaces its behavior differs from a surface bounded mode, which requires that $k_{//} > \frac{\omega_{WA}}{c}$, and the corresponding dispersion line should always distribute within the "light zone" (not including the boundary). As a comparison with WA, SPP mode is a surface bounded mode confined at metal-dielectric interfaces. It should satisfy the condition $k_{//} > \frac{\omega_{WA}}{c}$, and has a dispersion relation:

$$K_{SP} = k_{//} = k_o \sin\theta \pm nG_x \pm mG_y \,, \tag{5-3}$$

where K_{SP} is the propagation wavevector along the surface (x-y plane) of textile materials. As shown in Figure 5-6(b), the modified textile material with flatted-trimmed wire closely resembles a hole array structure, in which, well-defined transmission peaks and transmission dips with respect to the rotation angle θ can be observed in our experiment. From the dispersion diagram shown in Figure 5-6(c), the dispersion curves defined by the transmission dips almost fit with the WA line, thus being identified as the excitation of WA mode. Furthermore, the transmission peaks with respect to the incent angles define a dispersion curve falling into the “light zone” and deviating from the WA line （$k_{//} > \frac{\omega_{WA}}{c}$）, which explicitly indicates surface bounded mode associated with the excitation of SPPs. As shown in Figure 5-6(e), the fundamental resonance of the normal textile material is characterized by a strong and sharp transmission dip. After mapping the dips with respect to the rotation angles, we can see that the dispersion curves shown in Figure 5-6(f), for both TE and TM rotation modes are beyond the “light zone”, indicating that the fundamental resonance of the textile metamaterial is different from the behaviors of Wood’s anomaly and SPPs mode. Two important clues from the experiment could relate this fundamental resonance to the localized plasmonic response. One is the flatness of the dispersion curves, which is a strong evidence for the highly localized nature of the mode. The other clue is the lineshape of the transmission dips, corresponding to a sharp resonance with Fano profiles. This is exactly the behavior expected when Wood’s anomaly (WA) is close to the wavelength of the localized plasmonic resonance. This leads to a strong energy coupling from the incident light into LP modes within a narrow frequency range near a Wood’s anomaly, hence presenting a sharp asymmetric plasmoninc resonance.

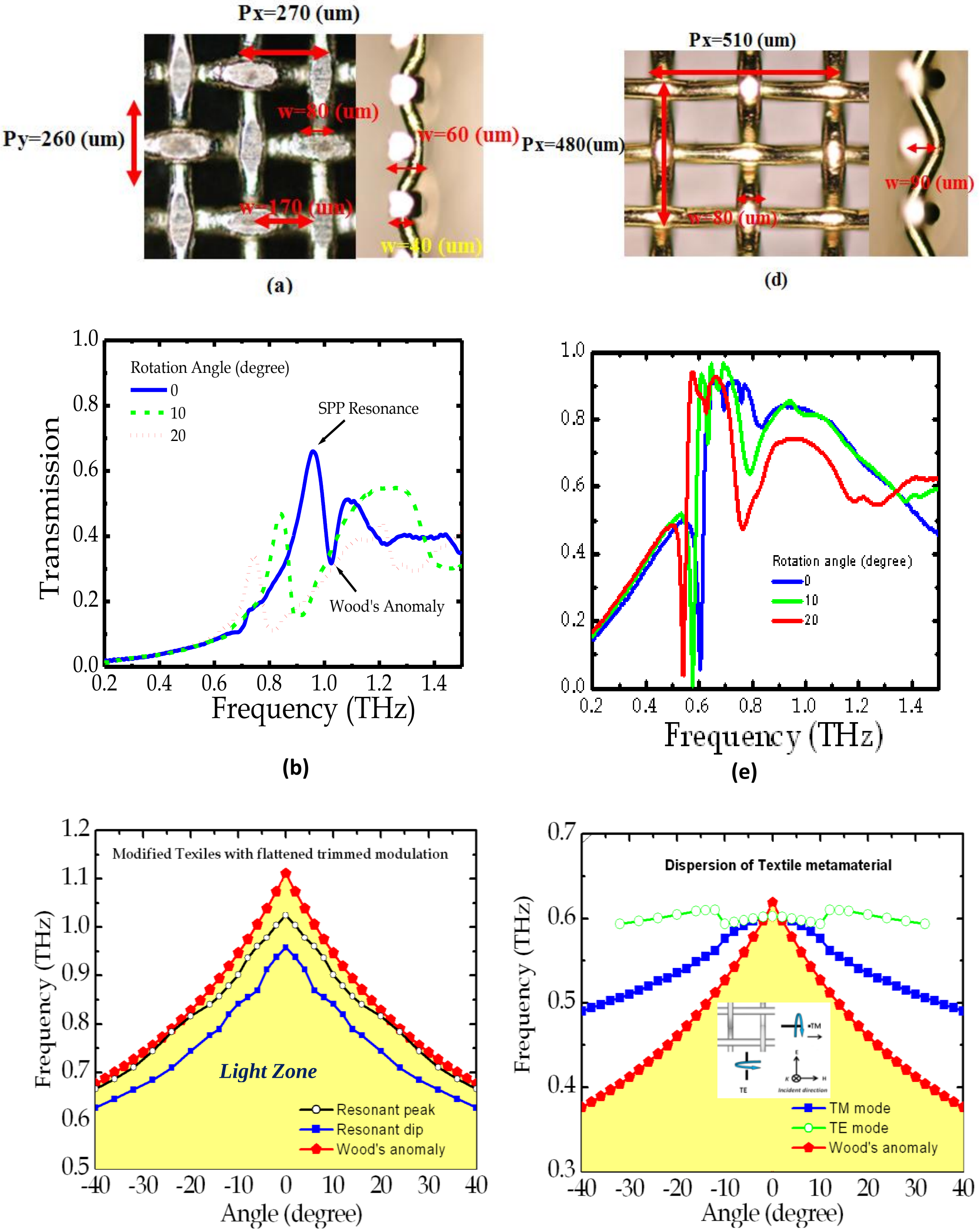

Px=270 (um)
Py=260 (um)
w=80 (um)
w=60 (um)
w=170 (um)
w=40 (um)
Px=510 (um)
Px=480(um)
w=90 (um)
w=80 (um)
Transmission
Rotation Angle (degree)
0
10
20
SPP Resonance
Wood's Anomaly
Frequency (THz)
Rotation angle (degree)
0
10
20
Frequency (THz)
Modified Texiles with flattened trimmed modulation
Light Zone
Resonant peak
Resonant dip
Wood's anomaly
Frequency (THz)
Angle (degree)
Dispersion of Textile metamaterial
TM
TE
Incident direction
TM mode
TE mode
Wood's anomaly
Frequency (THz)
Angle (degree)

(a) (d)

(b) (e)

(c) (f)

Figure 5-6 Dispersion measurement for a modified textile metamateiral and normal textiles. (a) A modified textile material (MTM) with flattened-trimmed wires. (b) Transmission spectrum of MTM with respect to the rotation angles [TM rotation mode, as shown in inset of Figure 5-6(f)]. The arrows indicate different excitation modes. (c) Dispersion diagram of the MTM. (d) A normal textile material (NTM) with curve wires. (e) Transmission spectrum of NTM with respect to the rotation angles. (f) Dispersion diagram of NTM, corresponding to different rotation mode shown in the inset.

5.4 The Hybrid textile metamaterials

As introduced in the section 5.3, the metal wire textiles are promising to support sharp and strong localized plasmonic resonance. This could be a strong boost for sensing applications, because narrower resonance line-widths allow for smaller resonance shifts associated with biochemical signals to be detected. Another advantage is that the configuration of the metal wires is easy to be engineered, enabling well reproducible fabrication for textile materials. As a comparison, the metal coated dielectric textiles suffer from the poor surface roughness, which can negatively influence the resonance strength and quality factors, resulting in a significant degrade performance as a sensor observed in our experiment. However, the pure metal wire textiles lack hydrophilic materials to implement microfluidic transportations. Here we propose a hybrid textile metamaterials comprised of crimped metal wires interlacing with hydrophilic dielectric fibers depicted in Figure 5-7(a). The resonance behavior does not change if the original transverse interlaced metal wires are replaced by dielectric fibers. This effect is demonstrated by numerical simulations shown in Figures 5-7(b) and (c). By using the scheme of hybrid mode, the two functional components, i.e. an electromagnetic resonators and a microfluidic transportation system, are functionally divided. The separation between the two functional components is expected to make a well-performed textile metamaterials, overcoming the drawbacks of both pure metal wire textiles and dielectric textiles.

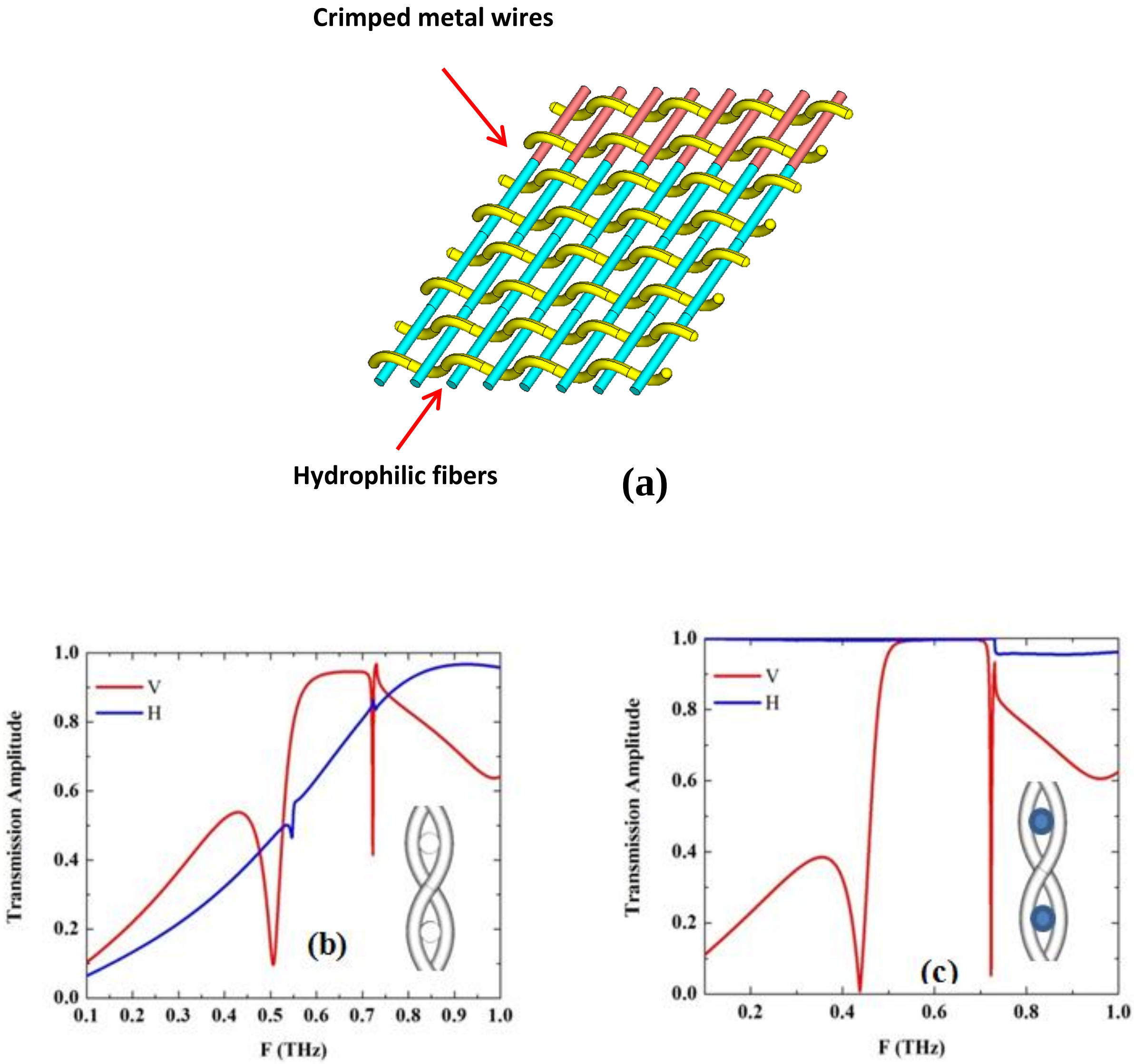

Figure 5-7 (a) A hybrid textile metamaterial comprised of crimped metal wire interlacing with hydrophilic dielectric fibers. (b) Response of pure metal wire textile. (c) Resonance of the hybrid textile, where the transvers metal wires are replaced by the dielectric hydrophilic fibers.

5.5 Weaving engineered textile metamaterials -- the equivalent circuit model

Here, we propose that the weaving technique can engineer the electromagnetic responses of the textile metamaterials, and could enhance the material performance for sensing applications. These prominent capabilities are mainly achieved by tailoring the weaving geometries, and can be exploited within the effective circuit model.

As shown in Figure 5-8(a), the incident THz radiation could induce oscillating surface currents on the curved wires, which give rise to magnetic fields localized in the region enclosed by the curved wires [see Figure 5-8(b)] and can be associated with a inductive response ***L***. Meanwhile, electrical charges accumulate at the two ends of a curved wire, leading to a capacitive response ***C***. Thus, the fundamental resonance of textile metamaterials can be characterized by an equivalent *LC* resonator. The corresponding effective capacitance and inductance can be expressed as:

$$C_{eff} = \alpha \cdot \frac{\varepsilon_o \varepsilon_i h d_2}{p_1/2}, \qquad (5\text{-}4)$$

$$L_{eff} = \beta \cdot \frac{\mu_o 0.5(p_1/2 - d_2)h}{p_2}, \qquad (5\text{-}5)$$

In Equation (5-4), the two ends of a curved wire (along the y direction) act as an effective parallel-plate capacitor that is separated by a distance $p_1/2$ and has an effective plate area hd_2. The ε_o and ε_i are permittivity of the vacuum and filling material (the microfluidic channel) in between the plates, respectively. Equation (5-5) describes the effective inductance per unit periodicity p_1 in the x direction, which is proportional to the area $(p_1/4)(h + \frac{d_2}{2})$ enclosed by a curved wire. α and β are coefficients that could be obtained by fitting the numerical or experimental results. Since the overlapping area between the two opposite curved wires is small, and the distance along the x direction between the two wires is relatively large, the coupling capacitance between the neighboring wires could be neglected as a first approximation. However, when the distance along the x direction between the wires is decreasing, the coupling capacitance may not be ignorable and should be included in a series capacitance equation.

By using the equivalent circuit model, the fundamental resonances of the textile metamaterials hold the following relations with respect to the weaving geometries of textile metamaterials.

$$f_{tex} = \frac{\gamma}{\sqrt{\mu_o \varepsilon_o \varepsilon_i}} \frac{[p_1 p_2]^{\frac{1}{2}}}{[d_2 h^2 (p_1/2 - d_2)]^{\frac{1}{2}}} \quad , \tag{5-6}$$

The corresponding resonance wavelength is:

$$\lambda_{tex} = \frac{\sqrt{\varepsilon_i}}{\gamma} \cdot \frac{h[d_2 (p_1/2 - d_2)]^{\frac{1}{2}}}{[p_1 p_2]^{\frac{1}{2}}} \quad , \tag{5-7}$$

where f_{tex} and λ_{tex} are resonant frequency and corresponding wavelength of the fundamental mode in the textile metamaterial, respectively. γ is a fitting constant (here, $\gamma = 0.02$ is a crude approximation obtained by fitting the numerical results). Although Equation (5-6) can only act as a qualitative model, it gives correct physics and predicts the effects of weaving geometry on the electromagnetic response of textile metamaterials, which are confirmed by the rigorous numerical calculations. First, it tells us that the fundamental resonance wavelength λ_{tex} is approximately proportional to the wire curvature h, provided that other geometry parameters are fixed. As shown in Figure 5-9(b), increasing h is associated with a larger curvature of the wire, and this leads to a redshift of the fundamental resonance. The diameter d_2 of the curved wire is another factor that significantly affects the resonance of the textile metamaterials. As shown in Figure 5-9(a), lager wire diameters will lower the resonance frequencies. Moreover, the individual weaving densities along the x and y directions are found to influence the resonance property of the textile metamaterials in opposite ways. As shown in Figure 5-9(c), raising the weaving density along Y direction can be achieved by decreasing the periodicity p_1 of a unit cell, resulting in a blue-shifted resonance. On the contrary, enhanced weaving density along x direction is achieved by reducing the periodicity p_2; however, this leads to a red-shift.

Furthermore, the sensitivity of the microfluidic sensors could be enhanced through the designs of the weaving geometries. From the view of equivalent circuit model, the LC resonance mode of textile metamaterials interacts with the filling materials (the microfluidic channels interlaced with curved metal wires) in between the curved metal wires, where the resonance shift is due to the dielectric changes of the microfluidic channels by adding the analytes. The sensitivity of the sensor is defined by the resonance shift per unit refractive index. Thus the sensitivity $\overline{S} = \left|\Delta f / \Delta n_i\right|$ with respect to the weaving geometries can be derived from Equation (5-6):

$$\frac{\Delta f_{tex}}{\Delta n_i} = -\frac{\gamma C}{\varepsilon_i} h^{-1} \sqrt{\frac{p_1 p_2}{d_2 (p_1/2 - d_2)}} \quad , \tag{5-8}$$

$$\overline{S} = \frac{\Delta f_{tex}}{\Delta n_i} \propto h^{-1} \sqrt{\frac{p_1 p_2}{d_2 (p_1/2 - d_2)}} \quad , \tag{5-9}$$

where C is the speed of light, ε_i is the dielectric constant of microfluidic channels before adding analytes. As derived from Equation (5-6), the refractive index of microfluidic channels will go up after absorbing the analytes ($\Delta n_i > 0$), thus inducing a redshift resonance, which is demonstrated in our experiment. From Equation (5-9), it is evident that the sensitivity is directly related to the weaving geometries that can enhance the sensing performance. For example, simply choosing thinner metal wires with lower curvature will significantly improve the sensitivity.

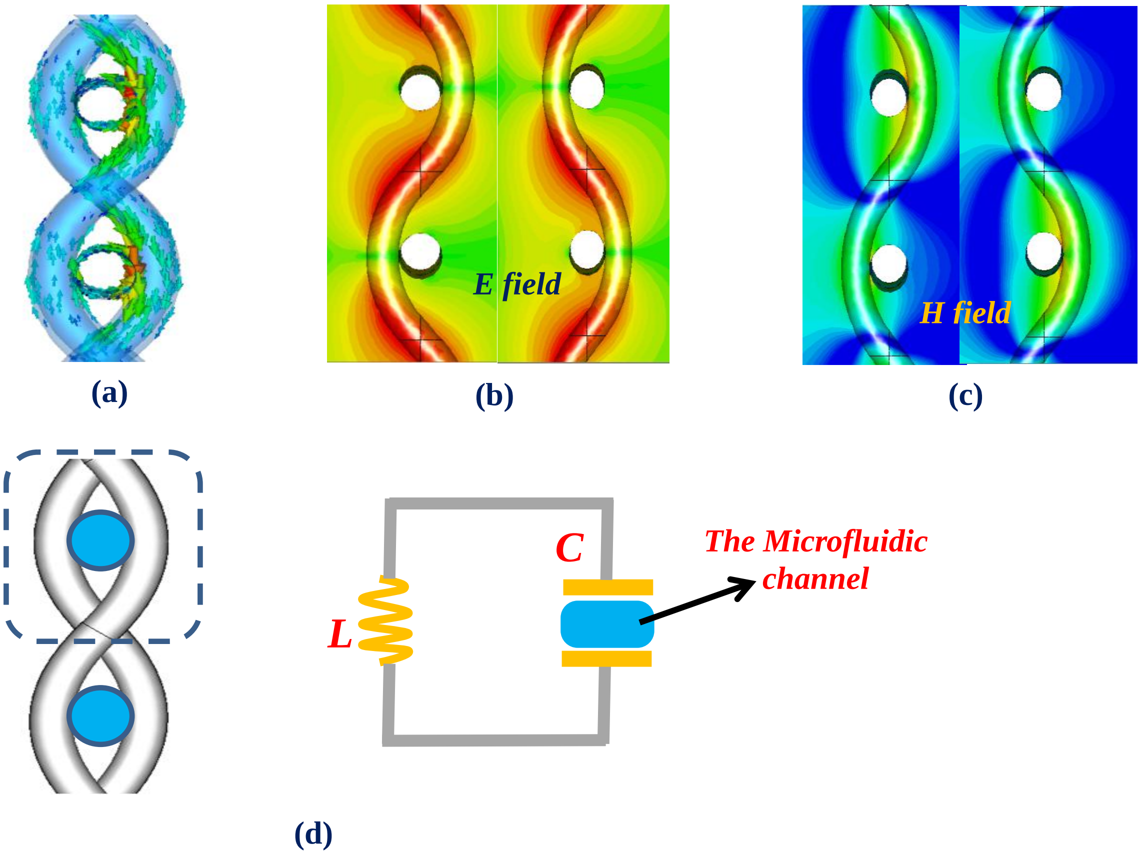

Figure 5-8 (a) Surface currents distribution on textile metamateial of fundamental resonant mode. (b) Electrical field distributions at resonance. (c) Magnetic field distributions at resonance. (d) Schematic of a hybrid textile metamaterial comprised of curved metal wires interlaced with hydrophilic fibers. The insets represent an equivalent ***LC*** resonator, charactering the fundametal resonance of the textile metamaterials.

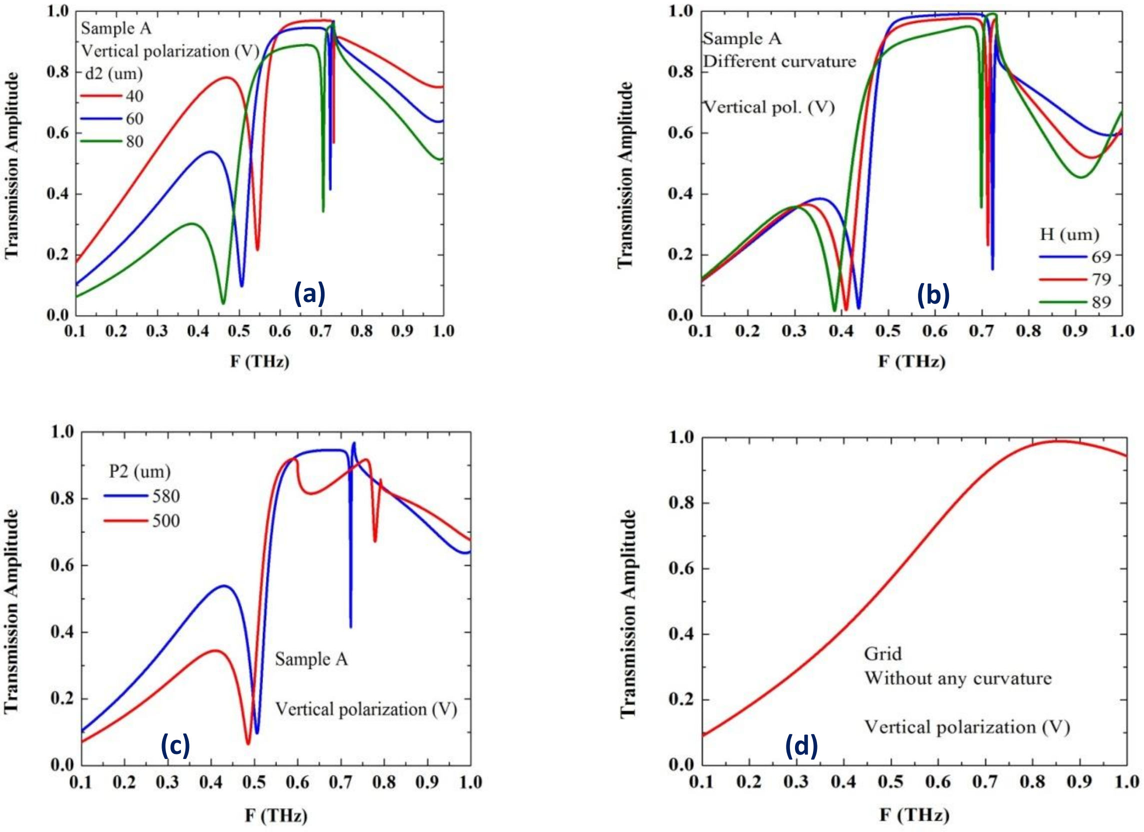

Figure 5-9 Weaving engineered the electromagnetic responses of textile metamaterial. (a) variation of wire diameter, (b) change the wire curvature, (c) the effect of The weaving densities respectively along the X and Y directions, (d) interlaced wires without curvatures.

5.6 Conclusion

We successfully bridge between the electromagnetic textile materials and microfluidic systems functioning in the THz region. This combination may pave a way in developing both functional metamatrials and new THz optofluidic systems, such as fluidic controlled metamaterials. Importantly, a new microfluidic sensing platform is demonstrated, which is benefited from the strong light-fluid interaction in textile metamaterials, showing great potential for cost-effective and high performance sensing platform useful in chemistry, biology and medicine applications.

CHAPTER VI

FUTURE WORK

6.1 Textile photonic crystals: novel electromagnetic properties and microfluidic sensing

Textile materials are formed by periodic dielectric structures and thus could be an ideal photonic crystal system functioning in the THz region. My ongoing work is to explore the electromagnetic responses of textile photonic crystals and combine them with microfluidic systems in sensing applications. This would show great interests and promising applications in THz photonics. The following Figure 6-1 shows the different textile photonic crystal structures with respect to different incident directions of THz radiation. The planar textile photonic crystal are confined in a two dimensional system such as a parallel-plat THz waveguide. The EM responses are expected to present anisotropic or isotropic properties corresponding to different types of textile. When combining with microfluidic system, the textile photonic crystals can be implemented as label free sensors, and the resonance shift of the textile photonic crystals indicates biochemical signals.

“Plain Dutch Weave” textile photonic crystals

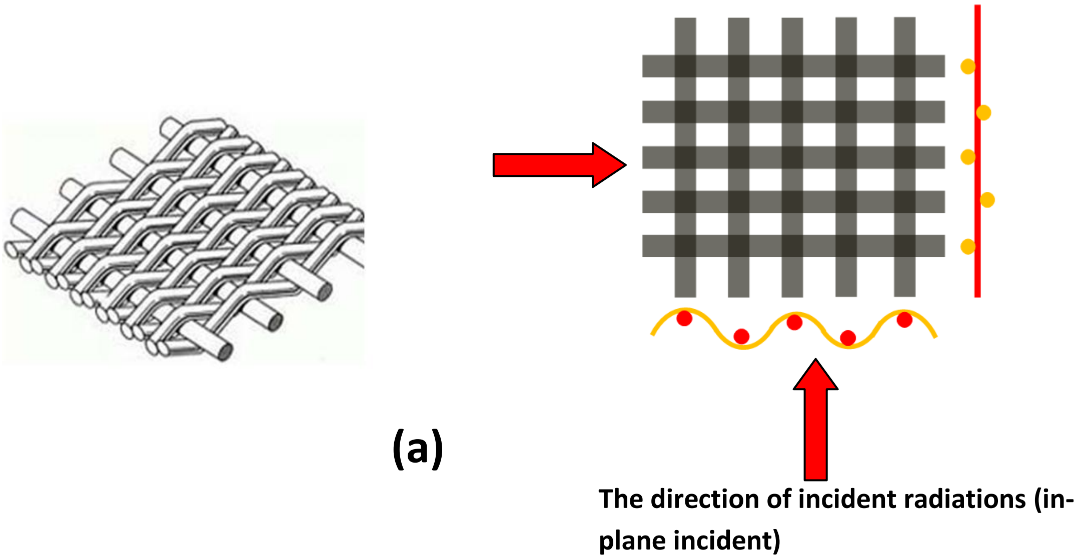

“Plain Weave (double crimped)” textile photonic crystals

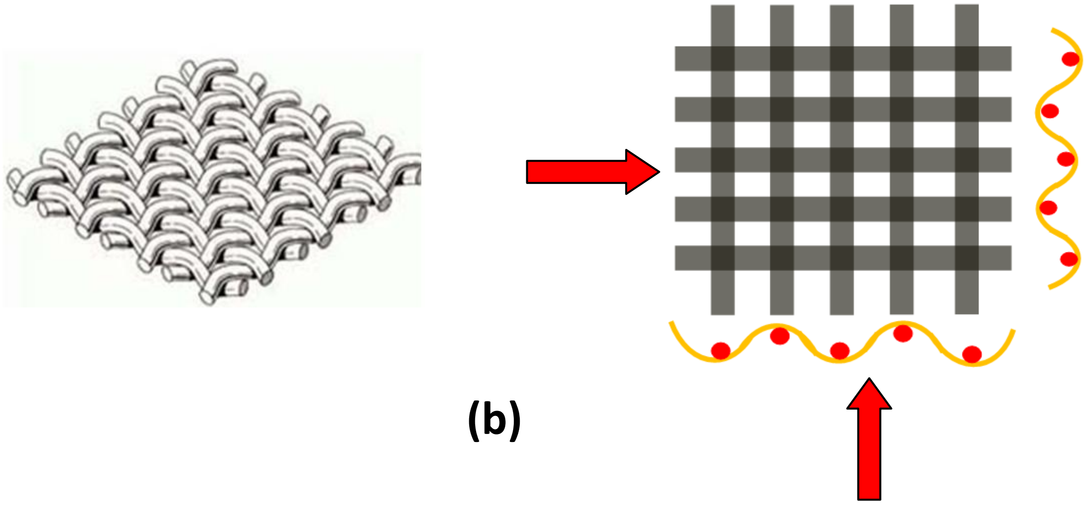

Figure 6-1 Textile photonic crystals. (a) The “plain dutch weave” textile photonic crystals with respect to incident radiations (in-plane) in different directions. (b) The “plain weave (double crimp weave)” textile photonic crystals with respect to incident radiations (in-plane) in different directions.

6.2 Spintronics in THz opto-electronics

Recently, a new class of electronic devices based on the spin degrees of freedom of electrons has emerged. This gives rise to the field of spintronics, in which electron spin carries information instead of charge. Spintronics is believed to be a promising candidate for information technology in the future [102-109]. On the other hand, the processing speed of charge-based devices is limited by the capacitance of the device and the drive current. Such obstacles stop the high speed devices operating at THz frequencies and create a "THz gap" in electronics. Spintronic devices, however, offer a route toward high speed devices operating at THz frequencies, thus helping fill the "THz gap". In spintronic devices, the binary information "0" and "1" are usually characterized by the electron spin orientations, and the information processing is based on the electron-spin resonance, in which the transition between spin orientations can be manipulated by external controls.

Usually, the intrinsic electron-spin resonance depends on the interaction between spin of the carrier and the magnetic properties of materials. However, very recent research has demonstrated that the electron-spin resonance can be engineered by metamaterials which are artificial media and gain their material properties from the geometric structures rather than the intrinsic composition. It is expected that the combination between spintronics and metamaterials may offer a new direction towards the development of future hybrid spintronic devices with unprecedented performance, and overcome the limitations of natural materials for spintronics.

In the scheme of metamaterial mediated electron-spin resonance, the static external magnetic field B_o is applied on the spintronic materials (usually magnetic materials) to generate energy splitting between the up and down electron spins (Zeeman Effect). The energy splitting is given by $\Delta E = g\mu_B B_o$, where g is the dimensionless magnetic moment of electrons called g factor,

μ_B is the Bohr magneton. Following the selection rules of electron-spin resonance, when light passes thorough spintronic materials, if the oscillating magnetic field H of light waves is perpendicular to the static external magnetic field B_o and the light frequencies get a correspondence to the spin energy splitting $\Delta E = h\nu$, the electron spins can absorb the light leading to strong electron-spin resonance, here h is the Planck's constant, ν is the light frequency. The metamaterials combined with spintronic materials are comprised of metallic split-ring resonators (SRR), as shown in Figure 6-2(a). The incident light on the metamaterial surface can excite the split-ring resonances which generate the oscillating electric current loop on the SRR structure and induce a magnetic field component perpendicular to the external static magnetic field, such excitation processes activate the electron-spin resonance in spintronic materials, as depicted in Figure 6-2(b).

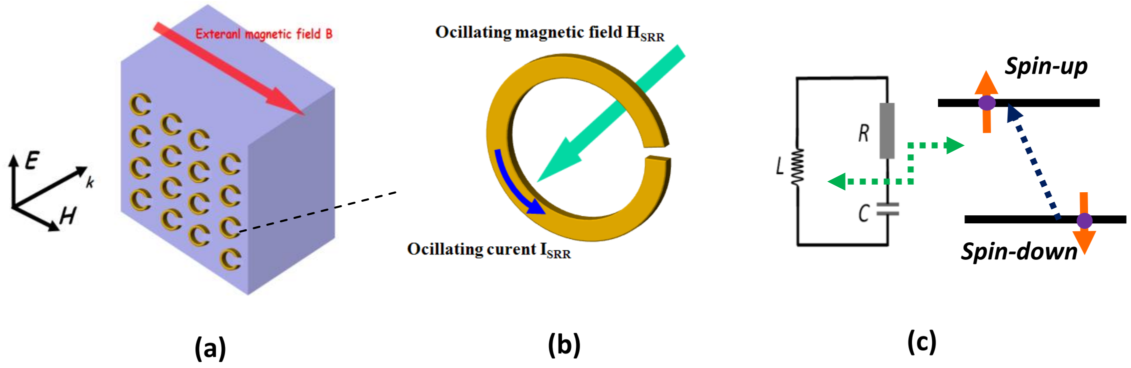

Figure 6-2 (a) The spintronic materials (blue) are combined with metamaterials formed by split ring resonators (yellow). The normally incident light is with electric field E and magnetic field H. The external static external magnetic field B_o is represented by the red arrow. (b) The excited split ring resonance of a single unit cell structure. The oscillating electric current loop and the induced oscillating magnetic field are depicted by blue and green arrays respectively. (c) The coupling (represented by the dashed green arrow) between the electron-spin resonance and split-ring resonance. The *LC* circuit response is equivalent to the split-ring resonance.

The mechanism of metamaterial mediated electron-spin resonance can be understood by the coupling between the electron-spin resonance and split-ring resonance equivalent to a response of *LC* circuit, as shown in Figure 6-2(c). Since the electron-spin resonance is combined with metamateirals and associated with electromagnetic response, the physics of the effect can be characterized by the effective dielectric permittivity model [110].

When a SRR is made from metals with magnetic properties, such as soft magnetic or ferromagnetic materials, it is expected that the electron spin will respond to the magnetic field generated in the SRRs. To study the electron-spin resonance in THz metamaterials, we will first deposit a flat magnetic thin film such as NiFe on silicon substrate and then pattern the SRR structure on the film with conventional lithography processes. Next, we will use external magnetic field to magnetize the SRRs with its magnetization along (or perpendicular to) the substrate plane, and characterize the response of metamaterials in these two magnetization states at THz frequencies. The normally incident THz radiation on the SRR surface can excite the SRR resonances, specifically, generate a unique electron-spin current loop oscillating in the SRR made of magnetic materials), and inducing a magnetic field component perpendicular to the external static magnetic field. Consequently, such excitation processes activate the electron-spin resonance in the SRR, as shown in Figure 6-3. The coupling between the SRR resonance and the electron-spin resonance can also be equivalent to a response of *LC* circuit coupled with electron-spin transition. The coupling constants and resonance frequencies associated with electron-spin will be determined by fitting the experimental THz-TDS transmission data. Once these parameters are determined, other physical quantities of interest in the spintronics field, such as spin current and magnetization, will be calculated.

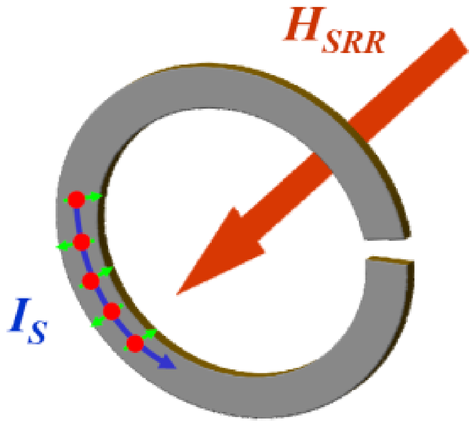

Figure 6-3 SRRs made from magnetic materials with a static external magnetic field (>10 T) applied on the SRRs. Excited SRR resonance in a single unit cell. I_s and H_{SRR} are the oscillating electron-spin current and the induced oscillating magnetic field, respectively.

Based on the fundamental studies described above, we plan to implement a proof-of-concept study of active metamaterial spintronic devices functioning in the THz regime, such as spintronic filters, switches and modulators. As illustrated in Figure 6-4(a), for example, a spintronic metamaterial can be comprised of arrays of a SRR combined with silicon pattern processed on dielectric substrate, such as sapphire. The SRR will be made from magnetic metals, or alternatively, made from regular metals deposited on top of a magnetic thin film. The design shown in Figure 6-4(a) allows for achieving a metamaterial-spintronic filter actively controlled by optical excitation. The shift or modification of the electron-spin resonance will be implemented by tuning the SRR resonance through altering the physical dimensions of the SRRs under photo-doping of the silicon pattern. The response of the SRR under optical excitation can be characterized by an equivalent response of a *LC* circuit. Under optical excitation, the silicon pattern gradually becomes metallic that modifies the effective physical dimension of the SRR such that the effective inductance in the equivalent *LC* circuit is adjusted, showing a photo-inductance response. The tuning and shifting of the SRR resonance couple with the electron-spin resonance, consequently lead to tuning and shifting in the electron-spin resonance, as illustrated in Figure 6-4(b).

Similarly, In Figures 6-4(c) and (d), the design allows for achieving a metamaterial-spintronic switch under active optical control. The spin resonance can be instantaneously turned on and off by photo-doping the silicon pattern on the SRR. The idea of active control using optical excitation can also be expanded to other mechanisms, such as external electric field, temperature, or liquid crystals through appropriate design of the metamaterial unit cells.

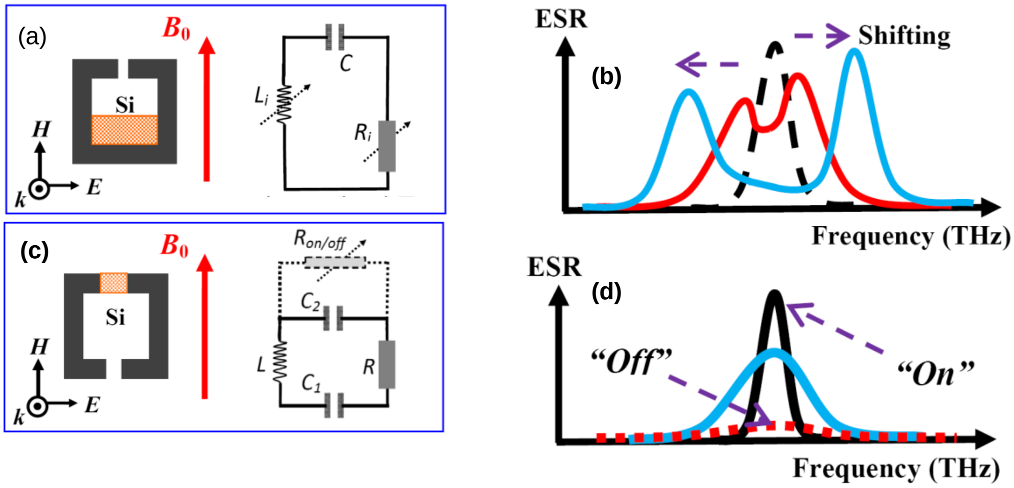

Figure 6-4 (a) Schematic of a SRR unit cell for metamaterial-spintronic filters and the equivalent *LC* circuit under optical excitation. B_o is a static external magnetic field (>10 T). The dashed arrows indicate the effect of optical excitation. (b) Schematic of electron-spin resonance modified by optical excitation. (c) SRR unit cell for metamaterial-spintronic switches or modulators and the corresponding equivalent *LC* circuit under optical excitation. (d) Schematic of electron-spin resonance switching by optical excitation.

6.3 The optimization for the THz slow-light metamaterial devices

The associated slow light phenomena and the performance of planar metamaterial slow-light devices will be characterized and evaluated by the proposed metrics based on the THZ-TDS measurement. The planar meta-material device design will be further optimized based on theoretical modeling and the experimental results. The active control of THz slow-light will be expanded to other approaches, such as electrical, temperature, and magnetic control.

Moreover, the mechanism described for trapping and releasing light relies on the presence of Bragg reflection and cavity resonance, which are general properties in the metamaterial waveguides comprised of periodic cut-through metallic systems. Our preliminary numerical result shows how this general scheme works on the trapping and releasing of THz radiation by use of mechanical or elastic control in the metamterial waveguides. The chanllenge here is the unique design and practical implementation of such prototype metamaterial waveguides that possess: 1) effective Bragg reflection and well-defined cavity resonance at THz frequencies, 2) effective mechanical or elastic tuning approaches, and 3) high coupling efficiency and low propagation losses. We plan to carry out systematic numerical simulations and to use the currently well-established micro-fabrication techniques, such as photolithography and laser micromachining to optimize the device design and to process unique metamaterial waveguides suitable for effective trapping and releasing of THz radiation. Novel micro-electro-mechanical system (MEMS) components will be integrated onto the waveguides to implement the local mechanical or elastic tuning. Near-field probes developed based on THz-TDS technique will be used to acquire and analyze the slow light signal in the waveguides and to characterize the spatial separation of different frequency components trapped along the waveguides.

REFERENCES

1. B. Ferguson and X.-C. Zhang, *Nature Materials.* **1**, 26-33 (2002).
2. M. Tonouchi, *Nature Photonics* **1**, 97–105 (2007).
3. D. H. Auston, K. P. Cheung, J. A. Valdmanis, D. A. Kleinman, *Phys. Rev. Lett.* **53**, 1555-1558 (1984).
4. D. Grischkowsky, S. Keiding, M. Van Exter, and Ch. Fattinger, *J. Opt. Soc. Am. B* **7**, 2006 (1990).
5. R. W. Wood, Proc. R. Soc. London **18**, 269-275 (1902)
6. H. Raether, *Plasmons on Smooth and Rough Surfaces and on Gratings* (Springer-Verlag, Berlin, 1988)
7. T.W. Ebbesen, H.J. Lezec, H.F. Ghaemi, T. Thio, and P.A. Wolff, *Nature* **391**, 667–669 (1998)
8. W. L. Barnes, A. Dereux, T. W. Ebbesen, *Nature* **424**, 824 (2003).
9. L. Mart ń-Moreno, F. J. Garc á-Vidal, H. J. Lezec, K. M. Pellerin, T. Thio, J. B. Pendry, and T.W. Ebbesen, *Phys. Rev. Lett*. **86**, 1114 (2001)
10. J. A. Porto, F. J. Garcıa-Vidal, and J. B. Pendry, *Phys. Rev. Lett.* **83**, 2845 (1999)
11. Barnes, W. L., Preist, T. W., Kitson, S. C. and Sambles, J. R., *Phys. Rev. B* **54**, 6227–6244 (1996).
12. Kitson, S. C., Barnes, W. L. & Sambles, J. R., *Phys. Rev. Lett*. **77**, 2670–2673 (1996).
13. J. Takahara, S. Yamagishi, H. Taki, A. Morimoto, and T. Kobayashi, *Opt. Lett*. **22**, 475-477 (1997).

14. D. F. P. Pile and D. K. Gramotnev, *Opt. Lett*. **29**, 1069-1071 (2004).

15. Georgios Veronis and Shanhui Fan, *Opt. Lett.* **30**, 3359-3361 (2005).

16. T.-I. Jeon, J. Zhang, and D. Grischkowsky, *Appl. Phys. Lett*. **86**, 161904-161906 (2005).

17. Tae-In Jeon_ and D. Grischkowsky, *Appl. Phys. Lett*. **88**, 061113-061115 (2006).

18. Kanglin Wang and Daniel M. Mittleman, *Phys. Rev. Lett.* **96**, 157401 (2006)

19. Qing Cao and Jürgen Jahns, *Opt. Express* **13**, 511-518 (2005)

20. J. B. Pendry, L. Martin-Moreno, F. J. Garcia-Vidal, *Science* **305**, 847-848 (2004).

21. F. J. Garcia-Vidal, L Martın-Moreno and J B Pendry, *J. Opt. A: Pure Appl. Opt*. **7**, S97–S101 (2005)

22. Alastair P. Hibbins, Benjamin R. Evans, J. Roy Sambles, *Science* **308**, 670-672 (20005)

23. F. J. Garcıa de Abajo, and J. J. Saenz, *Phys. Rev. Lett*. **95**, 233901 (2005)

24. Min Qiu, *Opt. Express* **13**, 7583-7588 (2005)

25. G. Goubau, *J. Appl. Phys*. **21**, 1119-1128 (1950).

26. V.G. Veselago, *Usp. Fiz. Nauk* **92**, 517 (1964) [*Sov. Phys. Usp*. **10**, 509 (1968)].

27. J.B. Pendry, A. J. Holden, W. J. Stewart and I. Youngs, *Phys. Rev. Lett*., **76**, 4773, (1996).

28. J. B. Pendry, A. Holden, D. Robbins, and W. Stewart, *IEEE Trans. Microwave Theory Tech* **7**, 2075 (1999).

29. D. R. Smith, W. J. Padilla, D. C. Vier, S. C. Nemat-Nasser, and S. Schultz, *Phys. Rev. Lett.*,**84**, 4184, (2000).

30. D. R. Smith, and N. Kroll, *Phys. Rev. Lett*., **85**, 2933, (2000).

31. R. A. Shelby, D. R. Smith, and S. Schultz, *Science* **292,** 5514, (2001)

32. J. Yao, Z. liu, Y. Liu, Y. Wang, 27C. Sun, G. Bartal, A.M Stacey, and X. Zhang, *Science*, **321**, 930, (2008).

33. S. Linden, C. Enkrich, M. Wegener, J. Zhou, T. Koschny, and C. M. Soukolis, *Science* **306**, 1351 (2004).

34. D. Schurig et al., *Science* **314**, 977 (2006).

35. C. Caloz, and T. Itoh, " *Electromagnetic Metamaterials* ", (Wiley).

36. T. J. Yen, W. J. Padilla, N. Fang, D. C. Vier, D. R. Smith, J. B. Pendry, D. N. Basov, and X. Zhang, *Science* **303**, 1494 (2004).

37. H. T. Chen, W. J. Padilla, J. M. O. Zide, A. C. Gossard, A. J. Taylor, and R. D. Averitt, *Nature* **444**, 597 (2006).

38. H.T. Chen, J.F O'Hara, A.K. Azad, A.J. Taylor, R.D. Averitt, D.B. Shrekenhamer and W.J.Padilla, *Nature Photonics* **2** ,295 (2008).

39. S. Chiam, R. Singh, C. Rockstuhl, F. Lederer, W. Zhang, *Phys. Rev. B* **80**, 153403

40. R. Singh, E.Smirnova, A.J. Taylor, J.F. O'Hara, and W.Zhang, *Optics Express* 16, 6537 (2008).

41. A. K. Azad, J. M. Dai, and W. Zhang, *Opt. Lett*. **31**, 634 (2006).

42. D. Qu, D. Grischkowsky, and Weili Zhang, *Optics Letters*, **29**, 896-898 (2004).

43. Abul K. Azad, Y. Zhao, and W. Zhang, *Applied Physics Letters*. **86**, 141102 (2005).

44. Abul K. Azad and Weili Zhang, *Optics Letters*, **30**, 2945-2947(2005).

45. Abul K. Azad, Yuguang Zhao, Weili Zhang, and Mingxia He, *Optics Letters*. **31**, 2637 (2006).

46. Weili Zhang, Abul K. Azad, Jingzhou Xu, Jian Chen, and X.-C. Zhang, *Physical Review Letters***, 98,** 193901(2006).

47. J. B. Khurgin and R. S. Tucker, *Slow Light: Science and Applications* (CRC Press, Taylor & Francis Group, 2008).

48. Koch, M. "*Terahertz communications: a 2020 vision*," Terahertz Frequency Detection and Identification of Materials and Objects, Netherlands: Springer, pp. 325-338, 2007

49. C.M. Mann, "Towards Terahertz Communications Systems", in: Miles et al. (eds.), *Terahertz Sources and Systems*, Kluwer 2001, pp. 261-267.

50. J.W. Bowen, “Towards Terahertz Communications – Systems Requirements”, in: Miles et al. (eds.*), Terahertz Sources and Systems*, Kluwer 2001, pp. 269-283.

51. Q. Gan, Z. Fu, Y. J. Ding, and F. J. Bartoli, *Phys. Rev. Lett*. **100**, 256803 (2008).

52. Q. Gan, Y. J. Ding, and F. J. Bartoli, *Phys. Rev. Lett*. **102**, 056801 (2009).

53. N. Papasimakis, V. A. Fedotov, N. I. Zheludev, and S. L. Prosvirnin, *Phys. Rev. Lett*. **101**, 253903 (2008).

54. P. Tassin, L. Zhang, T. Koschny, E. N. Economou, and C. M. Soukoulis, P*hys. Rev. Lett.* **102**, 053901 (2009).

55. S. Zhang, D. A. Genov, Y. Wang, M. Liu, and X. Zhang, *Phys. Rev. Lett*. **101**, 047401 (2008).

56. R. Singh, C. Rockstuhl, F. Lederer, and W. Zhang, *Phys. Rev. B* **79**, 085111 (2009).

57. S. Chiam, R. Singh, C. Rockstuhl, F. Lederer, W. Zhang, *Phys. Rev. B* **80**, 153403 (2009).

58. K. L. Tsakmakidis, O. Hess, and A. D. Boardman, *Nature* (London) **450**, 397 (2007).

59. Chen, Y.; Gu, J.; Xie, X. C.; Zhang, W. L. *J. Opt. Soc. Am. A* **28**, 272-277. (2011).

60. Hebling, J.; Yeh, K.-L.; Hoffmann, M.C.; Nelson, K. A. *IEEE J. Select. Topics Quantum Electron*. 2008, 14, 345–353.

61. Nielson, G. N.; Shaw, M. J.; Bogart, G. R.; Spahn, O. B.; Watts, M. R.; Olsson III, R. H.; Resnick, P.; Luck, D.; Brewer, S.; Tigges, C.; Grossetere, G. *Sandia Report* 2008, SAND2008-0211, 1-112.

62. B. A. Munk, “*Frequency Selective Surfaces: Theory and Design”* (John Wiley & Sons, New York, 2000).

63. I. A. I. Al-Naib, C. Jansen, and M. Koch, *Appl. Phys. Lett*. **93**, 083507 (2008).

64. I. A. I. Al-Naib, C. Jansen, and M. Koch, *Appl. Phys. Lett*. **94**, 153505 (2009).

65. I. A. I. Al-Naib, C. Jansen, N. Born, and M. Koch, *Appl. Phys. Lett*. **98**, 091107 (2011).

66. C. Jansen, I. A. I. Al-Naib, N. Born, and M. Koch, *Appl. Phys. Lett***. 98**, 051109 (2011).

67. R. Singh, I. A. I. Al-Naib, M. Koch, and W. Zhang, *Opt. Express* **18**, 13044 (2010).

68. W. L. Chan, H. T. Chen, A. J. Taylor, I. Brener, M. J. Cich, and D. M.Mittleman, *Appl. Phys. Lett*. **94**, 213511 (2009).

69. Mendis, R.; Grischkowsky, D., *J. Appl. Phys*. **2000**, 88, 4449-4451.

70. J. Zhang and D. Grischkowsky, *Opt. Lett*. **19**, 1617 (2004).

71. R. Mendis and D. Grischkowsky, *Opt. Lett*. **26**, 846 (2001).

72. A. L. Bingham and D. Grischkowsky, *Appl. Phys. Lett*. **90**, 091105 (2007)

73. J. O'Hara, R. Singh, I. Brener, E. Smirnova, J. Han, A. Taylor, and W.Zhang, *Opt. Express* **16**, 1786 (2008).

74. X. Liu, S. MacNaughton, D. B. Shrekenhamer, H. Tao, S. Selvarasah, A. Totachawattana, R. D. Averitt, M. R. Dokmeci, S. Sonkusale, and W. J. Padilla, *Appl. Phys. Lett*. **96**, 011906 (2010).

75. H. Tao, C. M. Bingham, A. C. Strikwerda, D. Pilon, D. Shrekenhamer, N.I. Landy, K. Fan, X. Zhang, W. J. Padilla, and R. D. Averitt, *Phys. Rev. B* **78**, 241103 (2008).

76. X. G. Peralta, M. C. Wanke, C. L. Arrington, J. D. Williams, I. Brener, A. Strikwerda, R. D. Averitt, W. J. Padilla, E. Smirnova, A. J. Taylor, and J. F. O'Hara, *Appl. Phys. Lett*. **94**, 161113 (2009).

77. H. Tao, J. J. Amsden, A. C. Strikwerda, K. Fan, D. L. Kaplan, X. Zhang, R. D. Averitt, F. G. Omenetto, *Adv. Mater*., **23**, 3197 (2011)

78. V. A. Fedotov, M. Rose, S. L. Prosvirnin, N. Papasimakis, and N. I. Zheludev, *Phys. Rev. Lett*. **99**, 147401 (2007).

79. W. Zhang, A. K. Azad, and D. Grischkowsky, *Appl. Phys. Lett*. **82**, 2841 (2003).

80. The Fabry-Perot resonance region is located at $f = N(c/2nL)$ (N = 1, 2…), where f is the F- P resonance frequency, N is an integer number, c the speed of light, n is the refractive index of the substrate, and L is the thickness of the substrate. As an example, a 22-µm-thick

Mylar film with refractive index 1.7, the lowest F-P resonance is around 4 THz, which is far away from the *LC* and dipole resonances of the metamaterial resonators.

81. S. Chiam, R. Singh, W. Zhang, and A. A. Bettiol, *Appl. Phys. Lett*. **97**, 191906 (2010).
82. H. Tao, A. C. Strikwerda, M. Liu, J. P. Mondia, E. Ekmekci, K. Fan, D. L. Kaplan, W. J. Padilla, X. Zhang, R. D. Averitt, and F. G. Omenetto, *Appl. Phys. Lett*. **97**, 261909 (2010).
83. W. J. Padilla, M. T. Aronsson, C. Highstrete, M. Lee, A. J. Taylor and R. D. Averitt, *Phys. Rev. B* 75, 041102 (2007)
84. W. Zhang, Eur. Phys. *J. Appl. Phys*. **43**, 1 (2008).
85. Y. S. Jin, G. J. Kim, and S. G. Jeon, *J. Korean Phys. Soc*. **49**, 513 (2006).
86. P. D. Desai, H. M. James, and C. Y. Ho, *J. Phys. Chem. Ref. Data* **13**, 1131 (1984).
87. B. Luk'yanchuk, N. I. Zheludev, S. A. Maier, N. J. Halas, P. Nordlander, H. Giessen, and C. T. Chong, *Nature Mater*. **9**, 707 (2010).
88. R. Singh, I. A. I. Al-Naib, M. Koch, and W. Zhang, *Opt. Express* **19**, 6312-6319 (2011)
89. S. Wietzke, C. Jansen, M. Reuter, T. Jung, D. Kraft, S. Chatterjee, B.M. Fischer, M. Koch, *J. Mol. Struct*. **1006**, 41 (2011).
90. C. Wood, J. Cunningham, I. C. Hunter, P. Tosch, E. H. Linfield, and A. G. Davies, *Int. J. Infrared Millim. Waves* **27**, 557 (2006).
91. Shen, J. T.; Catrysse, P. B.; Fan, S. *Phys. Rev. Lett*. 2005, 94, 197401-197404
92. Shin, J.; Shen, J. T.; Fan, S. *Phys. Rev. Lett*. 2009 102, 093903-093906
93. Y. Chen, Z. Song, Y. Li, M. Hu, Q. Xing, Z. Zhang, L. Chai, and C. Y. Wang, *Opt. Express* **14**, 13021 (2006).
94. T. Lopez-Rios, A. Wirgin, *Solid State Comm*. **52**, 197-201 (1984)
95. R. Collin, *Field Theory of Guided Waves*. (New York: McGraw-Hill, 1960)
96. Stefan A. Maier and Steve R. Andrews, *Appl. Phys. Lett*. **88**, 251120-251122 (2006).

97. Stefan A. Maier, Steve R. Andrews, L. Martín-Moreno, and F. J. García-Vidal, *Phys. Rev. Lett.* **97**, 176805 (2006)
98. Taflove, A.; Hagness, S. C. *"Computational Electrodynamics, The Finite-Difference Time-Domain Method"* (Artech House, 2000).
99. K. Zhang and D. Li, "*ElectromagneticTheory for Microwaves and Optoelectronics"* (Springer-Verlag, Berlin, Heidelberg, 1998).
100. N.-H. Shen, M. Massaouti, M. Gokkavas, J.-M. Manceau, E. Ozbay, M. Kafesaki, T. Koschny, S. Tzortzakis, and C. Soukoulis, *Phys. Rev. Let*t. **106**, 037403 (2011)
101. P. Bhandari, T. Narahari and D. Dendukuri, *Lab Chip*, 2011, **11**, 2493–2499
102. Wolf, S. A.; Awschalom, D. D.; Buhrman, R. A.; Daughton, J. M.; Molnár, S. von; Roukes, M. L.; Chtchelkanova, A. Y. and Treger, D. M., *Science* **294**, 1488 (2001)
103. Ziese, M. and Thornton, M. J. eds., *Spin electronics* (Springer-Verlag, 2002).
104. Awschalom, D.D.; Sarmarth, N. and Loss, D. eds., *Semiconductor Spintronics and Quantum Computation* (Springer-Verlag, Berlin, 2002).
105. Zutic, I.; Fabian, J.; and Sarma, S.D., *Rev. Mod. Phys.* ***76****, 323 (2004)*
106. Awschalom, D. D. and Flatte, M. E., *Nat. Phys*. **3**, 153 (2007).
107. Son, Y. W.; Cohen, M. L. and Louie, S. G., *Phys. Rev. Lett.* **97**, 21683 (2006)
108. Han, M. Y.; Ozyilmaz, B.; Zhang, Y. and Kim, P., *Phys. Rev. Lett.*, **98**, 206805 (2007).
109. Lu, J.; Zhang, X. and Pantelides, S. T., *Phys. Rev. B*. **79,** 073408 (2009).
110. Schneider, A.; Shuvaev, A.; Engelbrecht, S.; Demokritov, S. O. and Pimenov, A. , *Phys. Rev. Lett.*, **103**, 103907 (2009).

VITA

Yongyao Chen

Candidate for the Degree of

Doctor of Philosophy

Thesis: MANIPULATING THZ RADIATION USING NOVEL METAMATERIALS TOWARDS FUNCTIONAL PASSIVE AND ACTIVE DEVICES

Major Field: Electrical Engineering

Biographical:

Education:

Received the Bachelor of Science degree in Optoelectronics from Tianjin University, China, in July 2003; received the Master of Science degree in Physics electronics from Tianjin University, China, in April 2007.

Completed the requirements for the Doctor of Philosophy degree in Electrical Engineering at Oklahoma State University, Stillwater, Oklahoma, in July, 2012.

Experience:

Employed by State Intellectual Property Office of China (SIPO), as a patent examiner, April 2007 to July 2008; employed by Oklahoma State University, Department of Electrical and Computer Engineering as a teaching and research assistant, August 2008 to present.

Name: Yongyao Chen Date of Degree: July, 2012

Institution: Oklahoma State University Location: Stillwater, Oklahoma

Title of Study: MANIPULATING TERAHERTZ RADIATION USING NOVEL METAMATERIALS TOWARDS FUNCTIONAL PASSIVE AND ACTIVE DEVICES

Pages in Study: 139 Candidate for the Degree of Doctor of Philosophy

Major Field: Electrical Engineering

Scope and Method of Study: The objective of this study is to explore the fundamental physics in novel metamatrials functioning in THz region, and to develop passive and active functional devices, such as filters, switch/modulators, waveguides and sensors functioning in the THz regime. Such metamaterial structures were fabricated by using microelectronic lithography technique. The transmission and dispersion properties of the metamaterials were systematically investigated by using THz time-domain spectroscopy. Numerical simulations were carried out to further verify and reveal the experiment results.

Findings and Conclusions: We demonstrated that membrane metamaterials could resolve the limitations encountered in planar metamaterials fabricated on conventional substrates, and are particularly advantageous for developing cost-effective and high-performance devices, such as high-*Q* THz filter and disposable THz sensors. Moreover, we proposed that anisotropic metamaterials could be used to trap and harvest THz radiations in designed metamaterials waveguides. This research will lead to broad range applications, including optical delay-lines, ultra-broadband absorbers, sensitive detectors and optical sensor benefited from the enhanced light-matter interaction in metamaterial waveguides. In order to extend the tunability of metamaterials, we demonstrated that surface modes supported by the membrane metamaterials can be incorporated into the design of broadband tunable devices, showing great potential in practical applications, such as broadband filters and phase shifters functioning in the far-infrared region. In our latest research, it is found that micro-textiles can act as excellent artificial electromagnetic materials. On the other hand, a textile consisting of periodic networks of microfibers can be a pump-free microfluidic system because of the fluidic flow driven by the capillary force of fibers. We successfully combine the electromagnetic textile materials and microfluidic systems together, and make it functioning in the THz region. This research opens a door in developing functional metamatrials and new THz optofluidic systems. Importantly, a new microfluidic sensing platform is demonstrated which is benefited from the strong light-fluid interaction in textile metamaterials, showing great potential for cost-effective and high performance sensing platform useful in chemistry, biology and medicine applications.

ADVISER’S APPROVAL: Dr. Weili Zhang